Edinburgh Research Explorer

Cluster-surface interaction: From soft landing to implantation

OPEN ACCESS

Cluster–surface interaction: From soft landing to implantation

Vladimir N. Popoka,[2] Ingo Barke,[1] Eleanor E.B. Campbell,[3,4] Karl-Heinz Meiwes-Broer[1]

[1]Institute of Physics, University of Rostock, 18051 Rostock, Germany.

[2]Department of Physics and Nanotechnology, Aalborg University, 9220 Aalborg, Denmark.

[3]EaStCHEM, School of Chemistry, Joseph Black Building, University of Edinburgh, West Mains Road, Edinburgh, EH9 3JJ, UK.

[4]Division of Quantum Phases and Devices, Konkuk University, 143-701 Seoul, Republic of Korea.

[*]Corresponding author; e-mail address: vladimir.popok@uni-rostock.de

Abstract:

The current paper presents a state-of-the-art review in the field of interaction of atomic and molecular clusters with solids. We do not attempt to overview the entire broad field, but rather concentrate on the impact phenomena: how the physics of the cluster–surface interaction depends on the kinetic energy and what effects are induced under different energetic regimes. The review starts with an introduction to the field and a short history of cluster beam development. Then fundamental physical aspects of cluster formation and the most common methods for the production of cluster beams are overviewed. For cluster–surface interactions, one of the important scenarios is the low-energy regime where the kinetic energy per atom of the accelerated cluster stays well below the binding (cohesive) energy of the cluster constituents. This case is often called

soft landing: the deposition typically does not induce cluster fragmentation, i.e. the clusters tend to preserve their composition but not necessarily their shape. Specific characteristic phenomena for soft landing of clusters are summarized. They pave the way for the use of cluster beams in the formation of nanoparticle arrays with required properties for utilization in optics and electronics, as magnetic media and catalysts, in nanobiology and nanomedicine. We pay considerable attention to phenomena occurring on impact of clusters with increased kinetic energies. In particular, we discuss the physics of the intermediate regime between deposition and implantation, i.e. slight cluster embedding into the surface—otherwise known as cluster pinning. At higher impact energies, cluster structure is lost and the impact results in local damage of the surface and often in crater and hillock formation. We consider both experimental data and theoretical simulations and discuss mechanisms of these phenomena. Some analogies to the impact of macroscopic objects, e.g. meteorites are shown. This part of the paper also overviews the research on surface sputtering under high-fluence cluster beam treatment and the existing models explaining how this phenomenon can be used for efficient smoothing of surfaces on the macroscopic scale. Several examples of successful applications of the cluster beam technique for polishing of surfaces are given. We also discuss how the physical sputtering can be combined with reactive accelerated cluster erosion. The latter can be an efficient tool for dry etching of surfaces on the nanoscale. Specificity of cluster (multicomponent projectile) stopping in matter and formation of radiation damage under keV-to-MeV energy implantations are analyzed. The part about fundamental aspects of cluster implantation is followed by several examples of practical applications of keV-energy cluster ion beams. This includes ultra-shallow doping of semiconductors and formation of ultrathin insulating layers. A few examples of MeV-energy cluster implantation, leading to the formation of nanosize hillocks or pillars on the surface as well as to local phase transitions (for instance, graphite-to-diamond) are also discussed. The review is finalized by an outlook on the future development of cluster beam research.

Contents

1. Introduction

Atomic (or molecular) clusters are aggregates of atoms (or molecules). A cluster can be formed from atoms of the same chemical element or from two or more different species. Depending on composition, these aggregates may exhibit different binding types as well as different geometric and electronic structures. Their sizes can vary from a few up to many thousands of constituents. Medium and large size clusters have diameters on the scale of nanometers and they are often called nanoparticles (NP). Clusters show properties intermediate between those of individual atoms (or molecules), with discrete energy states, and bulk matter characterized by continua or bands of states. One can say that clusters represent a distinct form of matter, a "bridge" between atoms and molecules on the one hand and solids on the other. A wide variety of clusters has been produced and investigated from precursors including metals, semiconductors, ionic solids, noble gases and molecules. More detailed information about the classification of clusters, their bonding types, structure and properties in the gas phase goes beyond the scope of this review and can be found elsewhere [1, 2, 3, 4, 5, 6].

Interest in clusters comes from various fields. Clusters are used as models to investigate fundamental physical aspects of the transition from the atomic scale to bulk material. They can also be considered as a bridge across the disciplines of physics and chemistry, providing a means to probe the non-monotonic variations of properties and unusual phenomena of nanoscale objects [7]. Clusters on surfaces define a new class of systems highly relevant for practical applications. Finite size effects lead to electronic, optical, magnetic, chemical and other properties that can be quite different from those of the same material in the bulk form. They are of great interest for practical applications in areas such as electronics and optics, biology and medicine, catalysis and other nanotechnology-related branches [8, 9, 10, 11, 12, 13, 14, 15, 16, 17, 18, 19]. With clusters consisting of thousands of atoms it is possible to transport and locally deposit a large amount of material, providing an advanced method for growth of thin films which can be either porous or very compact and smooth depending on the energy regime used for cluster deposition [20, 21, 22, 23, 24]. Cluster assisted

deposition, where material being deposited is bombarded by energetic clusters, allows the control of the structure and composition of the grown layers, for instance, to fabricate thin and hard diamond-like carbon films [25]. Control of cluster kinetic energy provides a possibility to tune the cluster-surface interaction regime from soft landing towards implantation [26, 27, 28, 29, 30, 31].

Energetic cluster beams are found to be very efficient tools for the processing of surfaces (dry etching and cleaning) or improving surface topology (smoothing) [26, 28, 32, 33, 34]. Energetic cluster-surface collisions can be of significant interest for inducing specific chemical reactions due to the temporary build-up of high particle densities and the ultrafast dissipation and redistribution of significant amounts of energy within a very localized region [35, 36]. Implantation of keV-energy clusters is an efficient method for ultra shallow junction formation and infusion doping of shallow layers [37, 38, 39]. High-energy implantation leads to a number of interesting phenomena related to the very large energy density deposited during the cluster-substrate interaction, generating a highly excited region around the projectile path. For instance, nanosize hillocks or pillars can be formed on surfaces of various metal oxides by impact of MeV-energy cluster ions [40, 41]. Irradiation of polymer material by high-energy clusters followed by etching demonstrates a way for the formation of nanoporous membranes [42]. Upon MeV implantation of fullerenes into graphite, the relaxation of the deposited energy leads to a phase transition. In particular, the local compression and increase of temperature are enough for the formation of nanocrystalline diamond particles [43].

The current state-of-the-art in the field of cluster-surface interactions is presented below. However, before concentrating on the fundamental physics of cluster-solid collisions and practical applications of cluster beams for modification of surfaces and building of nanostructures, we give a brief history of cluster beam development and a survey of the physical principles and most commonly-used methods of cluster formation.

2. Formation of cluster beams

In this chapter, after mentioning a few historical milestones and several considerations of cluster nucleation, we discuss the most common methods of their production and size selection.

2.1. Brief history of cluster beam development

The formation of beams containing agglomerates of atoms was mentioned for the first time in the 50's [44]. In particular, small clusters of hydrogen, nitrogen and argon were separated from non-condensed residual gas and transferred into a high vacuum. At the same time it was demonstrated with CO_2 and H_2 that cluster beams can be ionized by electron bombardment enabling mass spectra to be obtained [45, 46]. These experiments were followed by investigations of the distribution of charged CO_2 clusters, $(CO_2)_n^+$ (where n is the number of constituents), in a beam depending on conditions of the cluster source [47] and by development of methods to evaluate cluster sizes, for example, by scattering of a potassium atomic beam passing through a nitrogen cluster beam [48]. Already in the 60's the concept of electrospray sources was introduced. This technique was initially designed to produce molecular beams of macro-ions, in particular, polymers [49]. Later, this type of source started to be used extensively for the study of different cluster species which could be formed from solutions [50, 51]. The development of various cluster techniques led not only to the investigations of clusters in the gas phase but also enabled studies of cluster-surface interactions. For instance, the dependence of nitrogen cluster reflection from stainless steel on the angle of incidence was studied [52]. First experiments on bombardment of carbon and gold foils by high-energy dimers and trimers of hydrogen were performed [53].

In the 70's the cluster technique underwent further development and improvement towards obtaining more stable and controllable beams as well as introducing new methods of cluster production. An idea similar to electrospray formation was applied to liquid metals. By means of field-emission, intense cluster ion beams of different metals (Li, Cs, Sn, Ga and Hg) were generated [54, 55, 56]. Cluster formation in expanding supersonic jets was

implemented [57] and gas aggregation (vaporization) sources for production of metal and semiconductor clusters were developed [58, 59, 60]. However, the first published results on the deposition of Si, Au and Cu suffer from a lack of confirmation concerning the cluster-to-monomer ratio in the beams [59].

The 80's brought more controllable parameters of the cluster beams and showed the applicability of ionized clusters for synthesis of thin metal films and heterostructures [61, 62]. The electrospray ionization method underwent significant improvement. In particular, an approach to eliminate re-solvation of macromolecular ions was invented and the source was combined with a mass-spectrometer that drastically improved accuracy in identification of molecular species [63]. This technique turned out to be especially important for analysis of biological macromolecules, a success which led to the Nobel Prize in Chemistry being awarded to J.B. Fenn in 2002.

The wide range of new techniques that were developed throughout the 70's and 80's were not only relevant for practical applications, they were also essential for furthering our understanding of the fundamental aspects of the physics and chemistry of clusters. For example, the "magic numbers" in the mass-spectra of rare gas clusters provided evidence for the icosahedral packing of atoms [64]. The electronic shell model was developed for metal clusters [65]. A source utilizing laser vaporization was invented that allowed cluster production to be extended over practically any solid material including those with high melting points [66, 67, 68]. The study of carbon clusters produced by laser ablation led to the discovery of fullerenes in 1985 [69] and the award of the Nobel Prize in Chemistry in 1996. Towards the end of the 80's, the idea of using arc discharge for cluster formation was introduced that led to the development of a pulsed arc cluster ion source with good performance for production of pure metal clusters as well as metal-doped rare gas cluster ions [70]. The ion sputtering method, which was previously used for production of monomers [71], was adopted for cluster formation [72, 73].

In the 90's, magnetron sputtering, a well-known method for molecular beam epitaxy, was introduced for cluster formation [74] and many different types of cluster sources underwent

further development [75, 76, 77, 78]. Devices for cluster beam control, manipulation and characterization were significantly improved [27, 76]. Progress in cluster beam techniques together with the beginning of the "nanoscience era", stimulated a significant increase of interest in research on both clusters in the gas phase and deposited (supported) clusters. We refer here to only a few of the topical reviews on "free" [1, 2, 76, 79, 80] and supported clusters [8, 11, 19, 24, 81, 82]. Early experiments on energetic cluster-surface interactions, cluster implantation and sputtering of surfaces by clusters beams should be noted [26, 83, 84, 85]. At the same time, systematic experimental work accompanied by molecular dynamics (MD) simulations started to provide a clear picture of the physical mechanisms of cluster-surface interactions [86, 87, 88, 89, 90, 91, 92, 93]. The milestones in this research field are reviewed below.

2.2. Fundamental aspects of cluster nucleation and growth

Nucleation is a subtle thermodynamic problem with numerous boundary conditions. Older classical and modern approaches are widely found, often constrained to a given class of materials [94, 95]. For cluster production a condensing flow is used, which can be described by (i) the homogeneous nucleation of liquid droplets from supersaturated vapors and (ii) by the growth of droplets. These two main theoretical approaches which principally are strongly connected appear as distinct subjects in the literature. In particular, in order to get reliable solutions one has to solve the Boltzmann equation, also close to the droplet surface. For now, it can be stated that homogeneous nucleation theory still has not reached a clear understanding after about 100 years of research. One of the weaknesses of the classical theory appears to be that it does not give sufficient attention to the energy transfer during the cluster growth [95]. Instead, a non-isothermal theory is needed, starting from the molecular level and valid all the way to the final droplet. It is not the task of this work to solve the problem of nucleation. Instead we merely address a few key properties before going into technical details of cluster production.

A good starting point to describe nucleation is to consider three-body collisions in a supercooled gas. The third partner has the role to simultaneously fulfill energy and momentum conservation, and it stabilizes the nascent dimer, which itself may serve as a nucleus for further cluster growth. Often a diffusion-limited growth is assumed to make the calculations feasible, leading to uniform size distributions (which means neglecting differences in binding energies). For this it is anticipated that the heat of condensation, released by the growing cluster, has to be carried away by a cooling (or carrier) gas. If each collision leads to cluster growth, the growth rate will be proportional to the collision rate between condensable atoms and the cluster. For such a scenario, Weiel has solved the rate equations as a function of the distance from the source nozzle, δ. In such a nozzle flow, the local temperature $T(\delta)$ is related to the local Mach number $M(\delta)$ by

$$T(\delta) = T_0 \left(1 + \frac{1}{fM(\delta)^2} \right)^{-1}, \tag{1}$$

where T_0 is the stagnation temperature and f is the number of internal degrees of freedom of the expanding gas mixture. Taking into account the relation between the number density of the vapour component and the local temperature $T(\delta)$, a solvable rate equation can be obtained [96]. Fig. 1 gives the result for an expanding MgF_2 vapour – argon mixture. Obviously, the maximum cluster size n_{max} is reached already close to the nozzle, i.e. after about 10 nozzle diameters.

For a more comprehensive view on cluster nucleation we refer to early work by Campargue et al. [97], reviewed and extended by Miller [98].

2.3. Methods of cluster production

It follows from the previous section that cluster production requires a thermodynamic non-equilibrium that can be implemented by means of different types of cluster sources. The preferred method of cluster formation can be chosen depending on e.g. the type of cluster species or the desired size of the particles. Technically, high-melting-point material clusters

are mainly produced with laser vaporization or plasma-based approaches, see below. In both cases the material is brought into the gas phase, being partially ionized, and then undergoes cooling and expansion in a stream of inert (carrier) gas. This can be pulsed, allowing for a hard expansion of the seeded clusters into vacuum, or it is continuously streamed at lower pressure. Lower melting point materials can be vaporized within resistively heated ovens or be expanded directly, e.g., through a high-pressure nozzle into vacuum.

All cluster sources are housed inside differentially-pumped vacuum chambers in order to reduce the gas load at the point of investigation. Ideally, only the central filament of the jet passes a narrow skimmer and enters the next section of the vacuum system as a collimated cluster beam. Further differential pumping can lead to sufficiently low pressure for providing ultra-high vacuum conditions required in experiments such as depositing the clusters onto ultraclean surfaces.

2.3.1. Gas aggregation

The starting point for gas aggregation is the evaporation of a solid or a liquid material into an aggregation chamber, which is filled with a cold gas at several mbar. Upon reaching supersaturation and after many collisions within the inert gas, the atoms nucleate to clusters or particles. The formation of smoke, fog, and clouds in nature occurs according to the same principle. After the aggregation, the clusters expand through the nozzle into the next vacuum chamber forming a subsonic beam. Gas-aggregation cluster sources produce continuous beams of elements with not very high boiling points (< 2000 K), usually metals. One of the first efficient gas aggregation cluster sources was developed by Sattler et al. [99]. Since then many groups use this technique. For more detailed descriptions see, for example [94, 100, 101, 102]. The cluster size distribution depends on a number of source parameters and can reach up to a few tens of thousands of atoms. However, clusters from aggregation sources can not be controlled easily with respect to their size distribution. The products tend to agglomerate to larger species, often at elevated temperatures due to the excess heat of condensation.

2.3.2. Supersonic (free-jet) expansion

Rare-gas or molecular clusters usually are produced from an adiabatic expansion through a continuously working or pulsed nozzle. The nozzle diameters range from a few µm up to 500 µm, usually restricted by the pumping speed of the apparatus. Mixed clusters are generated by a co-expansion of a gas mixture, or by using a pick-up technique with a cross-jet. Quite often the gas aggregation method is combined with the free-jet technique yielding so-called seeded supersonic nozzle sources in which a vapor of low-melting-point metals is seeded in the carrier gas at a stagnation pressure of several bars [103]. The size of the clusters may be varied by changing the nozzle temperature or the stagnation pressure. Typically, the sizes range from tens to thousands of atoms but for some sources can reach over a hundred thousand [104]. Without further size selection the width of the size distribution (FWHM) Δn is comparable to its average value n_{av}.

For a coarse size control, semi-empirical scaling laws have been derived from general considerations about condensation kinetics [105, 106, 107]. In this description, n_{av} scales with the "condensation parameter" Γ^*

$$\Gamma^* = k \frac{(p_0 \, D)^{0.85}}{(T_0)^{2.2875}} \tag{2}$$

where p_0 is the stagnation pressure (in mbar), T_0 is the nozzle temperature (in K), D is the effective nozzle diameter (in μm), and k is a gas specific constant. The gas constants can be calculated from the molar enthalpy at zero temperature and the density of the solid (see [106] for details). They range from 185 (Ne), 1646 (Ar), 2980 (Kr) to 5554 (Xe). The equation holds for monoatomic gases; otherwise the exponents of D and T_0 are different. In the case of conical nozzles, D has to be replaced by an equivalent diameter, which depends on the cone angle. The scaling laws developed for rare gases have been modified afterwards to be applied to metal vapors. More details of free-jet expansion can be found elsewhere [94, 98, 103].

2.3.3. Laser vaporization

In a laser vaporization cluster source a rotating target rod or plate of the desired material is used as the source of material for cluster formation [68, 108]. Nanosecond laser light pulses at an intensity of about 10 to 100 mJ/pulse erode the target material by producing a plasma plume, which is flushed by the carrier gas through a narrow channel (typically of 1-2 mm in diameter or even smaller) and a nozzle into high vacuum. Usually He pulses with an admixture of Ne or Ar at backing pressures of 2-20 bar serve as cooling and carrier gas. The close contact with the cold gas leads to supersaturation and efficient aggregation already in the source channel. Depending on the material and on the operation conditions, different types of nozzles are in use, partially with very long extenders of 10 cm or more. In some cases an additional small mixing chamber between source body and extender might increase the intensity within a desired mass range. Light for vaporization is usually provided by pulsed Nd:YAG or sometimes Ti:Sapphire lasers. Different photon energies can be applied as long as the intensity is sufficient to induce vaporization or create a plasma. With the laser vaporization source practically all solid materials can be brought into the vapor phase. A significant fraction (some ten percent) of the emerging clusters is charged. Thus, usually no additional ionization is necessary if experiments have to be performed on mass-selected species. The cluster size distribution depends on the source conditions and typically ranges up to a few hundred atoms per cluster [109, 110]. One of the advantages of the laser vaporisation source is that it is an easy way to produce binary clusters (consisting of two different chemical elements) using binary alloy targets of desired composition [75, 111], a dual-rod configuration [112] or even a dual-rod dual-laser technique [78].

2.3.4. Ion and magnetron sputtering

High-energy ion-surface sputtering has been an important topic in the last century. An analytical tool was developed, secondary ion mass spectrometry (SIMS), which detects secondary ions in order to reveal material composition. Whereas at energies in the keV

range the main interaction between the fast ion and the solid material can be traced back to binary collisions, the emission of clusters on impact of single ions is still not completely understood [113]. In ion-sputtering sources the projectile ions interact with clean surfaces usually under ultrahigh vacuum conditions. It has been shown that even large clusters with more than 100 atoms can emerge from a single impact, see Fig. 2 for an example on Cu_n [114].

Another type of sputtering emerges when a plasma is ignited in the presence of a rare gas (typically, argon with a stagnation pressures on the level of 0.1-1.0 mbar) in the vicinity of the target surface. The plasma is stabilized by a magnetic field. Magnetron sputtering sources have wide technical applications mainly in the thin film coating and processing industry. Their use for cluster production goes back to developments in the group of Haberland [74]. This versatile tool operates plane solid target (typically a few cm in diameter) mounted close to an axial permanent magnet. A voltage of 100-500 Volts between a ring-shaped electrode and the target initiates and drives a discharge, efficiently eroding the material and producing a circular well after several hours of operation (see Fig. 3). The eroded material is cooled by the carrier gas and transported through a nozzle. The formed clusters vary in size between several and over 10^6 atoms; 20 to 80 % of them (depending on cluster species) are ionised [74, 115]. The cluster beam flux can reach 10^{12} cluster/(cm^{2}s) [74]. Conducting and semiconducting materials can be sputtered by this type of sources, whereas ferromagnetic targets may cause some difficulties.

2.3.5. Arc discharge

In contrast to the magnetron sputtering source which operates with a high voltage discharge, arc cluster ion sources make use of high current arcs. Such are known as vacuum arcs, self-stabilizing at about a few tens of volts and a few tens of amperes. The discharge can be sustained in vacuum once a spark has initially brought some metal into the vapor phase. One has to ensure that the discharge is carried by the metal vapor rather than by the carrier gas. In order to accomplish this, the temporal development of the high voltage-driven spark needs

special care. Once the metallic component in the source determines the conductivity, the discharge voltage switches to a low level so that the carrier gas will not be ionized. Two variants of arc sources are in use, pulsed ones and continuously working ones. The concept of the pulsed arc cluster ion source (PACIS) [116, 117] is very similar to the laser vaporization cluster source, only that the laser is replaced by a pulsed high-current arc between two electrode rods at about 1 mm separation. An offspring of the PACIS uses one rotating electrode, in which case it is called a pulsed microplasma source [118]. When operated continuously we obtain the arc cluster ion source (ACIS) [119, 120]. Connected to an electrostatic quadrupole it provides a high flux of mass-filtered metal clusters in the range from ca. 2 to up to 15 nm in diameter, see Fig. 4. Here the target is a water cooled hollow cathode, a water cooled counter electrode serves as anode. Magnet coils around the hollow cathode help to control the arc. Again, the plasma is flushed by an inert carrier gas into vacuum, producing a cluster beam with a high amount (about 80 percent, depending on the material) of charged species.

2.3.6. Electrosprays and liquid metal ion sources

In the end of the 60's Dole and colleagues carried out a series of experiments in which they attempted to generate beams of charged macromolecules in vacuum [49]. Their approach was to electrospray a dilute solution of polystyrene molecules into a bath gas of nitrogen at atmospheric pressure. The idea was that as the solvent evaporated from the charged droplets the charge density on the surface would increase until the Rayleigh limit was reached. At this point the Coulomb repulsion forces begin to exceed the surface tension and the droplet would subdivide. Eventually a state would be reached in which on average each droplet would contain only one macromolecule. A decade later, Fenn and his group further developed the electrospray technique: solutions passing through a small capillary biased at 2-10 kV relative to ground are electrosprayed into a bath gas to form a gaseous dispersion of ions that is expanded into vacuum in a small supersonic free jet [50]. A portion of the jet going through a skimmer forms a molecular beam that contains a variety of ionic species.

This type of source can be used to isolate high-molecular-weight species, like e.g., proteins or clusters, from solution.

In a liquid metal ion source, a metal is liquefied and brought to the end of a capillary or a needle. A Taylor cone is formed under the application of a strong electric field. With increasing sharpness of the cone the electric field becomes stronger, eventually driving field evaporation. Technically, these ion sources are often operated with gallium and particularly used in ion implantation or in focused ion beam instruments. However, this approach is also used for production of intense cluster ion beams of different metals (Li, Cs, Sn, Ga and Hg) [54, 55, 56]. For alkali and group IV element clusters Saito et al. [121] demonstrated that the mass spectra exhibited magic numbers and signatures of doubly charged species, which hints at high energies involved in the growth process. For the purpose of cluster deposition we should note that both the electrospray and liquid metal ion sources produce strong and continuous beams which, in connection with a dc mass filter, deliver high flux mass-selected clusters.

2.3.7. Helium droplet pick-up

For experiments at ultra-low temperatures, helium droplet pick-up sources prove to be very versatile. He droplets are produced by the supersonic expansion of pre-cooled helium gas with a stagnation pressure of about 20 bar through a 5 µm diameter nozzle [122, 123, 124]. By choosing the temperature at the orifice (8-14 K), the log-normal droplet size distributions can be adjusted in the range of $n_{average} = 10^3$-10^7 atoms. After passing differential pumping stages the beam enters the pick-up chamber containing a gas target or a heated oven, where atoms or molecules are collected and aggregate to clusters inside the He droplets. With this setup it is possible to record clusters with e.g. up to 150 silver atoms [125] or 2500 magnesium atoms [126]. Downstream of another differential pumping stage the doped droplets are ionized by laser light or an electron beam. The resulting charged products are detected by a mass spectrometer, typically using reflectron time-of-flight (TOF) method, having a sufficient resolution ($\Delta m/m \sim 10^{-4}$) to distinguish between different charge states

and even to resolve isotope compositions. The benefits of pick-up sources rely on the feasibility to embed the cluster into a well-controlled environment. In the case of He, the embedding medium is weakly interacting, ultracold (ca. 0.4 K) and superfluidic [127], thus being an ideal matrix for spectroscopic studies [128]. Similarly, droplets or particles of other elements might serve as a pick-up medium, e.g. Ar, Kr, or Xe. Subsequent atom agglomeration inside the droplet can lead to the formation of electronically excited species [129].

Whereas the helium droplet pick-up sources so far have mainly served to prepare ultracold targets for spectroscopic purposes, the use for depositing clusters embedded in soft encapsulating shells has scarcely been tested. In fact, with a helium droplet velocity of about 200 m/s and the extreme high capability of He atoms to cool away any thermal excitation an ultrasoft deposition becomes possible. At the same time, as the He can be pumped without contamination of the system, this method is free of any surface damage. The group of Vilesov studied the utility of He droplets for depositing large molecular and atomic clusters [130]. For gold and silver clusters they demonstrated that a flux of about 10^{11} atom/(cm^{2}s) could be obtained, which is sufficient to reach a monolayer equivalent coverage within about 100 minutes. However, so far no source optimizations have been performed in order to increase deposition yields; an increase by one or two orders of magnitude should be possible.

2.4. Size selection of clusters

As follows from the previous sections, clusters produced by means of different sources usually have a wide size distribution. In most of the experiments and for many practical applications, the clusters must be mass separated (size selected). Methods applied for the size-selection depend on the charge state and mass range of the clusters.

2.4.1. Neutral cluster beams

Gas aggregation or adiabatic gas expansion *per se* do not lead to formation of charged particles. Thus, means of size selection have to rely on separation, for instance, through a difference in momenta or velocities. One of the methods, exploited by Buck and Meyer, is based on the scattering of a cluster beam from an atomic beam at an intersection angle of 90°: the heavier clusters are scattered into smaller angles with smaller final velocities compared to the lighter ones [131]. This technique was successfully applied in experiments with small (a few atoms or molecules in size) atomic and molecular clusters [132].

Another approach relies on aerodynamic focusing of the beam containing different-sized particles. At the beginning of a free expansion through a nozzle, the clusters possess not only velocities directed along the nozzle axis but also outward radial velocities. The clusters outgoing close to the nozzle edge experience the strongest radial drag. Thus, clusters expanding through the central part of the nozzle and those close to the edge will have significantly diverse trajectories. Since the effect of the radial drag is size-dependent, it can be used for size separation of the clusters. This approach was used for the first time in the early 60's: particles travelling along the main axis of coaxial capillaries formed a very well collimated beam [133]. In the 90's this idea was further developed into a system of aerodynamic lenses [134, 135]. The principle of aerodynamic size-selection is demonstrated in Fig. 5 [136]. The inertia of large particles having Stokes number St >> 1 exceeds the drag action of the central gas flow that leads to their deposition on the walls. Very small particles with St << 1 closely follow the gas flow and become trapped in the vortices. Thus, only the particles with St ~ 1 join the central beam and can pass through a set of lenses as shown in Fig. 6 [137]. By varying the lens geometry and parameters of the gas flow it is possible to use the set of aerodynamic lenses as a low-resolution mass filter of neutral clusters. Recent experiments and simulations in this direction showed focusing capabilities of nanoparticles with sizes in a rather wide range from ca. 30 up to 700 nm [138, 139]. The possibility to collimate even smaller particles (< 20 nm in diameter) was shown by the example of a Cu_n beam produced by means of an ACIS [140]. In this case both neutral and charged clusters

were aerodynamically focused. It was found that the presence of the lenses significantly increased the intensity of the beam in addition to influencing the size distribution of clusters due to two factors: (i) the particles having Stokes numbers ≈ 1 have the highest collimation efficiencies for the used lens configuration (maximum around 13 nm in Fig. 7(a)); (ii) insertion of the lens system directly after the nozzle decreased the pumping efficiency and led to a pressure rise and corresponding reduction of the cooling rate (giving a maximum around 3 nm in Fig. 7(a)).

A different type of aerodynamic size-selection was suggested by Piseri et. al [141]. They positioned an analogue of a revolver drum called a focuser in front of a capillary nozzle as shown in Fig. 8. In this system the particle flow undergoes two 90° turns to reach the nozzle inlet. The mechanism of size selection is demonstrated in panel (c) of the figure: at a given pressure only particles with appropriate size (mass) have trajectories close to the nozzle main axis and can pass through. Compared to the aerodynamic lens system shown in Fig. 6, the clusters approach the nozzle inlet with a more uniform velocity and they experience a more uniform acceleration. This design is also claimed to be less sensitive to the upstream position of the clusters. This type of mass filter is very compact.

2.4.2. Charged cluster beams

A significant fraction of clusters produced by means of surface erosion (in arc discharge, laser ablation and ion sputtering) or spray sources typically is ionized. Both positively and negatively charged cluster ions can be formed. Depending on cluster species, up to 80% of the emitted material can be charged, for instance in the case of magnetron sputtering [115]. However, in most cases this ratio is about 10-20%. To increase the fraction of the charged clusters or to produce them from a neutral beam, post-ionization can be employed. There are a few methods used to generate cations. One of them is electron impact ionization. This approach uses either thermal electrons or a focused accelerated electron beam interacting with the cluster beam. Another possibility is photoionisation where laser or other intense light beams (e.g. synchrotron radiation) are used for cluster excitation. Positively charged clusters

can also be generated by electric discharge. This method is used only for free jet sources where a corona discharge occurs within the stagnation chamber, prior to the expansion. To generate anionic clusters, a method of electron transfer is typically used (although anionic clusters can also be extracted directly from laser vaporisation or other sputtering sources). Electron attachment cab occur e.g. via collisions with alkali metal atoms in the vapour phase. The disadvantage of this ionisation method is the possibility of alkali metal inclusion into the clusters.

A range of mass separation techniques are available for the charged clusters. The choice typically depends on the required precision of the mass selection. Very tight size selection is able to resolve and separate clusters with a precision of 1 a.m.u. However, such high resolution was achieved for sizes of only up to a few tens of atoms depending on the atomic mass of the cluster species corresponding to a mass resolution $\Delta m/m$ of the spectrometer of ca. 10^{-5}-10^{-3}. The lower limit of the resolution interval can be achieved using linear TOF mass spectrometers, for instance in a Wiley-McLaren configuration [76, 142]. To reach the level of 10^{-5} the TOF must be used in a reflectron configuration [143].

However, for many practical applications like cluster deposition such high mass resolution is not required. Instead, the possibility to select clusters with lower precision but from a broad interval of sizes is desirable. One of the examples is a magnetron sputtering source combined with a novel high transmission TOF system providing a constant mass resolution $\Delta m/m \sim 4 \times 10^{-2}$ over a broad range of cluster sizes from 2 to at least 70000 atoms [144]. The idea of size selection is the following: the cluster beam, entering the TOF in the horizontal direction, experiences a vertical acceleration and then moves diagonally in a field-free region. A horizontal slit is then used to select the required mass. The use of perpendicular deflection, rather than the acceleration in the direction of the beam, as in a conventional TOF, means that the resolution of the TOF is constant over the entire mass range, since the incoming beam has practically no perpendicular velocity component.

Another widely-used type of mass filter is a radiofrequency (rf) quadrupole spectrometer (Fig. 9). Typical mass resolutions of modern quadrupole spectrometers are around 10^{-4}-10^{-3}

[145]. In combination with cluster sources, this type of size selection is often used as a band-pass filter with a variable bandwidth. The pass condition is defined by following equation [146]

$$m = \frac{V}{7.219v^2r_0^2} \qquad (3)$$

where m is the mass of the passing particle, V is the voltage applied to the rods, v is the frequency of the rf field applied to the rods and r_0 is the distance between the main axis and the edges of the rods as shown in Fig. 9(b). It is clear from the equation that the pass condition is a function of the voltage, frequency and distance between the rods. It is possible to pass arbitrarily large masses but the resolution deteriorates. A maximum mass range of 60000 a.m.u. with a resolution of about 200 a.m.u was reported [102]. Even higher mass ranges up to 10^6 a.m.u. can be reached in modern quadrupole spectrometers but the mass selection is relatively poor ($\sim 10^{-2}$) for such heavy clusters.

Another mass selecting approach relies on the deflection of the charged clusters in an electrostatic field. An electrostatic quadrupole spectrometer is schematically shown as a part of the setup in Fig. 4. The main parts of the spectrometer are four electrodes, each having the shape of a quarter cylinder. The electrodes are divided into two pairs which are biased with the same absolute voltages but opposite polarities. The clusters produced by a source typically have the same velocities but different mass-to-charge ratios. Thus, they will be deflected to different angles in the electrostatic field of the spectrometer. By adjusting the voltage, clusters of desired size can be deflected by 90° to leave the spectrometer and enter the deposition chamber. Fig. 10 shows an example of Ag_n clusters deposited from an ACIS using two settings of the static quadrupole deflector voltages. Obviously, just by choosing the voltage a desired particle size can be obtained. These selections are useful for high throughput but they do not provide very high mass resolution.

One more commonly used type of mass spectrometer is the Wien filter in which mass separation is accomplished with crossed homogeneous electric and magnetic fields

perpendicular to the cluster beam [147]. For clusters, a typical resolution of $\approx 10^{-2}$ for the mass range up to ca. 4000 a.m.u was reported [148]. At the same time the device could be used as a band-pass filter for much larger cluster sizes.

Exhaustive reviews on these and some other mass-selecting techniques can be found in [1, 14, 27, 76, 145].

3. Cluster-surface interaction

One of the important parameters in the application of cluster beams is the kinetic energy E_{kin} which defines the appropriate regime of the cluster-surface interaction. In this paper we divide the cluster-surface interaction processes into *low- and high-energy* ones. An interaction is considered to be *low-energy* when the kinetic energy per atom E_{at} is below the binding (cohesive) energy of the cluster constituents E_{coh} (which is typically below the level of eV/atom). This case is often called deposition or soft landing (Fig. 11(a)). The deposition typically does not induce cluster fragmentation, i.e. the clusters preserve their composition. At the same time, the structure can be distorted. In other words, the cluster can undergo a plastic deformation especially if E_{at} is close to E_{coh} or if atoms of the deposited cluster strongly interact with the substrate atoms. If E_{at} exceeds E_{coh} the impact is considered to be *high-energy*. Under such impact regime, there are a few possible scenarios. If E_{at} is only slightly above E_{coh} the cluster is significantly plastically deformed on impact but it fragments only partly and most of its constituents remain intact. A further increase of E_{kin} leads to cluster decomposition and fragmentation. Cluster fragments can be either backscattered from the surface or implanted into the substrate. For the latter case, the energy locally transferred to the surface must be higher than the penetration threshold energy – the energy which is required to displace the host atoms from their binding sites. Thus, the implantation always leads to the formation of collision-induced damage of the substrate (Fig. 11(b)). In the case of relatively high E_{kin} the impact can also lead to significant erosion such as sputtering of surface atoms and crater formation. Thus, by varying the cluster kinetic energy one can

develop different methods for synthesis and modification of materials. The different energetic regimes of cluster-surface interactions are discussed in detail below.

3.1. Cluster deposition

3.1.1 Soft Landing

Much of the effort in the field of soft landing is driven by the idea to maintain the unique properties of size-selected clusters and immobilize them at the surface for investigation or potential applications. In particular, at low E_{kin} material exchange between cluster and substrate, as well as fragmentation can be reduced or prevented [11]. Typical limits that can be found in the literature are around $E_{at} \approx 0.1 eV$. However, the general conditions required for soft landing are difficult to specify since the process strongly depends on cluster size and material, as well as the substrate properties like surface energy, hardness, corrugation, polarizability and temperature [149].

As a starting point, small clusters consisting of well below 100 atoms are discussed. Density functional calculations of Ag and Pd tetramers adsorbed on MgO suggest an almost unperturbed configuration compared to the gas phase [150]. MD studies of the deposition process support this scenario [151]. In contrast, on metal substrates small clusters may easily change their structure upon contact with the surface because of the dominant role of the cluster-surface interaction energy. This is the energy gain compared to the situation of a cluster separated from the surface and it depends on the binding energy of the cluster constituents to the surface, as well as on the surface and interface energies. In the case of Ag_7 and Ag_{19} deposited on Pd(100) and Pd(111) MD simulations have shown that even at very low E_{kin}, close to zero, partial implantation and atomic site exchange occur [152]. Pronounced atomic rearrangement but no significant atom exchange has been found for Cu_n and Au_n up to $n = 55$, deposited on Pd(100) at negligible kinetic energy [153]. Furthermore, the degree of wetting increases for high substrate temperatures or for deposition at step edges. For these small clusters major restructuring is inevitable such that soft landing does not necessarily preserve the properties of the free particle. Implications of the cluster-surface

interaction for the structure of small clusters have been intensively discussed in recent years, particularly in the context of potential catalytic applications [154, 155, 156].

For larger clusters with several hundreds or thousands of atoms the situation changes because the cluster-surface interaction energy becomes less important compared to E_{kin}. On weakly attractive surfaces clusters may even be reflected for certain ranges of the kinetic energy [157, 158]. This question will be addressed in section 3.2. On adhesive surfaces the thermodynamically stable structure, particularly for many metal clusters on metal surfaces, is that of a flat monoatomic film. At low enough temperature a metastable three-dimensional structure may be stabilized. For such wetting systems an increase of E_{kin} leads to a temporary rise of temperature that accelerates the cluster evolution towards the final configuration. Thus, the shape as measured experimentally or determined by MD calculations changes with increasing impact energy. Simulations of the deposition process of Cu_{1289} on Au(001) resulted in substantial particle flattening at $E_{at} = 100$ meV while only slight deformations have been observed for $E_{at} = 1$ meV [159]. At elevated impact energies, partial implantation can also occur for large clusters. Simulations of the impact of $Ag_{500}Co_{500}$ core-shell clusters reveal that even at $E_{at} = 250$ meV a few percent of the atoms are shallow-embedded while the core-shell structure is preserved [160]. The authors have not found a pronounced size dependence but the degree of implantation increases with kinetic energy, reaching almost 30% for $E_{at} = 1$eV. This phenomenon is discussed in more detail in section 3.3.

With increasing E_{kin} the system is allowed to progress towards energetically more and more favorable configurations. This is also reflected by the degree of epitaxy between cluster and surface, specifically if cluster and surface are of the same material. Early MD simulations showed that Cu_{87} and Cu_{959} deposited on copper at $E_{at} = 200$ meV develop a large degree of epitaxy [92]. The smaller clusters even recrystallize after their internal structure has been temporarily destroyed by the impact. A widely-used measure for the general shape of a particle is the aspect ratio, i.e. its lateral diameter d divided by its height h. Experimentally, the aspect ratio of deposited clusters is accessible for instance via the combination of

transmission electron microscopy (TEM) and scanning tunneling microscopy (STM). Au_n (n ≈ 750) deposited on Au(111) with E_{at} between 0.25 and 1.25 eV show a high aspect ratio of >4 indicating considerable deformation [161]. Simulations for Au_{440} (E_{at} = 0.25eV) landed on Au(111) reveal deformation as well, albeit with a smaller aspect ratio [162] (see Fig. 12). For bimetallic $Pd_{1-x}Ag_x$ clusters deposited at 50 meV on Pd(100) the different melting points and atomic radii of the metals affect the diffusivity of the individual atoms and result in pronounced wetting and epitaxy of the clusters [163]. Also, cluster temperature plays a crucial role for relaxation of the cluster/surface system. Whereas the degree of epitaxy at 300 K is about 70% for $Pd_{50\%}Ag_{50\%}$ clusters (≈1500 atoms) on Pd(100), it shows almost full epitaxial alignment at 1300 K [163]. In general, smaller clusters exhibit epitaxial order with respect to the symmetry of the underlying crystal already at lower temperatures compared to larger ones. This has been shown, for example, by reflection high energy electron diffraction (RHEED), where smaller Fe_n (4 nm in diameter) were partially oriented with respect to a W(110) substrate [164]. Larger particles (13 nm in diameter) needed to be annealed to achieve epitaxial alignment (Fig. 13) [165].

Since cluster properties are affected by the detailed structure of the cluster/substrate interface, atomically well-defined surfaces are needed for experimental investigations. While these conditions can be reached rather easily for chemically inert substrates like highly-ordered pyrolytic graphite (HOPG) or noble metals, more reactive surfaces require extremely clean vacuum conditions, particularly during the deposition process. As an example, for Ag_n (diameter of 6 nm) deposited on Si(111) (E_{at} ≈ 0.02 eV), the 7x7 surface reconstruction has been preserved upon cluster deposition as demonstrated by atomically resolved STM images (Fig. 14) [166].

Epitaxy is not only achieved through the initial heating at impact but also due to movement of atoms on a longer time-scale. The migration of twin boundaries at the interface between epitaxial and non-epitaxial parts of the cluster has been identified as a dominant effect for Cu_n, Ag_n, Au_n, Ni_n, and Pt_n (n = 6-2000) on a surface of the same material [167]. The influence of the surface lattice on the cluster has been studied in the case of large Au_n,

consisting of up to several thousand atoms, on MgO by cross-sectional high-resolution transmission electron microscopy (HR-TEM) [168]. These clusters exhibit a well-defined shape even at E_{at} = 0.5 eV.

While structure, alignment, deformation and wetting can be studied in detail using theoretical methods like MD simulations, experimental studies are restricted to the final state of the cluster. They also require rather special circumstances to access such information. Most data are available for clusters deposited on carbon which can be used directly for TEM investigations. Recent developments in HR-TEM allow for reconstructing the three-dimensional shape of individual nanoparticles with atomic precision [169]. For the precise structural determination of clusters deposited on other substrates a variety of methods has been applied, including the analysis of facets visible in TEM [168] or STM images [170], in-situ RHEED measurements [164], decoration of small clusters with rare-gas atoms [171] or the combination of different microscopy techniques.

The kinetic energy range for soft-landing conditions is considerably extended if the cluster is allowed to gently dissipate energy in a controlled fashion prior to substrate contact. A popular example is the use of buffer layers which typically consist of thin rare-gas films. MD simulations have shown that small $(NaCl)_n$ can be landed without fragmentation or implantation even at kinetic energies of 2.72 eV per NaCl molecule if a rare gas buffer layer on top of the substrate is used [172]. Similar results have been obtained by the same group for Cu_{147} deposited in rare gas films on Cu(111): while the clusters can be soft-landed on the surface in the presence of the film, their initial structure is completely destroyed upon impact at E_{at} = 5.3 eV on bare Cu(111) [173]. A direct comparison of Ag_7 deposition at E_{at} = 2.9 eV with and without an Ar buffer layer (of 10 monolayers thickness) on Pt(111) confirms that this technique is applicable to small metal clusters as well [174]. The clusters do not suffer fragmentation on the Ar covered substrate and neither do they form surface defects that act as pinning centers, as in the case of the bare substrate. On the other hand small clusters are more affected by the rare gas layer itself. Ag_n (n = 2…7) deposited into rare-gas matrices show a considerable amount of fragmentation within the rare-gas film in the energy range

2.5-50 eV [175]. Even if the cluster survives the impact into the rare-gas layer without major structural rearrangements this does not prevent the cluster from restructuring after rare-gas desorption due to cluster-surface interactions as e.g. shown for small Fe clusters soft-landed on an Ar layer on (2x1)O/Ru(001) [176].

The concept of a buffer layer can also be extended to other weakly interacting materials beyond rare gases. As an example, C_{60} molecules adsorbed on Au(111) were used for the controlled deposition of size-selected Ag_{561} [177]. The C_{60} layer decouples the clusters from the metal substrate and reduces particle flattening. Nevertheless the particles start to decay upon annealing by penetrating the one monolayer thick C_{60} coverage atom by atom until a metastable configuration is reached [178]. In this case the final cluster size and geometry can be substantially different from the deposited particles, in spite of soft landing.

3.1.2 Diffusion, agglomeration, and coalescence

Self-assembled nanostructures and clusters at surfaces are produced by exploiting the diversity of physical effects that are based on diffusion of single atoms. Likewise, during the formation of free clusters (inside a source), diffusion of atoms on the cluster surface plays an important role. Many of the restructuring processes discussed in the previous section can be viewed in terms of atomic diffusion. Apart from the motion of single atoms, diffusion of larger aggregates has been observed as well. The movement of two-dimensional adatom islands has been widely studied [179, 180, 181, 182]. Similar processes can also occur for three-dimensional clusters at a later stage after deposition when the particles have reached a more or less stable configuration on the substrate but still are allowed to propagate across the surface. Since the activation barrier strongly depends on the cluster-surface bonding, cluster diffusion is favored on weakly interacting materials, such as graphite or amorphous carbon. For a review see [81].

Movement of particles on the surface can lead to coalescence or agglomeration. Coalescence of two (or more) particles leads to their merging and the formation of a single larger particle with potentially different shape as shown by example of scanning transmission

electron microscopy (STEM) micrograph presented in Fig. 15(a) [183]. Agglomeration, on the other hand, is observed mostly for larger particles or low temperatures and results in immobilization, for instance by formation of ramified islands (see atomic force microscopy (AFM) image presented in Fig. 15(b)) [8], while preserving the individual cluster shape. Nucleation and growth of agglomerates depend on the surface mobility and sticking coefficient of the clusters. It was suggested by A. Perez et al. [8] that the transition from coalescence to agglomeration of diffusing clusters occurs at a critical size.

The coalesced particles can exhibit altered electronic properties compared to the constituents, particularly if several particles merge to a single object. Thus, evidence for diffusion can be obtained from spectroscopic methods. By comparing spectra of the corresponding bulk material to those of different cluster samples, ultraviolet photoelectron spectroscopy has been used to identify substantial diffusion of small Ag_n (n = 1…5) on HOPG even at temperatures as low as 70 K [184]. In a further photoemission investigation, Ag_{55} and Ag_{923} have been deposited onto HOPG [185]. The mean density of the statistically distributed landing sites was low enough to expect the presence of well-separated particles throughout these studies. Nevertheless, for elevated coverage the clusters showed a pronounced tendency for coalescence at $T = 50$ K and $T = 100$ K, respectively. Interestingly, even large Sb_n and Au_n up to n = 2300 diffuse rapidly on graphite [186]. The authors propose a mechanism based on rotations of the entire cluster on the surface. Indeed, a combination of rotations and translations has been identified by MD studies as the dominant mechanism for the motion of Au_n on graphite (Fig. 16) [187]. The exceptional high mobility on flat surfaces can also be ascribed to the total energy landscape of the cluster propagation across the surface. Since activation barriers are particularly small if the atoms in the contact facet are not in registry with the surface, such incommensurable states result in efficient diffusion. Transitions back to an aligned, "sticking" state are relatively unlikely due to the large configuration space of the system [188, 189]. This mechanism is very different from the simple diffusion of single adatoms. Regarding more general properties, though, the motion of large clusters shows strong similarities to adatom diffusion: based on MD simulations it was

found that the diffusion rate for Au_{249} on graphite is comparable to that for single adatoms [190]. Another analogy to adatom diffusion is the formation of a barrier similar to the Schwoebel effect at step edges that was found for Au_n on graphite, both experimentally [186] and in simulations [191].

The versatility of sample preparations based on diffusion is generally limited by its statistical nature. Cluster agglomeration typically results in structures without preferential directional growth. But the diffusion can be guided by the presence of steps or a finite curvature on the sample. Ag_n with a mean diameter of 3 nm deposited on HOPG behave like a one-dimensional particle gas in narrow areas between concave bends [192]. Within such regions they can form one-dimensional chains of agglomerated particles (Fig. 17).

For potential applications, sample preparation at room temperature is often inevitable while aggregation of clusters must be avoided. Instead of introducing pinning centers on the sample the modification of a cluster via collision with another, smaller cluster may provide an interesting route as shown by MD simulations of Au_n and mixed cluster systems [193]. Efficient immobilization at room temperature has been obtained after collision of Au_n with a small cluster containing a different metal. The authors suggest the formation of pinning centers due to the locally distorted structure of the merged particle as a mechanism for the reduced diffusivity.

Compared to graphite, on other substrates like metals or many oxides the lateral diffusion of metal clusters is less likely because the interatomic interactions are comparable inside the cluster and at the cluster-substrate interface. Nevertheless, considerable diffusion rates have been observed for small Pt_n (n = 2,3) oligomers on Pt(001) at $T = 175$ K. In fact the mean-square displacement of the dimer was more than 50 times larger compared to the monomer [194]. The low activation barrier is explained by a weakening of bonds due to the larger coordination compared to the monomer. In this case the monomer and dimer motion is based on atom exchange with the substrate, while the trimer combines conventional hopping with exchange displacements. A number of different diffusion mechanisms has also been found for Ni_n on Au(110)-(1x2) by MD simulations [195]. While dimers propagate by

conventional jumps, trimers can diffuse via in-plane rotations. Surprisingly, larger clusters like Ni_4, Ni_7, and Ni_{13} with more and more spherical shape can roll on the surface which leads to enhanced diffusion. A similar mechanism has been found for Pd_n (n = 2-4) on MgO(100), also by MD simulations [196]. As a result the activation barrier remains similar for all investigated oligomer sizes (n < 5), including the monomer. But small clusters do not always show such pronounced diffusivity. On (2x1)O/Ru(001) even Fe trimers soft-landed on an Ar layer are found to be relatively stable against diffusion at temperatures up to 400 K, whereas Fe monomers are highly mobile already at T = 150 K [176].

3.1.3 Cluster Assembled Materials

One of the advantages of the cluster beam technique compared to ion or molecular beam methods is that the mechanism of cluster formation inside the cluster source is decoupled from the substrate properties. This advantage allows for deposition of thin films by cluster beams where the structure of such films can be controlled by varying the cluster kinetic energy. For instance, for Mo_n deposited on a Mo surface, MD simulations showed that at E_{at} = 0.1 eV porous films can be grown in which the clusters are gently stacked one above the other (Fig. 18) [21]. At E_{at} = 1 eV epitaxial layers with good adhesion to the surface were observed, where the density reached 80% of the bulk material. A further increase of the cluster energy up to E_{at} = 10 eV led to the complete decomposition of the clusters and the formation of a denser film with better adhesion because of the strong intermixing between cluster and substrate material within a few atomic layers. This intermixing regime was experimentally demonstrated by deposition of very smooth (roughness of 0.7-1.5 nm), dense and strongly adhering coatings on Si, quartz and steel substrates using Al_n^+, $(TiN)_n^+$ and $(TiAlN)_n^+$ cluster ions with energies of E_{at} = 5-20 eV [24].

In a joint experimental and theoretical study Au_n (diameter of 2.9 nm) deposited on Au(111) were compared to MD simulations at E_{at} = 0.25 eV [161]. Neither diffusion, nor coalescence was observed, and the film morphology was similar to the case of molybdenum mentioned above (see Fig. 18(a)). Another interesting question is whether the chemical

identity of bimetallic clusters is changed upon formation of a film by cluster beam deposition. As an example, the film properties of assembled Ni-Al clusters have been investigated by MD simulations [197]. No intermixing is found on Ni and Ni_3Al surfaces, and the intermixing on Al reaches a depth of 1nm. The clusters keep their chemical identity with a crystalline core, independent of the impact energy within the investigated range of $E_{at} = (0.25...1.25)$ eV. The high surface-to-volume ratio of porous nanoparticle films obtained by low-energy cluster deposition is often accompanied by poor mechanical properties. It was proposed that such films could be improved by ion-induced densification [198]. Using MD simulations the authors could show that after bombardment with Xe and Au ions the initial mean density was greatly enhanced while nanocrystallinity and the structure of the substrate were still preserved. If cluster-cluster interaction is undesirable, as e.g. for magnetic applications, they can be co-deposited with other materials, resulting in decoupled clusters embedded in matrices (see e.g. [199] for a review).

In a typical cluster deposition experiment, the landing sites on the substrates cannot be controlled directly but the spatial cluster distribution is of statistical nature. On the other hand, often a well-ordered alignment of clusters is of interest, particularly in view of potential applications. One possible route is to use a shadow mask which transmits clusters to the substrate only within restricted areas. By deposition of neutral carbon clusters it was possible to grow patterns of three-dimensional objects using such a mask (Fig. 19) [200]. This method of formation of patterned carbon dots on a silicon surface followed by thermal annealing was later employed to obtain arrays of SiC dots [201].

Utilizing site-selective cluster adsorption the structure size can be reduced down to a range below 100 nm: deposition of metal clusters on lithographically patterned surfaces was demonstrated by Reichel and co-workers [202]. Based on the fact that adhesion on a polymer is much weaker than on SiO_2 and Si_3N_4 substrates, they could for example prepare Bi cluster-assembled nanowires on such materials (Fig. 20).

One route towards the idea of controlling the arrangement of single clusters on a substrate might be to make use of the cluster diffusion kinetics. Mobile clusters on weakly

interacting substrates can be immobilized by defects, such that the problem reduces to the production of well-controlled defect patterns. One example showing self-organized cluster array formation has been presented for Au_n deposited on prestructured HOPG with arrays of defects generated by focused Ion beam lithography [203]. The clusters could be trapped at the defects with high probability, while the number of clusters per defect varied since it is still determined by a statistically distributed occupancy. Ordered arrangements based on self-organization of diffusing nanoparticles have also been achieved on triblock copolymers (SBS) [204]. Patterned SBS copolymer scaffolds were produced by self-assembly. Deposited Ag_n formed an ordered pattern along the scaffolds. Upon annealing, these cluster patterns were more stable than clusters deposited on unstructured substrates.

Interestingly, the diffusion of clusters on a substrate can lead to arrays even without a structured template: closed-packed and well-separated clusters have been observed in experiments with Pt_n diffusion on amorphous carbon [205]. Besides ramified islands as discussed in 3.1.2 also compact aggregated structures have been produced (Fig. 21). Due to a short-range repulsive interaction between the clusters they keep a certain distance to each other. The precise control of such repulsive forces appears to be a key ingredient for the production of dense nanocluster arrays with long-range order.

Cluster beam deposition techniques have also attracted considerable attention because of a variety of promising technical applications. They became of increasing interest with intensive development of sub-micron and nano-electronics. For example, growth of good-quality Ge layers with a thickness of 100-400 nm on a Si substrate was reported using a germanium cluster beam at supersonic velocities [206]. The results were obtained at a temperature of 500 ^{o}C, which is lower than the critical temperature of epitaxial growth by molecular beams or chemical vapor deposition. Generally, for appropriate E_{kin} the impact area can be locally annealed without heating the entire sample.

Nanostructured carbon films were proposed as promising materials for electron field emission applications and the production of cold flat cathodes. Their advantages compared to conventional materials are in lower threshold fields and saturation current densities as well

as in higher site emission densities [207]. The cluster beam technique can be used to produce exotic carbon allotropes: although the existence of crystalline carbyne is strongly debated, carbine-rich solids have already been synthesized mainly based on chemical methods [208]. The deposition of pure carbon clusters from a supersonic beam provided experimental evidence for the possibility of producing a carbyne-rich pure carbon solid [209].

Deposition of fullerenes for thin film formation or following production of fullerene-based compounds is of considerable interest for practical applications. For example, C_{60} has shown high field effect mobility as an *n*-type material making fullerene films interesting for organic-based transistors and diodes [210, 211]. It was shown that incorporation of fullerenes increases the efficiency of organic photovoltaic devices and solar cells [212, 213]. However, utilization of fullerenes for practical applications still requires deeper knowledge and control of the physical properties of such systems. Despite many years of study, the understanding and control of the electronic and dielectric properties of "buckyball" systems, endohedral fullerenes (fullerenes with encapsulated atoms) and fullerene/metal interfaces is still challenging [214, 215, 216, 217].

The use of cluster-assembled TiO_2 films, which demonstrate good adhesion of different macromolecules such as DNA, proteins and peptides, is suggested for the integration of cell cultures on micro- and nano-devices [218]. Pd_n deposited on PMMA using supersonic beams showed an unexpected evolution, in particular, they were found to penetrate into the substrate to the depth of several tens of nm (Fig. 22) [219]. The physics of this phenomenon is not well understood but the obtained results suggest that cluster beams could be a promising tool for the fabrication of metallic micro- and nano-structures on flexible polymer films.

The cluster beam deposition technique was also shown to be an efficient and powerful tool for fabrication of organic (for instance, polyethylene and 2-methyl-4-nitroaniline) thin films and various inorganic-organic complex nanometer-scale functional structures, see for example review [82]. In particular, advantages of the cluster beam method are in (i) deposition of organic materials with high melting point, in organic solution, and even those

insoluble in acids and alkalis, (ii) cleanliness of the processes which are carried out in high vacuum. Soft landing of organometallic or organic compounds produced by cluster techniques are often used in surface chemistry, see for instance [220] as an example of soft-landing experiments of vanadium-benzene clusters.

Cluster ion beam processing in conjunction with other methods may provide the opportunity to realise otherwise difficult to obtain compositions and material phases or required structures and film parameters. Cluster ion beam-assisted deposition has been used, for example, for the growth of high-quality, thin and smooth films of ITO [221], Ta_2O_5, Nb_2O_5 [222] and TiO_2 [223]. The formation of smooth thin films as components of complex glass/polymer/metal oxide heterojunction systems in the fabrication of light-emitting devices was also shown to be an advantage of cluster beam technique [224]. Deposition of clusters was used for the formation of diluted magnetic semiconductors. The advantage was in the possibility to overcome the solubility limit of certain chemical elements in a matrix. Using this approach $Ge_{1-x}Mn_xTe$ films with tunable magnetic properties were produced. The magnetic properties were controlled by varying the Mn content over a wide interval in the clusters formed in an aggregation chamber [225]. Ionised cluster beams with low acceleration energy were shown to be useful for preparing transparent TiO_2 thin films for the efficient photocatalytic degradation of pollutants diluted in water and air [226]. The combination of this method and metal ion (V^+, Cr^+, etc.) implantation can be used to produce TiO_2 thin films that are able to operate not only under UV light but also under visible light irradiation [226]. Carbon nitride films exhibiting an extremely high hardness and low initial and steady-state friction coefficients as well as low wear rates were obtained by a reactive ionised cluster beam technique where the carbon clusters pass through a reactive gas (N_2) and the resulting particles are deposited on the substrate [227]. Semiconductor nanoparticles are of great interest for photovoltaic applications. Co-deposition of PbS_n clusters (mean diameter of 2.9 nm) and an organic matrix (titanyl phthalocyanine and α-sexithiophene) resulted in densely packed, yet well-separated clusters embedded in the organic films [228]. Such

hybrid materials may improve the low efficiency of organic solar cells as sensitizers for the near infrared region of the solar spectrum.

3.2. Cluster scattering, fragmentation and impact chemistry

In the previous section, we mainly considered cluster soft-landing. Here we discuss cluster impact processes with higher E_{kin} which is transferred to a subset of specific modes of both the cluster and the surface atoms at the moment of impact. Fig. 23 depicts possible scenarios of cluster-surface impact with increased E_{kin} [229].

If E_{at} is close to the cohesive energy but does not overcome it, the cluster is plastically deformed on impact but will still be intact. It will stay on the surface in the case of severe binding to the surface atoms. Alternatively, it can rebound (be non-dissociatively scattered). The excess energy gained by the impact is rapidly transferred into the internal degrees of freedom that leads to the vibrational excitation of the rebounded cluster. A good example of non-dissociative cluster scattering is fullerene-surface collisions due to the relatively high binding energy of the C_{60} (on the level of 10 eV) compared to other cluster species. In the experiments and modelling of the interaction of C_{60}^- with Si(100), it was found that the fullerenes are resistant to fragmentation up to an energy of ca. 170 eV/cluster ($E_{at} \approx 2.8$ eV) and the rebounded clusters acquire 10-30 % of the E_{kin} as vibrational excitation that in turn can lead to thermionic or delayed electron emission from the vibrationally excited C_{60}^- [230, 231, 232]. The modelling [231] also demonstrated that at $E_{kin} = 250$ eV, the scattered fullerene possesses a vibrational energy of 30-60 eV being equivalent to an effective temperature of 2000-4000 K. The cluster can survive without fragmentation on the time scale of about 1 μs.

Compared to the case of non-dissociative cluster scattering, there are many more investigations of scattering followed by fragmentation. Depending on the cluster species and their E_{kin} as well as on the type of surface and its temperature, there are several possible scenarios leading to the cluster dissociation such as evaporation, fission, cleavage and

shattering. Below, we will mention some of the main phenomena. For a more extensive review on this topic see [229].

Chatelet and co-workers have carried out a series of studies of large clusters of inert gases scattering off HOPG surfaces at thermal impact velocities (ca. 500 m/s), see for instance [233, 234, 235, 236]. They have found that the clusters hitting the surface at small angles glide on it leading to the following main fragmentation channels: monomer evaporation from the gliding cluster; temporal trapping of cluster atoms by the surface with their subsequent thermalization and evaporation; splitting of gliding clusters into large fragments (these fragments were found to leave the surface at angles close to the surface plane).

Experiments on small Al_n colliding with silicon at an energy of 80 eV showed that the dissociation involves not only sequential evaporation of atoms but also production of small fragments. The fragments leave the surface at a thermal velocity determined by the local temperature upon surface impact [237]. Bernhardt and co-workers demonstrated with the example of small Bi_n and Sb_n impacting on HOPG that at $E_{kin} < 75$ and 150 eV for Bi and Sb, respectively, the fragmentation pattern is very similar for both species but it becomes different at higher energies. This observation is probably related to the stability of different fragment sizes [238]. Later, it was shown by Tai and Muracami that Sn_n^+ prefers to fragment by fission [239].

Shattering of the impacting parent cluster ions into small molecular fragments was found to be a dominant mechanism for molecular clusters such as water cluster cations $(H_2O)_nH^+$ [240], methanol cluster cations $(CH_3OH)_nH^+$ [241] and $(NH_3)_nNH_4^+$ [242, 243]. Compared to these clusters with relatively weak intermolecular bonds, shattering of C_{60}^+ requires much higher energies [244, 245]. It was shown by Kappes and co-workers in collision experiments on different surfaces that the fullerene energy must be as high as ca. 300 eV [246, 247]. The experimental results are consistent with maximum entropy calculations that predict shattering for internal energies beyond ca. 200 eV [244]. However, a lower shattering threshold of 150 eV for C_{60}^- impacting on a gold surface was reported by Kaplan et al. [248]. Kaplan et al. also

studied the small scattered fragments C_n^- (n=2-12) and suggested two multifragmentation modes: a post-collision event at near-grazing incidence with a common average velocity for all fragments and direct collision-induced dissociation at near-normal incidence with a common average energy for all fragments [249].

Thus, the scattering experiments demonstrate that at very low collision energies the cluster can rebound without dissociation. With an increase of E_{kin}, rapid heating of the cluster on impact with the surface leads to evaporation of atoms or small fragments. At higher energies shattering or fission of the cluster occurs. It is worth noting that for the relevant interval of E_{kin} cluster scattering processes may not be the dominant channels. In many cases colliding clusters remain on the surface and become embedded (see section 3.3).

Impact chemistry is one more interesting case of the use of energetic cluster beams [35, 250]. Molecular clusters impacting on a solid surface with hypersonic velocities (which are roughly an equivalent of E_{at} between several and several tens of eV) could be one suitable approach to explore chemical and physical processes at extraordinarily high pressures and temperatures on a nanometre scale [251]. As the front atoms of the cluster reach the surface and abruptly slow down, the rest of the cluster is still moving forward. Therefore, immediately after the beginning of impact, E_{kin} is converted into internal energy. Computational studies, for instance, by Landmann and co-workers have revealed that the effective temperature and pressure can reach 4000 K and 10 GPa, respectively, on impact of Ar_{561} on NaCl with an E_{at} of only ca. 1.9 eV [252]. Raz and Levine showed that an initially cold Ar_{125} cluster colliding with the surface at a velocity of 10 km/s ($E_{at} \approx 21$ eV) can be heated to well over 10^5 K [250]. This shock phenomenon occurs on a time scale below 1 ps. However, this short period is long enough for chemical reactions to take place. Moreover, clusters can be regarded as a perfectly defined reaction system with a freely adjustable composition of the reactants. From a chemical point of view, the energy range from 0.1 to about 10 eV/molecule is especially interesting, as it allows fragmentation of the cluster, dissociation of the molecules within the cluster, and formation of new chemical bonds without destroying the solid substrate. Thus, not only dissociation of chemical bonds can occur within a cluster compressed by the impact

on a solid surface but also bond formation is possible in the very short time between cluster impact and subsequent fragmentation [36, 35]. In particular, the formation of molecular iodine was detected on surface impact of small $(CH_3I)_n^-$ clusters with a reactive reaction yield of 15 % (see Fig. 24). The variation in E_{kin} then allows a change in the rate of excitation of cluster vibrations, the total internal energy content and the particle density.

3.3. Cluster pinning

An increase of E_{at} above E_{coh} leads to significant plastic deformation and partial fragmentation of the cluster as already discussed in the previous section. However, if E_{at} only slightly overcomes E_{coh} and the cluster is not very small the escape of several atoms changes the cluster composition insignificantly. At the same time, the energy transferred to the substrate atoms upon collision can already be high enough to displace one or even a few of them. Thus, some point defects are formed and the residual cluster becomes trapped at these sites. Such an energy regime is called pinning [253, 254]. It is a boundary case between the soft landing and implantation of clusters. Pinning suppresses the cluster surface diffusion which can be advantageous for a number of practical applications. It is worth noting that in the soft-landing regime clusters can be immobilized on the surface defects or F_s-centres [255], thus, their diffusion is also suppressed but these are not the cases discussed in the current section.

Pinning of clusters was mostly studied on graphite, a material chosen due to its atomically smooth surface that favors observation of the deposited clusters, especially very small ones. A number of different cluster species have been investigated (for instance, Ag_n, Au_n, Pd_n, Ni_n and Co_n) [253, 254, 256, 257, 258, 259]. Good agreement with experiments was achieved using MD simulations [254, 259, 260]. In particular, it was shown that the energy required to displace carbon atoms was between 4.75 and 6.25 eV irrespective of cluster size in the range n = 7-100 [260, 261]. These values are close to the vacancy or interstitial formation energies in graphite which were reported to be between 5.5-7.0 eV [262]. Both experiments and simulations demonstrated a certain threshold (minimum) energy

value E_{pin} required for the cluster pinning. E_{pin} was found to be dependent on cluster species, size and substrate composition. A semi-empirical model gave the following relationship between E_{pin} and the transferred energy E_T required to displace a target atom (or produce a recoil one) [260]

$$E_{pin} = \frac{nmE_T}{4NM},$$

(4)

where n is the number of atoms in the cluster, m is the atomic mass of the cluster constituents, M is the mass of the target atoms and N is the number of recoil atoms. To obtain pinning of small clusters, one can assume that only one carbon atom should be set into motion and this approach agreed rather well with the experiments, showing a linear dependence of E_{pin} on cluster size. In other words, the pinning energy per cluster constituent was found to be a constant value (Fig. 25). These values vary between ca. 6 and 16-19 eV/atom from Ni to Au [253, 256, 257, 258, 259, 260]. The shape and structure of the pinned clusters were found to be dependent on their size and to a great extent on the type of species. For instance, it was shown by MD simulations that large gold clusters are more spread out after the impact and can partially fragment while pinned nickel clusters are more compact (Fig. 26) [261]. For the case of cobalt clusters, both modeling and experiments demonstrated that they prefer to form single adatom layers on interaction with graphite if the cluster sizes are of a few tens of atoms [259].

Studies of metal clusters with n $\gtrsim$ 80-100 atoms have shown that the dependence of E_{pin} on n changes to sublinear as n increases [257, 260]. With an increase in size, the cluster becomes more efficient at damage formation: many target atoms can be displaced from their sites on individual impact under conditions where the large cluster has the same E_{at} as the small one. However, to trap the large cluster only a few defects are needed. Thus, lower kinetic energy per atom is required to pin the larger clusters.

It is worth noting that the obtained pinning threshold energies for metal clusters impacting on graphite are close to those for the formation of thin adhesive metal films by energetic cluster deposition [24]. In both cases, the clusters produce some radiation damage

at the surface and are able to penetrate beneath the surface. The energies (of several eV/atom) that were sufficient for these processes are significantly lower than those known for monomer ions. For example, the minimum value required by light He^+ ions to penetrate through a graphite surface was found to be 22.5 eV [263]. It is also known that the penetration threshold increases with atomic radius reaching several tens of eV for heavy ions. One more example is large (thousands of atoms) Ar_n impacting on Si. In this case the threshold energy was estimated to be only about 4.7 eV per atomic constituent while for argon monomers it is ca. 15-20 eV [264]. This is one of the clear cases where the physics of cluster impact is different from that of monomer ion impact. The reason for the difference is in the high energy density deposited by the cluster. Despite the quite low energy per atom, multiplication of this relatively low energy by the number of atoms and division by the very small surface collision area leads to high values of the energy density.

Cluster pinning is not of only fundamental interest. The pinned clusters can have a number of potential applications. One of them is immobilization of protein molecules for their further investigation or fabrication of biochips [12, 265]. Pinned metal clusters can also be considered as a main component of nanoscale gas sensors. Adsorption of gas molecules on the cluster surface can significantly change its electronic properties [266]. These changes can be monitored either by optical methods (plasmon resonance) or through measurements of the conductance of the cluster ensembles. Pinning of size-selected metal clusters is also of significant interest for catalytic applications, as was already mentioned in section 3.1.3.

3.4. Surface erosion on cluster impact

3.4.1. Crater and hillock formation

It is well known that the elastic collision of an accelerated ion with lattice atoms leads to a knock-on effect and the formation of a displacement cascade. Under certain conditions, the lattice atoms have a high probability to be sputtered from the surface [267]. It was experimentally observed that the impact of heavy ions can lead to crater formation. For instance, craters with diameters in the range of 4-5 nm were found on a Au surface

implanted by Bi^+ and Bi^{2+} ions [268]. More systematic study of this phenomenon showed that the crater diameter depends on the implantation energy. For the case of Kr^+, As^+ and Ge^+ ions implanted into PbS and Si, the crater diameter was found to increase from 7 to 28 nm when the energy was increased from 20 to 200 keV [269]. However, with further energy increase up to 500 keV the crater diameter and the ratio of craters per impact decreased: craters were not found for an energy of 1 MeV. To explain crater formation on energetic ion impact, the modified thermal-spike model, introduced by Seitz and Koehler [270] and further developed by Kelly and Miotello [271, 272] is widely used: the phenomenon is associated with individual displacement cascades originated by the projectiles. Wilson et al. suggested that the centre of the displacement cascade is rich in vacancies and the periphery in interstitials [269]. This causes stress leading to compaction or sinking of the central part and peripheral rising forming the crater rims.

Craters are also often found in energetic cluster-surface collisions both in experiments [273, 274, 275, 276, 277, 278] and in MD simulations [88, 89, 279, 280, 281, 282, 283, 284]. Some examples of experimental observations and simulations are presented in Fig. 27 and 28. The physics of cluster-surface impact is different from that of monatomic projectile impact due to the multiple collision effect, i.e. the interaction of numerous cluster constituents with the target atoms on a very short time scale (typically the initial stage of impact lasts less than 1 ps). Such an interaction leads to local high-energy transfer and strong disorder of the atomic arrangement in the impact region. The target atoms in the core part of the impact area contribute to the development of inward displacement cascades forming a depression on the surface, i.e. a crater. A large fraction of atoms – those present at the periphery of the impact area – gain lateral momenta or momenta directed away from the surface (Fig. 29) [88, 285]. Thus, they either form an atomistic flow that contributes to the formation of the crater rim or they become sputtered.

The conditions under which an incident cluster causes crater formation are mainly dominated by the kinetic energy per cluster constituent rather than the total cluster kinetic energy. However, it is important to remember that cluster impact is a multiple-particle

phenomenon and the energy density locally transferred to the target atoms must be considered.

The efficiency of crater formation is also dependent on the properties of the substrate material. Higher material density, melting point and larger atomic displacement energies provide less favorable conditions for crater formation as shown by comparison of keV-energy argon cluster impact on silicon and sapphire [286]. Recent experiments on Ar_n^+ implantation into diamond have supported this conclusion [287]. It was also suggested that the crater shape can be dependent on the crystallographic structure of the target. For example, Insepov et. al found the craters to be near conical with the facet directed along the (111) plane for Si(100) and hemispherical for Si(111) (Fig. 30) [288]. For some substrates the crater formation is suppressed due to material properties. For instance, implantation of Ar_n^+ and Co_n^+ ($16 \leq n \leq 63$) cluster ions into graphite with E_{at} up to 1 keV led to no crater formation [259, 289]. The explanation was obtained with the aid of MD simulations, demonstrating that craters can appear only at the initial stage of impact. The elastic behavior of graphene sheets at a later stage causes efficient closure of the craters and only disordered areas are finally formed [287]. Such areas were experimentally observed as sub-nm high bumps using STM.

The crater diameter typically increases with the cluster size. This was shown experimentally by the example of keV-energy Ar_n: with an increase in size from a few hundred up to a few thousand atoms the crater diameters on Si and Au surfaces were increased from 4 to 35 nm [275, 290, 291]. MD simulations demonstrated that the crater volume increases nonlinearly with the cluster size [292]. The dependence of crater size on E_{kin} has a more complicated behavior. On the one hand, the increase of energy leads to more efficient excavation of the substrate material in the impact area, thus, to the increase of crater sizes. For instance, it was shown for the case of large Ar_{2000} impacting on silicon that the crater diameter is roughly a function of $E_{at}^{1/3}$ (see Fig. 31) [293]. On the other hand, at higher kinetic energies the cluster constituents become implanted and the maximum of the energy transfer shifts deeper into the bulk, thus, eliminating the efficiency of sputtering.

Therefore, after a certain energy threshold, the crater formation rate starts decreasing [294] and crater diameters can become smaller. The latter tendency was, for example, found for the implantation of small Ar_n^+ into silicon: the craters shrank at higher impact energies [286].

The craters produced by atomic clusters resemble macroscopic ones formed, for example, on meteorite impact. However, the crater formation processes are different on the nanoscale and macroscale. As mentioned above, the nanoscale craters originate from atomic displacements at the surface. Their formation is well understood in the framework of thermal spikes, development of shock waves and liquid flow phenomena. Macroscopic crater formation is better understood in terms of a transient high-pressure region inside the material: both compression of the impacting body and successive compression and expansion mechanisms in the target are considered [295, 296]. The crater volume V typically scales linearly with the impact mass according to the following empirical equation [295]

$$V = K \frac{m}{\rho} \left(\frac{\rho v^2}{G} \right)^{3\mu/2},$$

(5)

where v and m are the impactor velocity and mass, respectively, ρ and G are the density and strength of the target material, respectively, K is a target parameter dependent on the mass density and strength and μ is the scaling exponent which varies between 1/3 and 2/3. However, it was recently demonstrated using large-scale atomic simulations that the crater formation in the case of very large (containing many thousands of atoms) clusters emerges the macroscopic cratering behavior [297, 298]. Nowadays, due to the significantly increased power of computers, one can afford to model systems consisting of millions of atoms and apply atomic simulations as a tool for the understanding of phenomena that arise on impact of macroscopic objects.

Besides craters, another type of surface nanostructure - hillocks (nm-size protrusions) - are often observed under implantation (Fig. 32). For the case of conventional ion implantation the reported energies required for hillock formation are on the level of MeV. However, for the case of clusters the hillocks are already observed on impacts with E_{kin} of

several keV (in most cases these values correspond to just a few hundred eV per atom). In order to understand the mechanisms of hillock formation on cluster impact we will give a short introduction to this topic for the case of high-energy ions.

There are numerous reports on hillock formation under MeV-to-GeV-energy ion implantations. See for example [299, 300, 301, 302]. Hillock sizes vary depending on the implantation species, energy and target material. Typically, they are from a few up to ca. 10 nm in height with basal diameters of about 10-40 nm. Several models were developed and applied in order to explain the hillock formation [41, 302, 303, 304, 305]. Some mechanisms are still debated. However, the most commonly-accepted scenario is the following. The hillock formation is caused by energy transfer from the high-energy ion to the target due to electronic stopping that leads to melting along the latent track with subsequent pushing out and quenching of the molten material. For MeV ion implantation the hillocks are formed only if the electronic stopping power is above a certain threshold corresponding to the condition that the transferred energy is enough to surpass the melting point along the entire track [306, 307]. In other words, the implantation should provide formation of continuous amorphous tracks. For discontinuous tracks, the flow of molten material towards the surface is hindered and the formation of hillocks is obviously suppressed [308].

Hillocks are often found on impact of keV-energy clusters, a few orders of magnitude lower in energy compared to the cases of ion implantation, discussed above [275, 309, 310, 311, 312]. In most cases, the hillocks were reported to be cone-shaped (or truncated cone-shaped). Sometimes, dimples were found at the top of the hillocks [275]. Typically, the height varies on the scale of a few nm and the basal diameter is between 10-50 nm [275, 286, 310]. In some reports [310, 312], larger diameters were measured using AFM but they were most probably related to the tip convolution effect. Thus, the hillock dimensions on cluster ion impact are very similar to those reported for high-energy ion implantation.

The mechanism of hillock formation can be ascribed to the result of nuclear stopping of the cluster constituents in a shallow layer of the target. On keV-energy cluster impact, MD simulations show an exreme compression of the material (up to GPa level) and a local

increase of temperature up to a few thousand degrees [88, 252, 275]. As soon as this temperature increases above the melting point the material melts around the impact spot. The molten material can be pushed out and quenched, forming a hillock [29, 286]. The melting model is supported by the experimental observations. By comparing cluster ion implantation into silicon and sapphire, it was shown that a threshold energy is required for the formation of hillocks [286]. No hillocks but only simple craters were observed until this threshold value was reached. For the same cluster size and kinetic energy the threshold was found to be lower for the material with lower melting point and smaller atomic displacement energy. An increase of kinetic energy led to growth of higher hillocks. After reaching a maximum value, the hillocks then gradually decreased in size until they were almost invisible. This phenomenon was explained by the inward shift of the cluster-to-target energy transfer and melting of the material at greater depth that made the push-out (or expulsion) effect less prominent. The origins of the expulsion effect are not completely understood yet but they can be related to the difference in density of the hot fluidised material and the surrounding solid state matrix that leads to significant local tensions. One more possible mechanism is elastic rebound of the bulk as a result of relaxation after shock wave formation.

In a few experiments on keV-energy cluster ion implantation [286, 278] it was found that a hillock can be located in the centre of the crater (i.e. surrounded by a rim) forming a complex crater (Fig. 33). The name was chosen by analogy with the similarly shaped craters made by meteorite impact on planet surfaces [296]. The first suggested model of complex crater formation assumed that the crater is formed due to the excavation of the material while the hillock originates according to the mechanisms discussed above [278]. Some MD simulations were able to predict the formation of a small peak at the crater bottom, for example for the case of $(CO_2)_n$ collisions on diamond [313]. However, such MD simulations showed a much smaller rim-to-rim diameter for the complex craters compared to those observed in the experiments (up to 50 nm even on impact of rather small clusters with sizes of only about 1-2 nm and E_{kin} of a few keV) [286, 314]. These large rim-to-rim diameters could not be explained just by excavation of the target material on cluster impact. This

discrepancy led to the inference that there is an effect which is not properly presented in the classical MD modeling. Recent MD simulations of Ar_n cluster implantation in silicon predicted a significant increase of lateral momenta of target atoms around the impact spot [314]. The simulations also showed the possibility of collective oscillations of the target atoms involved in the collision event (see Fig. 34) [315]. These oscillations could last a few ps. This phenomenon is especially pronounced if a thin layer is present on top of the bulk target and if the collision cascade is developed at the interface of these two materials, for example in Si covered by a native oxide layer [314]. Thus, one can suggest that surface waves are formed in the small local volume melted by energy transfer on the cluster impact with subsequent quenching of the waves forming large rims. However, this model requires further investigations.

3.4.2. Sputtering and smoothing

Bombardment of a sample by energetic particles can lead to sputtering of atoms and surface erosion as was already shown for the case of individual impacts causing crater formation. In this section, more general aspects of sputtering by cluster ions are discussed. The erosion efficiency is characterised by the sputtering yield Y, which is defined as the mean number of emitted atoms per incident particle. For the case of monatomic projectiles, the sputtering occurs as a result of the collision cascade development: some of the recoils approach the surface with enough energy to escape [267]. Depending on ion species, energy and target material, Y typically varies between 0.5 and ca. 10. An exception was shown for bombardment of C_{60} films. For 170 keV Bi^+ and 800 keV N^{2+} ions, Y of over 10^4 atoms was reported [316]. Such extremely high sputtering yields were explained by collision-induced decomposition of the fullerenes.

A high sputtering yield was theoretically predicted and experimentally observed on bombardment by cluster ions [273, 317, 318, 319, 320, 321]. For impacting clusters, Y was found to be from several tens to several thousands of atoms per cluster ion [322, 323, 324]. With clusters, the linear cascade sputtering theory fails to a large extent. Instead, non-linear

effects prevail, accompanied by thermal spikes. Very high sputtering yields can be explained in terms of the multiple-collision effect leading to the local deposition of high energy that causes the formation of many collision cascades. For a single collision, a significant fraction of the target atoms at the periphery of the impact area obtains momenta directed away from the surface. For a beam of clusters, this effect leads to very pronounced lateral sputtering shown in Fig. 35 [28]. The obtained distribution is rather different from the case of sputtering by monomers described by the "cosine" law $Y(\Theta) \sim cos^m \Theta$ with $m \geq 1$, where Θ is the emission angle of the sputtered atoms.

For cluster sputtering, a relation $Y \sim E^{1.4}$ was predicted by MD simulations [325]. This law demonstrated reasonable agreement with experimental results on Ar_n^+ sputtering of various metal surfaces [322]. Studies of sputtering of gold and silver targets by small gold clusters showed that for the energy interval from 20 to ca. 200-300 eV/atom $Y \sim (dE/dx)_{nucl}^2$, where $(dE/dx)_{nucl}$ is the nuclear stopping power. However, after reaching a maximum Y starts decreasing with a further increase of energy [324]. One of the explanations of this phenomenon is the transition to a constant nuclear stopping power for projectiles with velocities above a certain value.

One more important parameter for sputtering is the cluster size. In the experiments on Si sputtering by keV Au_n, it was found that Y slightly increases with cluster size [321]. More recent studies of argon cluster impact on Si and Au targets have shown quite similar results, in particular, that the sputtering yield is proportional to the size (number of atoms) to the power 1.1 [264]. The experiments on energetic impact of small (up to 13 atoms) Au_n on gold and silver targets demonstrated an interesting effect that Y/n^2 increases linearly with E_{kin} until a maximum is reached [324]. This effect found its theoretical background in the work of Samela and Nordlund [326]. They also suggested a model for the above-mentioned dependence $Y \sim (dE/dx)_{nucl}^2$. The model showed that the sputtering yield can not be directly proportional to the cluster energy because most of the energy deposited in head-to-head collisions does not contribute to the displacement cascade formation. Instead, the effective damage energy deposited from the cluster must be considered.

The high sputtering yield provided by keV-energy clusters is an important effect for surface smoothing [327, 328, 329]. A "downhill particle current" model was developed explaining suppression of the surface roughness under cluster bombardment by re-deposition of material from hills (protrusions) into valleys (pits) due to the above-mentioned domination of lateral sputtering (Fig. 36) [318, 330]. Effective cluster-induced smoothing can also be explained in the framework of the Bradley-Harper theory [331]. Formation of surface relief on particle bombardment can be described by two competing mechanisms: the change of the sputtering yield with the incident angle of the impactor and surface migration or re-deposition of atoms. For cluster bombardment, both the angular distribution of sputtered atoms and the sputtering yield are strongly dependent on the incident angles [274, 332]. Hence, even at normal incidence of the cluster beam there are always local variations of the impact angle for individual clusters due to the small changes in topography on the nanoscale. These variations change the local sputtering rate. In particular, an increase of incidence angle α leads to a decrease of Y, following $Y(\alpha) \sim cos\alpha$ [332]. The tops of small hills are sputtered more efficiently than slopes. High energy transferred to the sputtered atoms leads to their enhanced surface mobility, thus, facilitating filling of the valleys between the hills.

The phenomenon of surface smoothing by cluster beams was found to be of considerable interest for industry, in particular for electronics and optics. For practical applications, the cluster energy should be high enough to provide displacements of the target atoms but not too high to avoid implantation and severe radiation damage of the substrate. A commercially available technique utilizing gas cluster ion beams has been developed [333]. The main advantages of this technique compared to ion or plasma assisted processing are high spatial resolution, short-range damage and elimination of charge accumulation on the substrate surface. In combination with conventional evaporation techniques energetic cluster beams were demonstrated to be an efficient approach to improve uniformity of the deposited thin films and to produce flat interfaces in multi-layered structures [334]. One more advantage is a high smoothing efficiency at oblique angles (~ 85° incident angles) that makes cluster beams an exclusive tool for smoothing and polishing of side walls of various

trenches or vertical pillars (Fig. 37) on the micron or submicron scale [34, 335]. It is important that cluster smoothing does not have a negative effect on the surface mechanical properties. For instance, a TiN surface smoothed by an Ar_n^+ cluster ion beam did not exhibit any change in its mechanical properties, e.g. nanohardness or residual stress [320].

Cluster sputtering also attracted a lot of attention for use in SIMS. Different cluster species were tried. By selecting the best-suited primary cluster ions the sputtering ion yield can be increased significantly. Cluster beams are especially important for the analysis of organic targets where there is a need to limit the penetration depth and large clusters are favored. For more details on this topic we refer to a recent review [336].

3.4.3. Reactive cluster erosion

In addition to the physical sputtering discussed above, "chemical sputtering" or reactive accelerated cluster erosion (RACE) was found [337]. In impact experiments of 120 keV $(CO_2)_n^+$ on diamond and copper substrates, the experimentally measured rates were of the same order of magnitude for both materials, despite the predicted much higher erosion rate (about 2 orders of magnitude) of copper compared to diamond. It was assumed that the very high temperatures reached on the hypervelocity cluster impact led to the dissociation of the CO_2 molecules and the resulting atomic oxygen reacted with the target material. In the case of copper a low-vapor-pressure oxide was formed while for the diamond a highly volatile CO compound was the resulting product. The chemical sputtering mechanism was later confirmed in experiments with $(SF_6)_n^+$ bombarding W, Au, Si and SiC [273]. For example, in the case of 20 keV cluster ions comprised of 2000 SF_6 molecules, each molecular constituent has an energy of 10 eV that gives about 1.43 eV/atom. This value is much lower than the average displacement energy of Si atoms (about 15 eV) as well as lower compared to the energy threshold found for physical sputtering of Si in the case of Ar_n^+ cluster ions (4.7 eV) [264]. However, the sputtering yield of Si by $(SF_6)_{2000}^+$ was found to be 55 times higher than by Ar_{3000}^+. The high yield of volatile SF_x compounds was registered by a residual gas analyser confirming the chemical nature of the sputtering. The effect of lateral sputtering for

the "chemical case" is eliminated which is caused by the isotropic evaporation of volatile materials produced by the chemical reactions. It was shown that the smoothing effect for chemical sputtering is poorer than for the physical sputtering induced by inert gas clusters [328]. However, chemical sputtering can find another application, for instance, selective etching. RACE was suggested as a cluster impact lithography method for obtaining specific surface micron or submicron reliefs by making use of mask-protected patterning [28]. Thus, by taking into account the much higher sputtering efficiency of $(SF_6)_n$, $(CO_2)_n$ or $(O_2)_n$ compared to inert gas clusters the former can be proposed for high-speed processing of surfaces. However, a more systematic study of chemical sputtering by cluster ions is required.

3.5.   Implantation of clusters

Consider a cluster impacting a solid with a relatively high velocity (where E_{at} is much higher than E_{coh}). The cluster will be rapidly broken down, after some tens or hundreds of femtoseconds, [338, 339] and such interaction must be treated as a multiple-collision event. At the beginning of the impact, energy and momentum transferred very locally to the target cause its compression and an increase of temperature. Local temperature and pressure can rise by up to 10^4-10^5 K and the GPa level, respectively, for the first 10^{-13}-10^{-12} s [88, 252, 275]. The impact causes a shock wave to propagate from the surface towards the bulk [281, 340]. Interaction of the energetic cluster constituents with the target atoms also leads to the development of thermal spikes. In the case of keV-energy cluster implantation the thermal spikes originate via nuclear stopping of the projectiles, i.e. by energy deposited in ion-atom and atom-atom collisions during the ballistic (or dynamic) phase of the collision cascades [271, 272]. These cascades have a complex nature due to non-linear effects related to the interaction of cluster constituents not only with the target atoms but also with each other. High local temperatures can cause melting of the material around the cascades [92]. Nowadays, there is no commonly accepted theory that satisfactorily describes the cluster

implantation process. Therefore, the goal of the following sections is a critical analysis of the published data on the subject.

3.5.1. Stopping of clusters in matter

We start from consideration of the keV-energy implantation regime, i.e. with E_{at} ranging from tens of eV to a few keV. The energy loss occurs predominantly via elastic collisions between the atoms (nuclear stopping). However, due to the nearness of the penetrating cluster constituents, one can expect an interaction between them that complicates the analysis of the stopping process. It can not be explained in terms of binary collisions as in the case of monatomic projectiles. Closely penetrating cluster constituents lead to the development of overlapping displacement cascades [341]. Thus, the difference between the stopping of an atom in a cluster and an individual atom makes a difference to the projected range R_p (mean implantation depth) of cluster constituents and hence to the produced radiation damage compared to monomer ion implantation.

3.5.1.1. Projected ranges and stopping power

MD and Monte Carlo simulations showed that the penetration depth of cluster constituents is larger than for monatomic ions of the same chemical element at the same incident velocity [342, 343, 344]. This phenomenon was called "clearing-the-way" and was explained by considering that the "front" atoms of the cluster push target atoms out of the way of the "rest" atoms. As a result of this the stopping power of the cluster is reduced and the projected ranges of most of the cluster constituents are increased. Heavier ions would thus be expected to cause more clearing of "light" targets [345]. On the contrary, the effect is negligible if the mass of the cluster constituents is much smaller than the mass of the target atoms, as was shown, for instance, for simulations of deuterium cluster implantation (clusters of up to 500 atoms with energies of 200 eV/atom) into a silver target [345].

"Clearing-the-way" was demonstrated in a number of publications (see below). However, different simulations and experiments showed various scaling laws for cluster implantation.

MD simulations of small clusters, for instance Ar_6 and Ar_{13} implanted into Si, showed an almost linear scaling of R_p with the implantation energy, i.e. a very similar dependence as seen for the monomer ions [285]. In the case of larger argon clusters with n = 43 and 688 and E_{at} between 10 and 100 eV it was calculated that $R_p \sim E_{kin}^{1/3}$ with the penetration depth largely independent of n (Fig. 38) [285]. Modeling of Au_n (n = 2-7) implantation into Cu with E_{at} = 1-10 keV showed a slight increase of R_p with n for the same E_{at} [338]. A similar effect was found for B_n (n = 10, 18 and 36) implanted into silicon with a constant E_{at} = 200 eV [346]. This modeling also demonstrated that the mean depth of both boron atoms and the defects (Si interstitials) increase with cluster size as $n^{1/3}$. Calculations of implantation of Si_n (n ≤ 50) into Si with a constant E_{at} = 70 eV demonstrated the same dependence $R_p \sim n^{1/3}$ [347]. However, for this case, the dependence of R_p on the energy gave a scaling $\sim E_{at}^{1/2}$. Simulations of Au_n (n = 1, 13, 43, 87, 201, 402) implantation into gold and graphite with E_{at} = 100 eV showed a clear effect of the cluster size on the projected ranges and the dependence followed a power law $R_p = an^{\alpha}$ with α varying from 0.31 to 0.45, when changing from gold to graphite [348]. The value of α obtained for the gold target is in agreement with the value for the implantation of Si_n clusters into Si. The difference in α for the gold clusters implanted into graphite could be explained in terms of more "clearing" for targets composed of "light" atoms and by the layered structure of graphite.

Thermal spikes were also found to be important for the penetration of cluster constituents and development of the displacement cascades. The calculated effective radius of the molten regions, for example, in Cu was about 2 nm per cascade [349]. MD simulations showed an increase (up to 130 %) in the straggling of the projected range ΔR_p of Au_n implanted into Cu with E_{at} = 1-10 keV compared to monomers due to atomic mixing in the thermal spike [338]. However, this theory predicts that no increase in ΔR_p of cluster constituents is expected for Si because the cascades break down into subcascades at much lower energies compared to Cu. The resulting liquid-like pockets are much smaller in silicon and cool down faster. Similar to this simulation, there was no difference in R_p and a very small difference in ΔR_p found when comparing the calculated values for B_1 and B_{10} implanted

into Si with E_{at} of 200 and 500 eV/atom [350]. The theoretically predicted change in R_p and ΔR_p was found to be in good correlation with the experimentally obtained depth profiles of Au_n^+ (n = 2, 3, 7) implanted into copper and silicon with E_{at} = 10-100 keV [351].

However, compared to simulations, there is rather little experimental data on measurements of R_p for cluster implantation. The "clearing-the-way" was experimentally found in the case of small Ta_n^+ (n = 2, 4, 9) implanted into graphite with E_{at} = 555 eV, however no scaling dependence was suggested [352]. Experiments on the implantation of B_n (up to n = 4) into silicon showed an increase in both R_p and ΔR_p in the case of small clusters compared to monomers by about 20 and 30 %, respectively [353]. There is an interesting series of experiments carried out on cluster ion implantation of graphite. Graphite is chosen because it has an atomically smooth surface that makes it easy to resolve very small radiation damaged areas. One more advantage is that post-implantation thermal treatment gives a possibility to extract the depth of the introduced radiation damage [354, 355] which corresponds well to the depth of the deepest implanted constituents in the case of the keV-energy implantation regime. It was found using MD simulations that the secondary (recoil) displacement cascades give only a minor contribution to the damage and can be disregarded [289]. For C_{60}^+ ion implantation into graphite with a rather wide range of energies from 500 eV to 23 keV the penetration depth was found to follow $E_{kin}^{1/2}$ [280]. The same type of dependence was demonstrated for the case of graphite bombarded by keV-energy Ag_7, Au_7 and Si_7 [356]. Since cluster momentum $p \sim E_{kin}^{1/2}$, it was suggested to scale implantation depth (or R_p) not with energy but with momentum, giving a linear scaling law presented in Fig. 39 and following the dependence

$$R_p = a + bp = a + bmv, \tag{6}$$

where m and v are the cluster mass and velocity, respectively, a and b are the fit parameters. This equation can also be represented as

$$R_p = a_n + b_n v \tag{7}$$

where a_n and b_n are the size(mass)-dependent parameters [357].

In the general case of implantation, one of the important parameters defining the projected range (as well as radiation damage) is the stopping power. For the case of clusters with keV-energies the dominant mechanism is nuclear stopping. To find $(dE/dx)_{nucl}$ we consider that E is the kinetic energy equal to $mv^2/2$ and x represents R_p. Then by substituting v in eq. (6) we get

$$\left(\frac{dE}{dx}\right)_{nucl} = \frac{mv}{b_n} = \frac{p}{b_n} \tag{8}$$

Thus, both the projected range and nuclear stopping power are linear functions of the cluster momentum.

However, as one can see in Fig. 39, the best fit straight lines are different for different cluster species, inferring that there is some implantation parameter which is not considered. Such a parameter was suggested by Harbich and co-workers [357]. They divided the cluster momentum by the cross-sectional area of the cluster, thus, introducing the scaled momentum. A similar approach was used in [259, 289] where systematic studies of Co_n and Ar_n impacting on graphite with E_{at} between 1-1000 eV were carried out. It was demonstrated that the experimentally found values of the implantation depth for several cluster species and different cluster sizes fall on the same straight line when plotted versus scaled cluster momentum (momentum divided by projected surface area), as shown in Fig. 40(a). MD simulations for the same cluster species, sizes and energies demonstrated good agreement with the experiments (Fig. 40(b)). Thus, by considering the momentum it was possible to include both the implantation energy and mass of the cluster into the development of cluster stopping theory. However even for identical sizes, the diversity of chemical and geometrical structures may lead to different stopping. The difference in cluster cohesive energies affects the implantation only a little because clusters become broken on a very short time scale at

the beginning of the collision. The geometrical structure and cluster diameter are of higher importance because they define the area of the cluster-surface interaction. Thus, these parameters were taken into account to first order by introducing the scaled momentum. Hence, the universality of a simple empirical scaling law for cluster implantation into graphite was proposed. This can be an important contribution to the development of a general theory of cluster stopping in matter.

3.5.1.2. Radiation damage

Radiation damage under cluster implantation is a closely-related problem to cluster stopping. Unfortunately, this question has not been extensively studied experimentally so far. MD simulations of Ar_n impacting on Si showed that a similar damage region is formed by both large (hundreds of atoms) and small (tens of atoms) clusters if the total E_{kin} is the same (Fig. 41) [285]. In other words, an increase in cluster size leads to a decrease in the threshold energy of damage formation and to an increase of the displacement yield [358]. The latter is confirmed by other calculations. Simulations of Ta_n implantation into graphite evidenced a superlinear increase in the number of defects (vacancies) with cluster size at the same E_{at} [359]. In simulations of B_4 and B_{10} clusters implanted into Si with $E_{at} = 230$ eV it was found that the clusters produced a several times larger number of Frenkel defects (vacancies and interstitials) and gave a higher yield of amorphisation compared to B monomers [360]. Experiments on boron dimers and trimers implanted into Si with $E_{at} = 1$ keV qualitatively confirmed the simulations by demonstrating that the number of displaced silicon atoms per cluster atom increased by a factor of two compared to the monomer implantation [361]. A similar effect was found in experiments that compared radiation damage formation under the implantation of P^+ and F^+ atomic ions with PF_n^+ cluster ions having the same energy of 2.1 keV/amu [362]. The increased defect concentration for the cluster case was assigned to a molecular effect resulting from both a spatial overlap of collision subcascades and clustering of point defects.

Overlapping of the thermal spikes produced by individual cluster constituents leads to a strongly enhanced mixing of atoms [338] causing an increased ΔR_p [351] and, as a result, higher damage. For energies of several keV per cluster (the case of very shallow implantation), the depth of radiation damage is typically close to the projected ranges of the cluster constituents: the role of secondary displacement cascades is found to be minor as shown by MD simulations of boron cluster implantation into silicon (Fig. 42) [346]. This was also found to be the case in experiments on the keV-energy implantation of Co_n^+ in HOPG [259]. The graphite target is layered with strong covalent bonds in the plane and weak (van der Waals) ones between the planes. Therefore, the graphite structure responds very elastically to cluster impact: the collisions induce oscillations of the graphene planes [283]. The oscillations have very little influence on the structure outside the immediate impact region with primary displacement cascades, although their amplitude could be as large as the distance between two neighboring planes and the oscillations last a few tens of ps. The fragmented cluster atoms that have gained lateral momenta in the first collisions can travel away from the "impact core" between graphene layers, and therefore do not produce defects.

3.5.2. Shallow doping

Despite the lack of full understanding of cluster stopping, there is a practical interest in shallow implantation of clusters, for instance, for the formation of thin insulating layers. Implantation of chemically reactive cluster ions of $(O_2)_n^+$ and $(CO_2)_n^+$ into silicon with energies of 5-10 keV showed the formation of high quality SiO_2 films of a few nm thickness that can be adaptable for fabrication of ultrathin insulating layers for semiconductor devices [363]. An advantage of the cluster method is the very low surface roughness (below 0.5 nm) of the film [222] compared to so-called passive oxidation (SiO_2 formation under high oxygen pressure and high temperature) [364]. Synthesis of such thin SiO_2 films by other methods, for example, by pulsed laser deposition or plasma-enhanced chemical vapor deposition (PECVD), was found to be impossible due to either bubble formation (laser) or high porosity (PECVD) resulting in poorer quality and higher roughness of the films [365, 366].

Present-day semiconductor technology uses lower and lower implantation energies and heavier implant species because the new generation of transistors already needs to have *p-n* junctions of ca. 10 nm thickness. It was shown that low-energy implantation of $B_{10}H_{14}$ clusters can be an efficient way of doping shallow silicon layers [317]. The most important phenomenon found was the suppression of enhanced boron diffusion in cluster-implanted silicon during post-implantation thermal annealing. The physical nature of the effect is not fully understood. Most probably it is related to short transient thermal and pressure spikes in the very shallow layer leading to an intense intermixture of the implanted species with the target atoms and complete restructuring of this layer. A transistor with a 40 nm effective gate length was fabricated by such cluster implantation already in the middle of the 90's (Fig. 43). The possibility of forming ultrashallow junctions was also shown by using $(SiB_n)^-$ and $(GeB)^-$ cluster ions [367]. Ultra-shallow junctions of < 6 nm by B in-fusion into Si were fabricated and Ge in-fusion for the formation of thin layers of strained Si was proved using the cluster technique [39]. However, it took more than a decade to develop the cluster beam method suggested in the middle of the 90's into an industrial technology with high stability, reasonable times of operation and compatibility with other technological stages [333, 32].

3.5.3. High-energy cluster implantation

During the last 10-15 years, there has been considerable interest in implantation of high-energy (MeV) clusters showing specific phenomena like giant track and hillock formation in various target materials (Fig. 44) [41, 303, 368, 369, 370, 371, 372, 373]. Several models were applied to explain the hillock formation. Among the most popular are the shock wave, Coulomb explosion, ionic and thermal spike models. For such high energies one should also consider a so-called vicinage effect that leads to enhancement of the cluster stopping power compared to monomers as a result of interference in the excitation of target electrons by the simultaneous interactions with a few swift ions (cluster constituents or recoils). This phenomenon was experimentally observed for the first time on implantation of swift dimers and trimers of hydrogen into carbon and gold [53] and a little later it was explained

theoretically [374, 375]. Several years ago, the state in the field of high-energy cluster implantation has been summarized and analyzed by Chadderton [304]. A compound spike model including thermal and ion explosion spikes dominating at certain stages of the track formation was proposed. For the stopping power, contributions from each ion as well as from vicinage effects between the ions and from additional plasma stopping were suggested to be taken into account (Fig. 45) [305]. Despite minor discords of the existing approaches, the mechanism of hillock formation under MeV-energy bombardment can be ascribed to electronic stopping in the wake of the cluster constituents leading to local melting along the track, pushing out and quenching of the molten material.

One more interesting effect recently found on the MeV implantation of fullerenes into graphite is a phase transition yielding nanocrystals of diamond [43]. The very strong energy density deposited in electronic stopping generates a high enough temperature and intense outgoing recoil pressure pulses to produce a phase transition in the track region. The presence of crystalline diamond nanoparticles was found not only in the tracks but also around them on the surface. This is a confirmation of shock wave relaxation and hydrodynamic expansion causing the ejection of material from the near surface part of the track.

4. Conclusions and outlook

The study of the interaction of atomic (or molecular) clusters with surfaces is of increasing interest and activity in both academic and industrial domains. Deposition of size-selected nanoclusters or synthesis of thin layers with embedded nanoparticles opens new routes for the formation of electronic and optical devices, media for magnetic and catalytic applications, biocompatible systems etc. One of the advantages of the cluster beam technique compared to some other synthetic routes is in the possibility to decouple the particle formation which occurs inside a cluster source from the deposition process, leading to good control of the structure of the cluster assembled materials. The next important advantage is in adjustment of the cluster kinetic energy. By controlling the cluster-surface interaction regime one can

choose to produce very thin and atomically smooth films, dope ultra-shallow layers or provide high-yield sputtering and very efficient surface smoothing. A crucial factor for successful practical applications is a good understanding of the physical and chemical processes behind the cluster-surface interaction. A number of questions related to cluster soft-landing and the subsequent behaviour of atomic agglomerates on surfaces have been clarified. New systematic studies of electronic structure, optical, magnetic and catalytic properties of supported clusters provide (i) deeper knowledge of fundamental physics on the nanoscale as well as (ii) new synthetic routes for practical use of nano-systems and further development of such novel branches as plasmonics, spintronics and nanocatalysis. There are advances in applications of supported nanoparticles in biology and medicine. Despite the absence of a commonly-accepted theory of energetic cluster-surface interactions, a considerable success in the understanding of the sputtering process has been reached and several approaches towards the formulation of a universal theory of cluster stopping in matter have been developed.

Nevertheless, a number of fundamental physical aspects of cluster-surface interactions as well as numerous effects related to supported and embedded nanoparticles still need to be clarified. Theoretical simulations need further development of models and improvement of potentials that could more realistically describe the interaction of clusters of various species with different types of substrate materials. More systematic research with simulations matching experimental conditions as closely as possible would help clarify many of the still open questions.

References

[1] H. Haberland, (Ed.), Clusters of Atoms and Molecules, Springer-Verlag, Berlin, 1994.

[2] T. P. Martin, Phys. Rep. 273 (1996) 199.

[3] R. L. Johnston, Atomic and Molecular Clusters, Taylor&Francis, London, 2002.

[4] J. A. Alonso, Structure and Properties of Atomic Nanoclusters, Imperial College Press, London, 2005.

[5] F. Baletto, Rev. Mod. Phys. 77 (2005) 371.

[6] K.D. Sattler (Ed.), Handbook of Nanophysics: Clusters and Fullerenes, CRC Press, Boca Raton, 2010.

[7] P. Jena and A. W. Castleman [JR.], Proc. Nation. Acad. Sci. 103 (2006) 10560.

[8] A. Perez *et al.*, J. Phys. D: Appl. Phys. 30 (1997) 709.

[9] U. Kreibig and M. Vollmer, Optical Properties of Metal Clusters, Springer, Berlin, 1995.

[10] C. Binns, Surf. Sci. Rep. 44 (2001) 1.

[11] K. H. Meiwes-Broer, (Ed.), Metal Clusters at Surfaces, Springer, Berlin, 2000.

[12] R. E. Palmer, S. Pratontep, H. G. Boyen, Nature Mater. 2 (2003) 443.

[13] J. Bansmann et al., Surf. Sci. Rep. 56 (2005) 189.

[14] K. Wegner, P. Piseri, H. V. Tafreshi, P. Milani, J. Phys. D: Appl. Phys. 39 (2006) R439.

[15] E. Roduner, Nanoscopic Materials: Size-Dependent Phenomena, RSC Press, Cambridge, 2006.

[16] D.P. Woodruff (Ed.), The Chemical Physics of Solid Surfaces, Vol. 12, Atomic Clusters: From Gas Phase to Deposition, Elsevier, Amsterdam, 2007.

[17] C. Binns and J. A. Blackman, in J.A. Blackman (Ed.), Metallic Nanoparticles, Elsevier, Amsterdam, 2009, p. 277.

[18] W. E. Kaden, T. Wu, W. A. Kunkel, S. L. Anderson, Science 326 (2009) 826.

[19] K. H. Meiwes-Broer, W. Wurth, H. P. Steinrück, (Eds.), Focus on Clusters at Surfaces, New J. Phys. 4 (2002).

[20] H. Haberland, Z. Insepov, M. Karrais, M. Mall, M. Moseler, Y. Thurner, Mater. Sci. Eng. B 19 (1993) 31.

[21] H. Haberland, Z. Insepov, M. Moseler, Phys. Rev. B 51 (1995) 11061.

[22] P. Milani, M. Ferretti, P. Piseri, C. E. Bottani, A. Ferrari, A. Li Bassi, G. Guizzetti, M. Patrini, J. Appl. Phys. 82 (1997) 5793.

[23] V. Paillard, M. Meaudre, P. Melinon, V. Dupius, J. P. Perez, S. Vignoli, A. Perez, R. Meaudre, J. Non-Crystal. Sol. 191 (1995) 174.

[24] Y. Qiang, Y. Thurner, T. Reiners, O. Rattunde, H. Haberland, Surf. Coat. Technol. 100-101 (1998) 27.

[25] T. Kitagawa, I. Yamada, N. Toyoda, H. Tsubakino, J. Matsuo, G. H. Takaoka, A. Kirkpatrick, Nucl. Instr. Meth. Phys. Res. B 201 (2003) 405.

[26] J. Gspann, in T.P. Martin (Ed.), Large Clusters of Atoms and Molecules, Kluwer, Amsterdam, 1997, p. 443.

[27] P. Milani and S. Iannotta, Cluster Beam Synthesis of Nanostructured Materials, Springer, Berlin, 1999.

[28] I. Yamada, J. Matsuo, N. Toyoda, A. Kirkpatrick, Mater. Sci. Eng. R 34 (2001) 231.

[29] V. N. Popok and E. E. B. Campbell, Rev. Adv. Mater. Res. 11 (2006) 19.

[30] V. Popok, in K.D. Sattler (Ed.), Handbook of Nanophysics: Clusters and Fullerenes, CRC Press, Boca Raton, 2010, p. 19-1.

[31] V. N. Popok, Mater. Sci. Eng. R 72 (2011) 137.

[32] I. Yamada and N. Toyoda, Surf. Coat. Technol. 201 (2007) 8579.

[33] N. Toyoda and I. Yamada, IEEE Trans. Plasma Sci. 36 (2008) 1471.

[34] E. Bourelle, A. Suzuki, A. Sato, T. Seki, J. Matsuo, Nucl. Instr. Meth. Phys. Res. B 241 (2005) 622.

[35] W. Christen and U. Even, J. Phys. Chem. A 102 (1998) 9420.

[36] W. Christen and U. Even, Eur. Phys. J. D 9 (1999) 29.

[37] I. Yamada, J. Matsuo, E. C. Jones, D. Takeuchi, T. Aoki, K. Goto, T. Sugii, Mater. Res. Soc. Symp. Proc. 438 (1997) 363.

[38] B. Cvikl, D. Korosak, Z. J. Horvath, Vacuum 50 (1998) 385.

[39] J. Borland, J. Hautala, M. Gwinn, T. G. Tetreault, W. Skinner, Sol. State Technol. 47 (2004) 64.

[40] P. A. Thevenard, J. P. Dupin, B. Vu Thien, S. T. Purcell, V. Semet, Surf. Coat. Technol. 128-129 (2000) 59.

[41] M. Toulemonde, C. Trautmann, E. Balanzat, K. Hjort, A. Weidinger, Nucl. Instr. Meth. Phys. Res. B 216 (2004) 1.

[42] Z. Zhao, D. Qi, Z. Guo, Nucl. Instr. Meth. Phys. Res. B 217 (2004) 621.

[43] A. Dunlop, G. Jaskierowicz, P. M. Ossi, S. Della-Negra, Phys. Rev. B 76 (2007) 155403.

[44] E. W. Becker, K. Bier, W. Henkes, Z. Phys. 146 (1956) 333.

[45] W. Henkes, Z. Naturforshg. 16a (1961) 842.

[46] W. Henkes, Z. Naturforshg. 17a (1962) 786.

[47] J. Bauchert and O. F. Hagena, Z. Naturforschg. 20a (1965) 1135.

[48] H. Burghoff and J. Gspann, Z. Naturforschg. 22a (1967) 684.

[49] M. Dole, L. L. Mack, R. L. Hines, J. Chem. Phys. 49 (1968) 2240.

[50] M. Yamashita and J. B. Fenn, J. Phys. Chem. 88 (1984) 4451.

[51] C. Hao, R. E. March, T. R. S. C. Croley, S. P. Rafferty, J. Mass Spectrom. 36 (2001) 79.

[52] E. W. Becker, R. Klingelhöfer, H. Mayer, Z. Naturforschg. 23a (1968) 274.

[53]   W. Brandt, A. Ratkowski, R. H. Ritchie, Phys. Rev. Lett. 33 (1974) 1325.

[54]   R. Clampitt, K. L. Aitken, D. K. Jefferies, J. Vac. Sci. Technol. 12 (1975) 1208.

[55]   A. Dixon, C. Colliex, R. Ohana, P. Sudraud, J. Walle, Phys. Rev. Lett. 46 (1981) 865.

[56]   H. Helm and R. Möller, Rev. Sci. Instrum. 54 (1983) 837.

[57]   O. F. Hagena and W. Obert, J. Chem. Phys. 56 (1972) 1793.

[58]   E. O. Hogg and B. G. Silbernagel, J. Chem. Phys. 45 (1974) 593.

[59]   T. Takagi, I. Yamada, A. Sasaki, Thin Sol. Films 39 (1976) 207.

[60]   K. Kimoto and I. Nishida, J. Phys. Soc. Jpn. 42 (1977) 2071.

[61]   I. Yamada and T. Takagi, Thin Sol. Films 80 (1981) 105.

[62]   I. Yamada, H. Takaota, H. Usui, T. Takagi, J. Vac. Sci. Technol. A 4 (1986) 722.

[63]   J. B. Fenn, in Proc. 36th Ann. Conf., American Society for Mass Spectrometry, San
       Francisco, 5-10 June 1988, p. 773.

[64]   O. Echt, K. Sattler, E. Recknagel, Phys. Rev. Lett. 47 (1981) 1121.

[65]   W. D. Knight, K. Clemenger, W. A. de Heer, W. A. Saunders, M. Y. Chou, M. L. Cohen,
       Phys. Rev. Lett. 52 (1984) 2141.

[66]   V. E. Bondybey and J. H. English, J. Chem. Phys. 74 (1981) 6978.

[67]   T. G. Dietz, M. A. Duncan, D. E. Powers, R. E. Smalley, J. Chem. Phys. 74 (1981)
       6511.

[68]   R. E. Smalley, Laser Chem. 2 (1983) 167.

[69]   H. W. Kroto, J. R. Heath, S. C. O'Brien, R. E. Curl, R. E. Smalley, Nature 318 (1985)
       162.

[70]   G. Ganteför, H. R. Siekmann, H. O. Lutz, K. H. Meiwes-Broer, Chem. Phys. Lett. 165
       (1990) 293.

[71]   R. Middleton, Nucl. Instr. Meth. Phys. Res. 144 (1977) 337.

[72]   I. Katakuse, T. Ichihara, Y. Fujita, T. Matsuo, T. Sakurai, H. Matsuda, Int. J. Mass
       Spectrom. Ion Proces. 67 (1985) 229.

[73]   W. Begemann, K. H. Meiwes-Broer, H. O. Lutz, Phys. Rev. Lett. 56 (1986) 2248.

[74]   H. Haberland, M. Karrais, M. Mall, Y. Thurner, J. Vac. Sci. Technol. A 10 (1992) 3266.

[75]   S. Nonose, Y. Sone, K. Onodera, S. Sudo, K. Kaya, J. Phys. Chem. 94 (1990) 2744.

[76]   W. A. de Heer, Rev. Mod. Phys. 65 (1993) 611.

[77]   U. Heiz, A. Vaylovan, E. Schumacher, C. Yeretzian, M. Stener, P. Gisdakis, N. Rösch,
       J. Chem. Phys. 105 (1996) 5574.

[78]   W. Bouwen, P. Thoen, F. Vanhoutte, S. Bouckaert, F. Despa, H. Weidele, R. E.
       Silverans, P. Lievens, Rev. Sci. Instrum. 71 (2000) 54.

[79]   M. Brack, Rev. Mod. Phys. 65 (1993) 677.

[80]   A. W. Castleman and K. H. Bowen, J. Phys. Chem. 100 (1996) 12911.

[81]   P. Jensen, Rev. Mod. Phys. 71 (1999) 1695.

[82]   H. J. Gao, S. J. Pang, Z. Q. Xue, in D.L. Wise, G.E. Wnek, D.J. Trantolo, T.M. Cooper, J.D. Gresser (Eds.), Electrical and Optical Polymer Systems, Marcel Dekker, New York, 1998, p. 729.

[83]   T. Takagi, Mater. Sci. Eng. A 253 (1998) 30.

[84]   I. Yamada and J. Matsuo, Mater. Sci. Semicond. Proc. 1 (1998) 27.

[85]   S. J. Carroll, S. G. Hall, R. E. Palmer, R. Smith, Phys. Rev. Lett. 81 (1998) 3715.

[86]   I. Yamada, J. Matsuo, Z. Insepov, T. Aoki, T. Seki, N. Toyoda, Nucl. Instr. Meth. Phys. Res. B 164-165 (2000) 944.

[87]   S. J. Carroll, P. D. Nellist, R. E. Palmer, S. Hobday, R. Smith, Phys. Rev. Lett. 84 (2000) 2654.

[88]   T. J. Colla, R. Aderjan, R. Kissel, H. M. Urbassek, Phys. Rev. B 62 (2000) 8487.

[89]   Y. Yamaguchi and J. Gspann, Phys. Rev. B 66 (2002) 155408.

[90]   M. Moseler, O. Rattunde, J. Nordiek, H. Haberland, Nucl. Instr. Meth. Phys. Res. B 164-165 (2000) 522.

[91]   Y. Yamamura and T. Muramoto, Nucl. Instr. Meth. Phys. Res. B 72 (1992) 331.

[92]   R. S. Averback and M. Ghaly, Nucl. Instr. Meth. Phys. Res. B 90 (1994) 191.

[93]   W. Christen, U. Even, T. Raz, R. D. Levine, J. Chem. Phys. 108 (1998) 10262.

[94]   H. Pauly, Atom, molecule and cluster beams, V. 2, Springer, Berlin, Heidelberg, 2000.

[95]   F. Bakhtar, J. B. Young, A. J. White, D. A. Simpson, J. Mech. Eng. Sci. 219 (2005) 1315.

[96]   R. Weiel, Z. Phys. D 27 (1993) 89.

[97]   R. Campargue, J. Chem. Phys. 88 (1984) 4466.

[98]   D. R. Miller, in G. Scoles (Ed.), Atomic and Molecular Beam Methods, V. 1, Marcel Dekker, New York, 2004, p. 14.

[99]   K. Sattler, J. Mühlbach, E. Recknagel, Phys. Rev. Lett. 45 (1980) 821.

[100] A. S. Zolkin, J. Vac. Sci. Technol. A 15 (1997) 1026.

[101] I. M. Goldby, B. von Issendorff, L. Kuipers, R. E. Palmer, Rev. Sci. Instrum. 68 (1997) 3327.

[102] S. H. Baker, S. C. Thornton, K. W. Edmonds, M. J. Maher, C. Norris, C. Binns, Rev. Sci. Instrum. 71 (2000) 3178.

[103] O. Hagena, Rev. Sci. Instrum. 63 (1992) 2374.

[104] T. Seki, J. Matsuo, G. H. Takaoka, I. Yamada, Nucl. Instr. Meth. Phys. Res. B 206 (2003) 902.

[105] O. Hagena, in P.P. Wegener (Ed.), Molecular beams and low density gas dynamics, Dekker, New York, 1974, p. 93.

[106] O. Hagena, Z. Phys. D 4 (1987) 291.

[107] O. Hagena, Surf. Sci. 106 (1981) 101.

[108] C. L. Pettiette, S. H. Yang, M. J. Craycraft, J. Conceicao, R. E. Smalley, J. Chem. Phys. 88 (1988) 5377.

[109] O. Cheshnovsky, K. J. Taylor, J. Conceicao, R. E. Smalley, Phys. Rev. Lett. 64 (1990) 1785.

[110] N. Saito, K. Koyama, M. Tanimo, Appl. Surf. Sci. 169-170 (2001) 380.

[111] J. L. Rousset, A. M. Cardrot, F. J. Cadete Santos Aires, A. Renouprez, P. Melinon, A. Perez, M. Pellarin, J. L. Vialle, M. Broyer, J. Chem. Phys. 102 (1995) 8574.

[112] R. L. Wagner, W. D. Vann, A. W. Castleman, Rev. Sci. Instrum. 68 (1997) 3010.

[113] A. Wucher and M. Wahl, Nucl. Instr. Meth. Phys. Res. B 115 (1996) 581.

[114] W. Begemann, S. Dreihöfer, K. H. Meiwes-Broer, H. O. Lutz, in P. Jena, B.K. Rao, S.N. Khanna (Eds.), Physics and Chemistry of Small Clusters, Plenum Press, New York and London, 1987, p. 269.

[115] H. Haberland, M. Mall, M. Moseler, Y. Qiang, T. Reiners, Y. Thurner, J. Vac. Sci. Technol. A 12 (1994) 2925.

[116] H. R. Siekmann, C. Lüder, J. Faehrmann, H. O. Lutz, K. H. Meiwes-Broer, Z. Phys. D 20 (1991) 417.

[117] C. Y. Cha, G. Ganteför, W. Eberhardt, Rev. Sci. Instrum. 63 (1992) 5661.

[118] E. Barborini, P. Piseri, P. Milani, J. Phys. D: Appl. Phys. 32 (1999) 105.

[119] R. Methling, V. Senz, E. D. Klinkenberg, T. Diederich, J. Tiggesbäumker, G. Holzhüter, J. Bansmann, K. H. Meiwes-Broer, Eur. Phys. J. D 16 (2001) 173.

[120] A. Kleibert, J. Passig, K. H. Meiwes-Broer, M. Getzlaff, J. Bansmann, J. Appl. Phys. 101 (2007) 114318.

[121] Y. Saito and T. Noda, Z. Phys. D 12 (1989) 225.

[122] A. Bartelt, J. D. Close, F. Federmann, N. Quaas, J. P. Toennies, Phys. Rev. Lett. 77 (1996) 3525.

[123] S. Goyal, D. L. Schutt, G. Scoles, Phys. Rev. Lett. 69 (1992) 933.

[124] J. Tiggesbäumker and F. Stienkemeier, Phys. Chem. Chem. Phys. 9 (2007) 4748.

[125] P. Radcliffe, A. Przystawik, T. Diederich, T. Döppner, J. Tiggesbäumker, K. H. Meiwes-Broer, Phys. Rev. Lett. 92 (2004) 173403.

[126] T. Diederich, T. Döppner, T. Fennel, J. Tiggesbäumker, K. H. Meiwes-Broer, Phys. Rev. A 72 (2005) 23203.

[127] M. Hartmann, R. E. Miller, J. P. Toennies, A. Vilesov, Phys. Rev. Lett. 75 (1995) 1566.

[128] K. B. Whaley and R. E. Miller, (Eds.), Helium nanodroplets: a novel medium for chemistry and physics, J. Chem. Phys., Spec. Issue 115 (2001).

[129] D. Ievlev, I. Rabin, W. Schulze, G. Ertl, Chem. Phys. Lett. 328 (2000) 142.

[130] V. Mozhayskiy, M. Slipchenko, V. Adamchuk, A. Vilesov, J. Chem. Phys. 127 (2007) 94701.

[131] U. Buck and H. Meyer, Phys. Rev. Lett. 52 (1984) 109.

[132] U. Buck, J. Phys. Chem. 92 (1988) 1023.

[133] W. K. Murphy and G. W. Sears, J. Appl. Phys. 35 (1964) 1986.

[134] P. Liu, P. J. Ziemann, D. B. Kittelson, P. H. McMurry, Aerosol. Sci. Technol. 22 (1995) 293.

[135] P. Liu, P. J. Ziemann, D. B. Kittelson, P. H. McMurry, Aerosol. Sci. Technol. 22 (1995) 314.

[136] A. Gidwani, Ph.D. Thesis, University of Minnesota, Minneapolis (2003).

[137] F. Di Fonzo, A. Gidwani, M. H. Fan, D. Neumann, D. I. Iordanoglou, J. V. R. Heberlein, P. H. McMurry, S. L. Girshick, N. Tymiak, W. W. Gerberich, Appl. Phys. Lett. 77 (2000) 910.

[138] X. Wang, F. E. Kruis, P. H. McMurry, Aerosol. Sci. Technol. 39 (2005) 611.

[139] K. S. Lee, S. W. Cho, D. Lee, Aerosol Sci. 39 (2008) 287.

[140] J. Passig, K. H. Meiwes-Broer, J. Tiggesbäumker, Rev. Sci. Instrum. 77 (2006) 93304.

[141] P. Piseri, A. Podesta, E. Barborini, P. Milani, Rev. Sci. Instrum. 72 (2001) 2261.

[142] W. C. Wiley and I. H. McLaren, Rev. Sci. Instrum. 26 (1955) 1150.

[143] T. Bergmann, T. P. Martin, H. Schaber, Rev. Sci. Instrum. 60 (1989) 792.

[144] S. Pratontep, S. J. Carroll, C. Xirouchaki, M. Streun, R. E. Palmer, Rev. Sci. Instrum. 76 (2005) 45103.

[145] C. Binns, in J.A. Blackman (Ed.), Metallic Nanoparticles, Elsevier, Amsterdam, 2009, p. 49.

[146] P. Labastie, Int. J. Mass Spectrom. Ion Proces. 91 (1989) 105.

[147] W. Begemann, S. Dreihöfer, K. H. Meiwes-Broer, H. O. Lutz, Z. Phys. D 3 (1986) 183.

[148] B. Wrenger and K. H. Meiwes-Broer, Rev. Sci. Instrum. 68 (1997) 2027.

[149] P. M. Dinh, P. G. Reinhard, E. Suraud, Phys. Rep. 485 (2010) 42.

[150] A. M. Ferrari, C. Xiao, K. M. Neyman, G. Pacchioni, N. Rösch, Phys. Chem. Chem. Phys. 1 (1999) 4655.

[151] M. Moseler, H. Häkkinen, U. Landman, Phys. Rev. Lett. 89 (2002) 176103.

[152] B. Nacer, C. Massobrio, C. Félix, Phys. Rev. B 56 (1997) 10590.

[153] F. J. Palacios, M. P. Iniguez, M. J. López, J. A. Alonso, Phys. Rev. B 60 (1999) 2908.

[154] S. Vajda *et al.*, Nature Mat. 8 (2009) 213.

[155] A. Sanchez, S. Abbet, U. Heiz, W. D. Schneider, H. Häkkinen, R. N. Barnett, U. Landman, J. Phys. Chem. A 103 (1999) 9573.

[156] C. H. Yu, W. Oduro, K. Tam, E. S. C. Tsang, in J.A. Blackman (Ed.), Metallic Nanoparticles, Elsevier, Amsterdam, 2009, p. 365.

[157] A. Awasthi, S. C. Hendy, P. Zoontjens, S. A. Brown, Phys. Rev. Lett. 97 (2006) 186103.

[158] J. G. Partridge, S. A. Brown, A. D. F. Dunbar, R. Reichel, Nanotechnology 15 (2004) 1382.

[159] J. C. Jiménez-Sáez, A. M. C. Pérez-Martín, J. J. Jiménez-Rodríguez, Nucl. Instr. Meth. Phys. Res. B 249 (2006) 816.

[160] T. van Hoof, A. Dzhurakhalov, M. Hou, Eur. Phys. J. D 43 (2007) 159.

[161] L. Bardotti, B. Prével, P. Mélinon, A. Perez, Q. Hou, M. Hou, Phys. Rev. B 62 (2000) 2835.

[162] Q. Hou, M. Hou, L. Bardotti, B. Prével, P. Mélinon, A. Perez, Phys. Rev. B 62 (2000) 2825.

[163] C. K. Chen, S. C. Chang, C. L. Chen, J. Appl. Phys. 107 (2010) 124309.

[164] A. Kleibert, A. Voitkans, K.-H. Meiwes-Broer, Phys. Rev. B 81 (2010) 73412.

[165] A. Kleibert, A. Voitkans, K.-H. Meiwes-Broer, Phys. Stat. Sol. B 247 (2010) 1048.

[166] K. Sell, I. Barke, S. Polei, C. Schumann, V. von Oeynhausen, K. H. Meiwes-Broer, Phys. Stat. Sol. (b) 247 (2010) 1087.

[167] T. T. Järvi, A. Kuronen, K. Meinander, K. Nordlund, Phys. Rev. B 75 (2007) 115422.

[168] B. Pauwels, G. van Tendeloo, W. Bouwen, L. Theil-Kuhn, P. Lievens, H. Lei, M. Hou, Phys. Rev. B 62 (2000) 10383.

[169] Z. Y. Li, N. P. Young, M. Di Vece, S. Palomba, R. E. Palmer, A. L. Bleloch, B. C. Curley, R. L. Johnston, J. Jiang, J. Yuan, Nature 451 (2008) 46.

[170] K. Sell, A. Kleibert, V. v. Oeynhausen, K.-H. Meiwes-Broer, Eur. Phys. J. D 45 (2007) 433.

[171] R. Schaub, H. Jödicke, F. Brunet, R. Monot, J. Buttet, W. Harbich, Phys. Rev. Lett. 86 (2001) 3590.

[172] H. P. Cheng and U. Landman, Science 260 (1993) 1304.

[173] H. P. Cheng and U. Landman, J. Phys. Chem. 98 (1994) 3527.

[174] K. Bromann, C. Félix, H. Brune, W. Harbich, R. Monot, J. Buttet, K. Kern, Science 274 (1996) 956.

[175] S. Fedrigo, W. Harbich, J. Buttet, Phys. Rev. B 58 (1998) 7428.

[176] J. T. Lau, W. Wurth, H. U. Ehrke, A. Achleitner, Low Temp. Phys. 29 (2003) 223.

[177] S. Duffe, T. Irawan, M. Bieletzki, T. Richter, B. Sieben, C. Yin, B. von Issendorff, M. Moseler, H. Hövel, Eur. Phys. J. D 45 (2007) 401.

[178] S. Duffe, N. Grönhagen, L. Patryarcha, B. Sieben, C. Yin, B. von Issendorff, M. Moseler, H. Hövel, Nature Nanotech. 5 (2010) 335.

[179] G. L. Kellogg, Phys. Rev. Lett. 73 (1994) 1833.

[180] S. Liu, L. Bönig, H. Metiu, Phys. Rev. B 52 (1995) 2907.

[181] S. V. Khare, N. C. Bartelt, T. L. Einstein, Phys. Rev. Lett. 75 (1995) 2148.

[182] J. M. Wen, J. W. Evans, M. C. Bartelt, J. W. Burnett, P. A. Thiel, Phys. Rev. Lett. 76 (1996) 652.

[183] B. Yoon, V. M. Akulin, P. Cahuzac, F. Carlier, M. de Frutos, A. Masson, C. Mory, C. Colliex, C. Brechignac, Surf. Sci. 443 (1999) 76.

[184] M. H. Schaffner, J. F. Jeanneret, F. Patthey, W. D. Schneider, J. Phys. D: Appl. Phys. 31 (1998) 3177.

[185] B. Wortmann, K. Mende, S. Duffe, N. Grönhagen, B. von Issendorff, H. Hövel, Phys. Stat. Sol. B 247 (2010) 1116.

[186] L. Bardotti, P. Jensen, A. Hoareau, M. Treilleux, B. Cabaud, A. Perez, F. Cadete Santos Aires, Surf. Sci. 367 (1996) 276.

[187] R. Guerra, U. Tartaglino, A. Vanossi, E. Tosatti, Nature Mat. 9 (2010) 634.

[188] W. D. Luedtke and U. Landman, Phys. Rev. Lett. 82 (1999) 3835.

[189] Y. Maruyama, Phys. Rev. B 69 (2004) 245408.

[190] L. J. Lewis, P. Jensen, N. Combe, J. L. Barrat, Phys. Rev. B 61 (2000) 16084.

[191] P. Jensen, A. Clément, L. J. Lewis, Comp. Mat. Sci. 30 (2004) 137.

[192] M. Schmidt, N. Kébaïli, A. Lando, S. Benrezzak, L. Baraton, P. Cahuzac, A. Masson, C. Bréchignac, Phys. Rev. B 77 (2008) 205420.

[193] J. H. Ryu, H. Y. Kim, D. H. Kim, D. H. Seo, H. M. Lee, J. Phys. Chem. 114 (2010) 2022.

[194] G. L. Kellogg and A. F. Voter, Phys. Rev. Lett. 67 (1991) 622.

[195] W. Fan and X. G. Gong, Appl. Surf. Sci. 219 (2003) 117.

[196] G. Barcaro, A. Fortunelli, F. Nita, R. Ferrando, Phys. Rev. Lett. 95 (2005) 246103.

[197] M. Hou, V. S. Kharlamov, E. E. Zhurkin, Phys. Rev. B 66 (2002) 195408.

[198] K. Meinander and K. Nordlund, Phys. Rev. B 79 (2009) 45411.

[199] C. Binns et al., J. Phys. D: Appl. Phys. 38 (2005) R357.

[200] E. Barborini, P. Piseri, A. Podesta, P. Milani, Appl. Phys. Lett. 77 (2000) 1059.

[201] E. Magnano, M. Padovani, V. Spreafico, M. Sancrotti, A. Podesta, E. Barborini, P. Piseri, P. Milani, Surf. Sci. 544 (2003) L709.

[202] R. Reichel et al., Appl. Phys. Lett. 89 (2006) 213105.

[203] A. Perez, L. Bardotti, B. Prevel, P. Jensen, M. Treilleux, P. Mélinon, J. Gierak, G. Faini, D. Mailly, New J. Phys. 4 (2002) 76.

[204] C. H. Xu, X. Chen, Y. J. Liu, B. Xie, M. Han, F. Q. Song, G. H. Wang, Nanotechnology 21 (2010) 195304.

[205] R. Alayan, L. Arnaud, M. Broyer, E. Cottancin, J. Lermé, S. Marhaba, J. L. Vialle, M. Pellarin, Phys. Rev. B 76 (2007) 75424.

[206] J. L. Xu, J. L. Chen, J. Y. Feng, Nucl. Instr. Meth. Phys. Res. B 194 (2002) 297.

[207] C. Ducati, E. Barborini, P. Piseri, P. Milani, J. Robertson, J. Appl. Phys. 92 (2002) 5482.

[208] R. B. Heimann, S. E. Evsykov, L. Kavan, (Eds.), Carbine and Carbynoid Structures, Kluwer, Dordrecht, 1999.

[209] L. Ravagnan, F. Siviero, C. Lenardi, P. Piseri, E. Barborini, P. Milani, Phys. Rev. Lett. 89 (2002) 285506.

[210] N. Hiroshiba, K. Tanigaki, R. Kumashiro, H. Ohashi, T. Wakahara, T. Akasaka, Chem. Phys. Lett. 400 (2004) 235.

[211] L. Ma, J. Ouyang, Y. Yang, Appl. Phys. Lett. 84 (2004) 4786.

[212] H. Kim, J. Y. Kim, S. H. Park, K. Lee, Appl. Phys. Lett. 86 (2005) 183502.

[213] S. Yoo, B. Domercq, B. Kippelen, J. Appl. Phys. 97 (2005) 103706.

[214] V. N. Popok, I. I. Azarko, A. V. Gromov, M. Jönsson, A. Lassesson, E. E. B. Campbell, Sol. State Commun. 133 (2005) 499.

[215] L. Dunsh and S. Yang, Electrochem. Soc. Interf. 15 (2006) 34.

[216] V. N. Popok, M. Jönsson, E. E. B. Campbell, J. Nanosci. Nanotechnol. 7 (2007) 1434.

[217] V. N. Popok, A. V. Gromov, M. Jönsson, A. Taninaka, H. Shinohara, E. E. B. Campbell, Nano 3 (2008) 155.

[218] R. Carbone et al., Biomater. 27 (2006) 3221.

[219] L. Ravagnan, G. Divitini, S. Rebasti, M. Marelli, P. Piseri, P. Milani, J. Phys. D: Appl. Phys. 42 (2009) 82002.

[220] K. Judai, K. Sera, S. Amatsutsumi, K. Yagi, T. Yasuike, S. Yabushita, A. Nakajima, K. Kaya, Chem. Phys. Lett. 334 (2001) 277.

[221] J. Matsuo, E. Minami, M. Saito, N. Toyoda, H. Katsumata, I. Yamada, Eur. Phys. J. D 9 (1999) 635.

[222] N. Toyoda, Y. Fujiwara, I. Yamada, Nucl. Instr. Meth. Phys. Res. B 206 (2003) 875.

[223] O. Nakatsu, J. Matsuo, K. Omoto, T. Seki, G. Takaoka, I. Yamada, Nucl. Instr. Meth. Phys. Res. B 206 (2003) 866.

[224] J. Y. Kim, E. S. Kim, J. H. Choi, J. Appl. Phys. 91 (2002) 1944.

[225] Y. Fakuma, T. Murakami, H. Asada, T. Koyanagi, Physica E 10 (2001) 273.

[226] H. Yamashita and M. Anpo, Catal. Surv. Asia 8 (2004) 35.

[227] X. R. Zou, J. Q. Xie, J. Y. Feng, Surf. Coat. Technol. 111 (1999) 119.

[228] A. M. Zachary, I. L. Bolotin, D. J. Asunskis, A. T. Wroble, L. Hanley, Appl. Mat. Int. 1 (2009) 1770.

[229] H. Yasumatsu and T. Kondow, Rep. Prog. Phys. 66 (2003) 1783.

[230] R. D. Beck, P. St. John, M. M. Alvarez, F. Diederich, R. L. Whetten, J. Phys. Chem. 95 (1991) 8402.

[231] R. C. Mowrey, D. W. Brenner, B. I. Dunlap, J. W. Mintmire, C. T. White, J. Phys. Chem. 95 (1991) 7138.

[232] T. Moriwaki, H. Shiromaru, Y. Achiba, Z. Phys. D 37 (1996) 169.

[233] M. Benslimane, M. Chatelet, A. D. Martino, F. Pradere, H. Vach, Chem. Phys. Lett. 237 (1995) 323.

[234] M. Chatelet, M. Benslimane, A. D. Martino, F. Pradere, H. Vach, Chem. Phys. Lett. 50 (1996) 352.

[235] E. Fort, F. Pradere, A. D. Martino, H. Vach, M. Chatelet, Eur. Phys. J. D 1 (1998) 79.

[236] A. D. Martino, M. Chatelet, F. Pradere, E. Fort, H. Vach, J. Chem. Phys. 111 (1999) 7038.

[237] A. Terasaki, T. Tsukuda, H. Zasumatsu, T. Sugai, T. Kondow, J. Chem. Phys. 104 (1996) 1387.

[238] T. M. Bernhardt, B. Kaiser, K. Rademann, Z. Phys. D 40 (1997) 327.

[239] Y. Tai and J. Murakami, Chem. Phys. Lett. 339 (2001) 9.

[240] W. Christen and U. Even, Eur. Phys. J. D 24 (2003) 283.

[241] W. Christen and U. Even, Eur. Phys. J. D 16 (2001) 87.

[242] W. Christen, U. Even, T. Raz, R. D. Levine, Int. J. Mass Spectrom. Ion Process. 174 (1998) 35.

[243] E. Hendell, U. Even, T. Raz, R. D. Levine, Phys. Rev. Lett. 75 (1995) 2670.

[244] E. E. B. Campbell, T. Raz, R. D. Levine, Chem. Phys. Lett. 253 (1996) 261.

[245] E. E. B. Campbell and F. Rohmund, Rep. Prog. Phys. 63 (2000) 1061.

[246] R. D. Beck, J. Rockenberger, P. Weis, M. M. Kappes, J. Chem. Phys. 104 (1996) 3638.

[247] P. Weis, J. Rockenberger, R. D. Beck, M. M. Kappes, J. Chem. Phys. 104 (1996) 3629.

[248] A. Kaplan, A. Bekkerman, E. Gordon, B. Tsipinyuk, M. Fleischer, E. Kolodney, Nucl. Instr. Meth. Phys. Res. B 232 (2005) 184.

[249] A. Kaplan, A. Bekkerman, B. Tsipinyuk, E. Kolodney, Phys. Rev. B 79 (2009) 233405.

[250] T. Raz and R. D. Levine, in R.A. Dressler (Ed.), Chemical Dynamics in Extreme Environments, World Sci., Singapur, 2001, p. 20.

[251] A. Gross, H. Kornweitz, T. Raz, R. D. Levine, Chem. Phys. Lett. 354 (2002) 395.

[252] C. L. Cleveland and U. Landman, Science 257 (1992) 335.

[253] S. J. Carroll, P. Weibel, B. von Issendorff, L. Kuipers, R. E. Palmer, J. Phys.: Condens. Matter 8 (1996) L617.

[254] S. J. Carroll, S. Pratontep, M. Streun, R. E. Palmer, S. Hobday, R. Smith, J. Chem. Phys. 113 (2000) 7723.

[255] C. Bürgel, R. Mitric, V. Bonačić-Koutecky, Phys. Stat. Sol. (b) 247 (2010) 1099.

[256] M. Di Vece, S. Palomba, R. E. Palmer, Phys. Rev. B 72 (2005) 73407.

[257] S. Gibilisco, M. Di Vece, S. Palomba, G. Faraci, R. E. Palmer, J. Chem. Phys. 125 (2006) 84704.

[258] S. Vučković, J. Samela, K. Nordlund, V. N. Popok, Eur. Phys. J. D 52 (2009) 107.

[259] V. N. Popok, S. Vučković, J. Samela, T. Järvi, K. Nordlund, E. E. B. Campbell, Phys. Rev. B 80 (2009) 205419.

[260] R. Smith, C. Nock, S. D. Kenny, J. J. Belbruno, M. Di Vece, S. Palomba, R. E. Palmer, Phys. Rev. B 73 (2006) 125429.

[261] R. Smith, S. D. Kenny, J. J. Belbruno, R. E. Palmer, in D.P. Woodruff (Ed.), The Chemical Physics of Solid Surfaces, Vol. 12, Atomic Clusters: From Gas Phase to Deposition, Elsevier, Amsterdam, 2007, p. 589.

[262] J. G. Kushmerick, K. F. Kelly, H. P. Rust, N. J. Halas, P. S. Weiss, J. Phys. Chem. B 103 (1999) 1619.

[263] D. Marton, H. Bu, K. J. Boyd, S. S. Todorov, A. H. Al-Bayati, J. W. Rabalais, Surf. Sci. 326 (1995) L489.

[264] T. Seki, T. Murase, J. Matsuo, Nucl. Instr. Meth. Phys. Res. B 242 (2006) 179.

[265] R. E. Palmer and C. Leung, Trends Biotechnol. 25 (2007) 48.

[266] T. F. Watson, D. Belic, P. Y. Convers, E. J. Boyd, S. A. Brown, Eur. Phys. J. D (2011) DOI: 10.1140/epjd/e2010-00264-7.

[267] P. Sigmund, Nucl. Instr. Meth. Phys. Res. B 27 (1987) 1.

[268] K. L. Merke and W. Jäger, Philos. Mag. A 44 (1981) 741.

[269] I. H. Wilson, N. J. Zheng, U. Knipping, I. S. T. Tsong, Phys. Rev. B 38 (1988) 8444.

[270] F. Seitz and J. S. Koehler, in F. Seitz, D. Turnbull (Eds.), Solid State Physics: Advances in Research and Applications, Vol. 2, Academic, New York, 1956, p. 305.

[271] R. Kelly, Rad. Eff. 32 (1977) 91.

[272] A. Miotello and R. Kelly, Nucl. Instr. Meth. Phys. Res. B 122 (1997) 458.

[273] N. Toyoda, H. Kitani, N. Hagiwara, J. Matsuo, I. Yamada, Mater. Chem. Phys. 54 (1998) 106.

[274] N. Toyoda, H. Kitani, N. Hagiwara, T. Aoki, J. Matsuo, I. Yamada, Mater. Chem. Phys. 54 (1998) 262.

[275] L. P. Allen, Z. Insepov, D. B. Fenner, C. Santeufemio, W. Brooks, K. S. Jones, I. Yamada, J. Appl. Phys. 92 (2002) 3671.

[276] G. Bräuchle, S. Richard-Schneider, D. Illig, J. Rockenberger, R. D. Beck, M. M. Kappes, Appl. Phys. Lett. 67 (1995) 52.

[277] V. N. Popok, S. V. Prasalovich, E. E. B. Campbell, Surf. Sci. 566-568 (2004) 1179.

[278] V. N. Popok, S. V. Prasalovich, E. E. B. Campbell, Vacuum 76 (2004) 265.

[279] R. S. Averback, T. de La Diaz Rubia, H. Hsieh, R. Benedek, Nucl. Instr. Meth. Phys. Res. B 59/60 (1991) 709.

[280] R. Webb, M. Kerford, M. Kappes, G. Bräuchle, Nucl. Instr. Meth. Phys. Res. B 122 (1997) 318.

[281] Z. Insepov and I. Yamada, Nucl. Instr. Meth. Phys. Res. B 112 (1996) 16.

[282] E. E. Zhurkin and A. S. Kolesnikov, Nucl. Instr. Meth. Phys. Res. B 202 (2003) 269.

[283] J. Samela, K. Nordlund, J. Keinonen, V. N. Popok, E. E. B. Campbell, Eur. Phys. J. D 43 (2007) 181.

[284] K. Nordlund and J. Samela, Nucl. Instr. Meth. Phys. Res. B 267 (2009) 1420.

[285] T. Aoki, PhD Thesis, Kyoto University, 2000.

[286] S. V. Prasalovich, V. N. Popok, P. Person, E. E. B. Campbell, Eur. Phys. J. D 36 (2005) 79.

[287] V. N. Popok, J. Samela, K. Nordlund, V. P. Popov, Nucl. Instr. Meth. Phys. Res. B submitted.

[288] Z. Insepov, L. P. Allen, C. Santeufemio, K. S. Jones, I. Yamada, Nucl. Instr. Meth. Phys. Res. B 202 (2003) 261.

[289] V. N. Popok, J. Samela, K. Nordlund, E. E. B. Campbell, Phys. Rev. B 82 (2010) 201403(R).

[290] L. P. Allen, D. B. Fenner, C. Santeufemio, W. Brooks, J. Hautala, Y. Shao, Proc. SPIE 4806 (2002) 225.

[291] Z. Insepov, R. Manory, J. Matsuo, I. Yamada, Phys. Rev. B 61 (2000) 8744.

[292] J. Samela and K. Nordlund, Phys. Rev. B 81 (2010) 54108.

[293] T. Aoki, T. Seki, J. Matsuo, Vacuum 84 (2010) 994.

[294] R. C. Birtcher, A. W. McCormick, P. M. Baldo, N. Toyoda, I. Yamada, J. Matsuo, Nucl. Instr. Meth. Phys. Res. B 206 (2003) 851.

[295] K. A. Hollapse, Annu. Rev. Earth Planet. Sci. 21 (1993) 333.

[296] H. J. Melosh and B. A. Ivanov, Annu. Rev. Earth Planet. Sci. 27 (1999) 385.

[297] J. Samela and K. Nordlund, Phys. Rev. Lett. 101 (2008) 27601.

[298] K. Nordlund, T. T. Järvi, K. Meinander, J. Samela, Appl. Phys. A 91 (2008) 561.

[299] A. Audouard, R. Mamy, M. Toulemonde, G. Szenes, L. Thome, Europhys. Lett. 40 (1997) 527.

[300] V. A. Skuratov, D. L. Zagorski, A. E. Efimov, V. A. Kluev, Y. P. Toporov, B. V. Mchedlishvili, Radiat. Meas. 34 (2001) 571.

[301] C. Müller, M. Cranney, A. El-Said, N. Ishikawa, A. Iwase, M. Lang, R. Neumann, Nucl. Instr. Meth. Phys. Res. B 191 (2002) 246.

[302] V. A. Skuratov, S. J. Zinkle, A. E. Efimov, K. Havancsak, Surf. Coat. Technol. 196 (2003) 56.

[303] M. Döbeli, F. Ames, C. R. Musil, L. Scandella, M. Suter, H. A. Synal, Nucl. Instr. Meth. Phys. Res. B 143 (1998) 503.

[304] L. T. Chadderton, Radiat. Meas. 36 (2003) 145.

[305] S. A. Cruz, E. G. Gamaly, L. T. Chadderton, D. Fink, Radiat. Meas. 36 (2003) 145.

[306] K. Awazu, X. Wang, M. Fujimaki, T. Komatsubara, T. Ikeda, Y. Ohki, J. Appl. Phys. 100 (2006) 44308.

[307] E. Akcöltekin, T. Peters, R. Meyer, A. Duvunbeck, M. Klusmann, I. Monnet, H. Lebius, M. Schleberger, Nature Nanotech. 2 (2007) 290.

[308] V. N. Popok, J. Jensen, S. Vučković, A. Mackova, C. Trautmann, J. Phys. D: Appl. Phys. 42 (2009) 205303.

[309] A. Gruber and J. Gspann, J. Vac. Sci. Technol. B 15 (1997) 2362.

[310] J. H. Song and W. K. Choi, Nucl. Instr. Meth. Phys. Res. B 190 (2002) 792.

[311] V. N. Popok, V. S. Prasalovich, M. Samuelsson, E. E. B. Campbell, Rev. Sci. Instrum. 73 (2002) 4283.

[312] V. N. Popok, V. S. Prasalovich, E. E. B. Campbell, Nucl. Instr. Meth. Phys. Res. B 207 (2003) 145.

[313] R. Krämer, Y. Yamaguchi, J. Gspann, Surf. Interface Anal. 36 (2004) 148.

[314] J. Samela, K. Nordlund, V. N. Popok, E. E. B. Campbell, Phys. Rev. B 77 (2008) 75309.

[315] J. Samela, private communication.

[316] F. C. Zawislak, M. Behar, D. Fink, P. L. Grande, J. A. H. da Jornada, J. R. Kaschny, Phys. Lett. A 266 (1997) 217.

[317] I. Yamada and J. Matsuo, Mater. Res. Soc. Symp. Proc. 427 (1996) 265.

[318] N. Toyoda, N. Hagiwara, J. Matsuo, I. Yamada, Nucl. Instr. Meth. Phys. Res. B 161-163 (2000) 980.

[319] J. A. Greer, D. B. Fenner, J. Hautala, L. P. Allen, V. Di Filippo, N. Toyoda, I. Yamada, J. Matsuo, E. Minami, H. Katsumata, Surf. Coat. Technol. 133-134 (2000) 273.

[320] A. J. Perry, S. J. Bull, A. Dommann, M. Michler, B. P. Wood, D. Rafaja, J. N. Matossian, Surf. Coat. Technol. 140 (2001) 99.

[321] M. Döbeli, P. W. Nebiker, R. Mühle, M. Suter, Nucl. Instr. Meth. Phys. Res. B 132 (1997) 571.

[322] J. Matsuo, N. Toyoda, M. Akizuki, I. Yamada, Nucl. Instr. Meth. Phys. Res. B 121 (1997) 459.

[323] H. H. Andersen, A. Brunelle, S. Della-Negra, J. Depauw, D. Jacquet, Y. Le Beyec, J. Chaumont, H. Bernas, Phys. Rev. Lett. 80 (1998) 5433.

[324] S. Bouneau, A. Brunelle, S. Della-Negra, J. Depauw, D. Jacquet, Y. Beyec, M. Pautrat, M. Fallavier, J. C. Poizat, H. H. Andersen, Phys. Rev. B 65 (2002) 144106.

[325] Z. Insepov and I. Yamada, Nucl. Instr. Meth. Phys. Res. B 153 (1999) 199.

[326] J. Samela, K. Nordlund, V. N. Popok, E. E. B. Campbell, Phys. Rev. B 76 (2007) 125434.

[327] I. Yamada, J. Matsuo, N. Toyoda, T. Aoki, E. Jones, Z. Insepov, Mater. Sci. Eng. A 253 (1998) 249.

[328] H. Tokioka, H. Yamarin, T. Fujino, M. Inoue, T. Seki, J. Matsuo, Nucl. Instr. Meth. Phys. Res. B 257 (2007) 658.

[329] S. Kakuta, S. Sasaki, T. Hirano, K. Ueda, T. Seki, S. Ninomiya, M. Hada, J. Matsuo, Nucl. Instr. Meth. Phys. Res. B 257 (2007) 677.

[330] M. Moseler, O. Rattunde, J. Nordiek, H. Haberland, Comput. Mater. Sci. 10 (1998) 452.

[331] R. M. Bradley and J. M. E. Harper, J. Vac. Sci. Technol. A 6 (1988) 2390.

[332] H. Kitani, N. Toyoda, J. Matsuo, I. Yamada, Nucl. Instr. Meth. Phys. Res. B 121 (1997) 489.

[333] A. Kirkpatrick, Nucl. Instr. Meth. Phys. Res. B 206 (2003) 830.

[334] I. Yamada and N. Toyoda, J. Vac. Sci. Technol. A 23 (2005) 1090.

[335] T. Aoki and J. Matsuo, Nucl. Instr. Meth. Phys. Res. B 257 (2007) 645.

[336] M. P. Seah and I. S. Gilmore, Surf. Interface Anal. 43 (2011) 228.

[337] J. Gspann, Nucl. Instr. Meth. Phys. Res. B 112 (1996) 86.

[338] J. Peltola and K. Nordlund, Phys. Rev. B 68 (2003) 35419.

[339] C. F. Sanz-Navarro, R. Smith, D. J. Kenny, S. Pratontep, R. E. Palmer, Phys. Rev. B 65 (2002) 165420.

[340] X. L. Ma and W. Yang, Nanotechnol. 15 (2004) 449.

[341] L. Shao, M. Nastasi, X. Wang, J. Liu, W. K. Chu, Nucl. Instr. Meth. Phys. Res. B 242 (2006) 503.

[342] Y. Yamamura, Nucl. Instr. Meth. Phys. Res. B 33 (1988) 493.

[343] Y. Yamamura and T. Muramoto, Rad. Eff. Def. Sol. 130-131 (1994) 225.

[344] V. I. Shulga and P. Sigmund, Nucl. Instr. Meth. Phys. Res. B 47 (1990) 236.

[345] V. I. Shulga, M. Vicanek, P. Sigmund, Phys. Rev. A 39 (1989) 3360.

[346] T. Aoki, T. Seki, J. Matsuo, Ext. Abstract 10th International Workshop Junction Technol. (2010) DOI: 10.1109/IWJT.2010.5474974.

[347] G. H. Gilmer, C. Roland, D. Stock, M. Jaraiz, T. de La Diaz Rubia, Mater. Sci. Eng. B 37 (1996) 1.

[348] C. Anders and H. M. Urbassek, Nucl. Instr. Meth. Phys. Res. B 228 (2005) 57.

[349] H. Hsieh, T. de La Diaz Rubia, R. S. Averback, Phys. Rev. B 40 (1989) 9986.

[350] Y. Hada, Physica B 340-342 (2003) 1036.

[351] H. H. Andersen, A. Johansen, M. Olsen, V. Touboltsev, Nucl. Instr. Meth. Phys. Res. B 212 (2003) 56.

[352] C. T. Reimann, S. Andersson, P. Brühwiler, N. Mårtensson, L. Olsson, R. Erlandsson, M. Henkel, H. M. Urbassek, Nucl. Instr. Meth. Phys. Res. B 140 (1998) 159.

[353] J. H. Liang and H. M. Han, Nucl. Instr. Meth. Phys. Res. B 228 (2005) 250.

[354] H. Chang and A. Bard, J. Am. Chem. Soc. 113 (1991) 558.

[355] F. Stevens, L. Kolodny, T. Beebe, J. Phys. Chem. B 102 (1998) 10799.

[356] S. Pratontep, P. Preece, C. Xirouchaki, R. E. Palmer, C. F. Sanz-Navarro, S. D. Kenny, R. Smith, Phys. Rev. Lett. 90 (2003) 55503.

[357] L. Seminara, P. Convers, R. Monot, W. Harbich, Eur. Phys. J. D 29 (2004) 49.

[358] T. Aoki, J. Matsuo, G. Takaoka, Nucl. Instr. Meth. Phys. Res. B 202 (2003) 278.

[359] M. Henkel and H. M. Urbassek, Nucl. Instr. Meth. Phys. Res. B 145 (1998) 503.

[360] T. Aoki, J. Matsuo, G. Takaoka, Mater. Res. Soc. Symp. Proc. 669 (2001) J4.5.1.

[361] J. Y. Jin, J. Liu, P. A. W. Heide, W. K. Chu, Appl. Phys. Lett. 76 (2000) 574.

[362] A. I. Titov, A. Y. Azarov, L. M. Nikulina, S. O. Kucheyev, Nucl. Instr. Meth. Phys. Res. B 256 (2007) 207.

[363] A. Akizuki, J. Matsuo, I. Yamada, M. Harada, S. Ogasawara, A. Doi, Nucl. Instr. Meth. Phys. Res. B 112 (1996) 83.

[364] J. R. Engstrom, D. J. Bonser, M. M. Nelson, T. Engel, Surf. Sci. 256 (1991) 317.

[365] A. P. Caricato, M. de Sario, M. Fernandez, G. Leggieri, A. Luches, M. Martino, F. Prudenzano, Appl. Surf. Sci. 197-198 (2002) 458.

[366] A. Cremona, L. Laguardia, E. Vassallo, G. Ambrosone, U. Coscia, F. Orsini, G. Poletti, J. Appl. Phys. 97 (2005) 23533.

[367] X. Lu, L. Shao, X. Wang, J. Liu, W. K. Chu, J. Bennet, L. Larson, P. Ling, J. Vac. Sci. Technol. B 20 (2002) 992.

[368] H. Dammak, A. Dunlop, D. Lesueur, Phys. Rev. Lett. 74 (1995) 1135.

[369] A. Brunelle, S. Della-Negra, J. Depauw, D. Jacquet, Y. Beyec, M. Pautrat, C. Schoppmann, Nucl. Instr. Meth. Phys. Res. B 125 (1997) 207.

[370] S. M. M. Ramos, N. Bonardi, B. Canut, S. Bouffard, S. Della-Negra, Nucl. Instr. Meth. Phys. Res. B 143 (1998) 319.

[371] P. Thevenard, J. P. Dupin, P. T. Vu Thien Binh, V. Semet, D. Guillot, Nucl. Instr. Meth. Phys. Res. B 166-167 (2000) 788.

[372] J. C. Giard, A. Michel, C. Tromas, C. Jaouen, S. Della-Negra, Nucl. Instr. Meth. Phys. Res. B 209 (2003) 85.

[373] A. Dunlop, G. Jaskierowicz, S. Della-Negra, Nucl. Instr. Meth. Phys. Res. B 146 (1998) 302.

[374] N. R. Arista and V. H. Ponce, J. Phys. C 8 (1975) L188.

[375] N. R. Arista, Phys. Rev. B 18 (1978) 1.

[376] K. Sell, PhD Thesis, University of Rostock, 2010.

Figure Captions

Fig. 1. Cluster size and local temperature of a 143 hPa MgF_2 vapour expanding in 4000 hPa Argon. Crucible temperature 2200 K, nozzle diameter 0.3 mm, nozzle opening angle 5°. x-axis: distance from nozzle, in units of the diameter D. Reprinted with kind permission from [96], Springer+Business Media B.V.

Fig. 2: Mass spectrum of sputtered Cu_n by using 20 keV Xe^+ ions as projectiles. Note that these clusters are generated from single high-energy ion impacts in ultra-high vacuum. Reprinted with kind permission from [114], Springer+Business Media B.V..

Fig. 3. (Color online) (a) The principle of magnetron sputtering and (b) typical eroded copper targets used for the cluster production.

Fig. 4. (Color online) Schematic view of arc-discharge cluster ion source ACIS including a mass separation unit and deposition chamber. The clusters are produced in ACIS, steered through the skimmers towards an electrostatic quadrupole mass filter where they are size-selected and deflected by 90° towards the next vacuum chamber for deposition on a sample mounted on a manipulator. Ions optics components are used to focus the beam in the plane of the sample and quartz microbalance is used for control of the deposition. Reprinted with kind permission from [119], Springer+Business Media B.V.

Fig. 5. The principle of size selection and focusing in the aerodynamic lenses. Only particles with Stokes numbers, St ~ 1 are able to pass through the set of lenses. See text for more details. Reprinted with permission from [14].

Fig. 6. Calculated flow streamlines (top) and particle trajectories (bottom) in the aerodynamic lens assembly. Reprinted with permission from [137]. Copyright 2000, American Institute of Physics.

Fig. 7. (Color online) Size distribution of Cu_n clusters obtained with and without a system of aerodynamic lenses. Details are in the text. Reprinted with permission from [140]. Copyright 2006, American Institute of Physics.

Fig. 8. Focusing nozzle assembly: (a) cross-sectional and (b) perspective views. The focusing (mass selection) mechanism is shown in (c). Reprinted with permission from [14].

Fig. 9. Schematic picture of (a) high-frequency quadrupole mass filter and (b) cross section of the rods. Four cylindrical rods are mounted very accurately in parallel. Pairs of opposing rods are electrically connected. A potential *V+Vcos(ωt)* is applied to one pair of rods and – *(V+Vcos(ωt))* to the other. Only cluster ions having a specific charge-to-mass ratio, defined by the applied voltages, can pass through the filter.

Fig. 10. TEM images of size-selected clusters obtained from the ACIS by tuning the quadrupole deflector voltages from (a) 100 V to (b) 1000 V. Mean particle sizes are 5.0 ± 1.0 and 14.0 ± 1.8 nm, respectively. Reprinted with permission from [376].

Fig. 11. Schematic of (a) cluster soft landing and (b) cluster-surface high-energy impact.

Fig. 12. Snapshots of MD simulations of Au_{440} cluster deposition on Au(111) at different times after initial contact. Full epitaxial alignment to the surface is achieved after 100 ps. Reprinted with permission from [162]. Copyright 2000 by the American Physical Society.

Fig. 13. Diffraction (RHEED) images of Fe_n clusters (diameter of 13 nm) deposited on W(110). (a) pronounced diffraction rings are visible for the as-deposited sample, indicating random orientation. (b) Upon annealing the rings diminish and the intensity of diffraction spots increases due to epitaxial alignment to the substrate. Reprinted with permission from [165].

Fig. 14. STM image of a silver cluster soft-landed on Si(111)-(7x7). A non-linear grey scale has been used to emphasize the atomically resolved surface reconstruction. Reprinted with permission from [166].

Fig. 15. (a) STEM image of coagulated Sb_4 clusters deposited on amorphous carbon, (b) AFM image of ramified island formation after deposition of Sb_{2300} clusters. Panel (a) reprinted from [183] with permission from Elsevier, panel (b) reprinted with permission from [8].

Fig. 16. (Color online) (a) Gold cluster consisting of 459 atoms modeled by a truncated octahedron in contact to a graphite surface via the (111) facet. (b) The contact facet may either be in registry with the surface lattices (I) or out-of-registry (II). Diffusion barriers are considerably lower in the latter case, resulting in large diffusion constants. Reprinted by permission from Macmillan Publishers Ltd: [187].

Fig. 17. (Color online) (a) AFM image of pleated graphite surface. Narrow, almost one-dimensional regions of convex (concave) surface bending are formed that act repulsive (attractively) on diffusing particles. (b) SEM image of Ag clusters deposited on pleated graphite. In this panel, besides ramified islands (c) the clusters form quasi one-dimensional chains between concave bends (d) and at step edges (e). The bends are indicated by dotted lines (f). Reprinted with permission from [192]. Copyright 2008 by the American Physical Society.

Fig. 18. MD simulations of Mo_{1043} clusters impacting on Mo (001) surface with (a) 0.1 eV, (b) 1 eV and (c) 10 eV kinetic energy per cluster atom. Reprinted with permission from [21]. Copyright 1995 by the American Physical Society.

Fig. 19. (a) Schematic representation of cluster beam deposition through a stencil mask. (b) SEM image of a pattern of pillars obtained with a round hole grid with 850 mesh and holes of

20 μm diameter. Reprinted with permission from [200]. Copyright 2000, American Institute of Physics.

Fig. 20. (a) Bi cluster-assembled wire extending over a planar Ti/Au fourpoint contact layout and supported on a Si_3N_4 passivated Si substrate and (b) a Bi cluster-assembled wire with a minimum width of 30 nm, supported on a SiO_2 passivated Si substrate. Reprinted with permission from [202]. Copyright 2006, American Institute of Physics.

Fig. 21. TEM micrograph of size-selected platinum clusters deposited on amorphous carbon. Inset shows how particles tend to assemble in close-packed arrays without direct contact. Reprinted with permission from [205]. Copyright 2007 by the American Physical Society.

Fig. 22. TEM micrographs (cross-sectional cuts) of PMMA with Pd nanoparticles deposited on the surface with different nominal thicknesses and substrate temperatures: (a) 1 nm at room temperature and (b) below 1 nm at 95 ^{o}C, Reprinted with permission from [219].

Fig. 23. (Color online) Schematic view of possible processes on energetic cluster-surface impact. Reprinted with permission from [229].

Fig. 24. Reaction yield of molecular iodine I_2^- as a function of the size n of the impacting iodomethane cluster anions $(CH_3I)_n^-$. Both the reaction yield and the fragment ion signal are taken at E_{kin} of the impacting cluster ions around 200 eV. The solid line is a fit to the data points. Reprinted with permission from [35]. Copyright 1998, American Chemical Society.

Fig. 25. The pinning threshold energies on HOPG as a function of size for (a) gold and (b) nickel clusters as obtained by experiments and calculations. Reprinted with permission from [256]. Copyright 2005 by the American Physical Society.

Fig. 26. (Color online) Simulated images of clusters on a graphite surface: (a) Ni_{55}; (b) Au_{55}; (c) Ni_{100}; (d) Au_{100}. Cluster energies are above the pinning thresholds. Reprinted with permission from [260]. Copyright 2006 by the American Physical Society.

Fig. 27. (Color online) AFM image of craters formed on a sapphire surface after impact of 9 keV Ar_{12}^+ cluster ions.

Fig. 28. Snapshots of MD simulation of 650 keV Au_{13} cluster impact on gold: (a) sputtering of surface atoms and (b) crater formation after 16 ps. Reprinted with permission from [315].

Fig. 29. Snapshots of MD simulation of Ar_{688} cluster impact on Si with E_{at} = 80 eV. Three sequential panels (a, b and c) show the development in distribution of momenta of atoms as a function of time. Reprinted with permission from [285].

Fig. 30. TEM cross-sectional images of craters formed on (a) individual 24 keV Ar_n^+ cluster ion impact on Si(100) and (b) individual 24 keV $(O_2)_n^+$ cluster ion impact on Si(111). Reprinted from [288] with permission from Elsevier.

Fig. 31. (Color online) Dependence of crater depth and radius on energy for Ar_{2000} clusters impacting on silicon. Reprinted from [293] with permission from Elsevier.

Fig. 32. (Color online) AFM image showing hillock formation on a Si surface after bombardment of 6 keV Ar_{12}^+ cluster ions.

Fig. 33. (Color online) AFM image of complex craters formed on the surface of silicon after 18 keV Ar_{12}^+ cluster ion implantation.

Fig. 34. MD simulations of the number of atoms having velocities larger than a given value in crystalline silicon as function of time after impact of keV-energy Ar_{12} cluster. The inset shows a cross-sectional snapshot of the impact area. Arrows depict collective movements of the target atoms in various directions. Colors of the arrows coincide with the colors of the number versus time plot, corresponding to the same direction of movement. Reprinted with permission from [315].

Fig. 35. Angular distribution of Cu atoms sputtered by Ar monomers and cluster ions at normal incidence. Reprinted from [28] with permission from Elsevier.

Fig. 36. Schematic picture of surface smoothing on cluster impact. Reprinted from [318] with permission from Elsevier.

Fig. 37. Scanning electron microscope images of cross sections of a silicon microstructure before and after SF_6 gas cluster irradiation. (a) Wide view of a silicon trench array fabricated by inductive coupled plasma reactive ion etching. Expanded image of sidewalls of trenches (b) before and (c) after irradiation by SF_6 gas clusters at an incident angle of 83° from the surface normal to the sidewall. The energy and the ion dose of the SF_6 clusters are 30 keV and 1.5×10^{15} ion/cm^2, respectively. Reprinted from [34] with permission from Elsevier.

Fig. 38. Mean depth of displacements in Si as a function of kinetic energy of impacting Ar_n clusters. Reprinted with permission from [285].

Fig. 39. The implantation depth for Au_7, Ag_7 and Si_7 clusters in graphite as a function of momentum. The dashed lines are the best fit straight lines. The filled circles are the depths of the damage tracks from MD simulations for Si_7. The crosses are the calculated centre-of-mass cluster implantation depths. Reprinted with permission from [356]. Copyright 2003 by the American Physical Society.

Fig. 40. (a) Experimentally found and (b) theoretically simulated dependences of depth of etched pits (in number of graphene layers) on scaled momentum for implantation of size-selected cobalt and argon clusters. Dashed line shows the best fit straight line for the experimental data.

Fig. 41. Model of damage formation by impact of large and small clusters. Reprinted with permission from [285].

Fig. 42. Simulated dependencies of the mean depth of implanted B constituents and interstitial Si atoms (radiation damage) on the size (in number of atoms) of boron clusters. Reprinted with permission from [346].

Fig. 43. Cross-sectional SEM image of a p-MOSFET fabricated using implantation of $B_{10}H_{14}$ clusters. Reprinted from [28] with permission from Elsevier.

Fig. 44. High resolution transmission electron microscopy image of tracks formed on Si bombarded with 30 MeV C_{60} clusters. The image is taken along the <111> direction. Reprinted from [373] with permission from Elsevier.

Fig. 45. Schematic picture showing a collision of high-energy C_{60} with a surface. Cascades of ions can be initiated inside the high-energy cluster projectile. There is a 'critical scattering angle' θ_L, following collision with a target atom, made by a leading carbon ion on one side of the moving C_{60} cluster, which leads to direct collision with a neighboring carbon on the other side, and thus to a displacement avalanche. This is a nuclear vicinage phenomenon. Reprinted from [305] with permission from Elsevier.

Fig. 1

Fig. 2
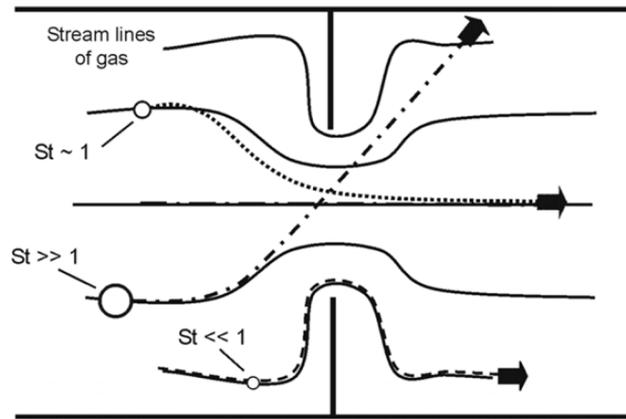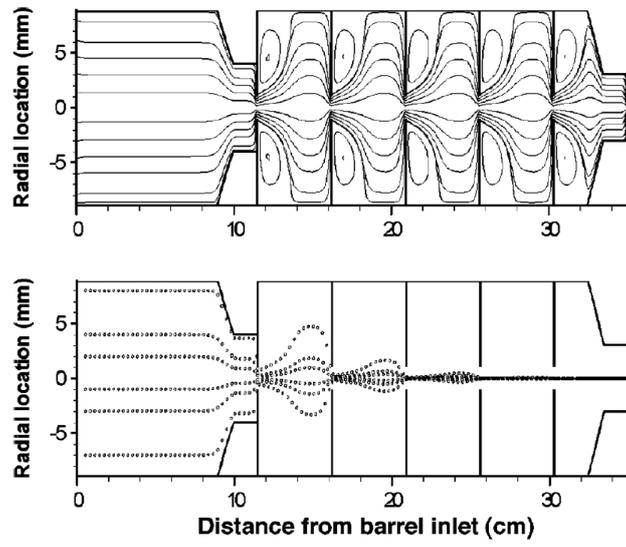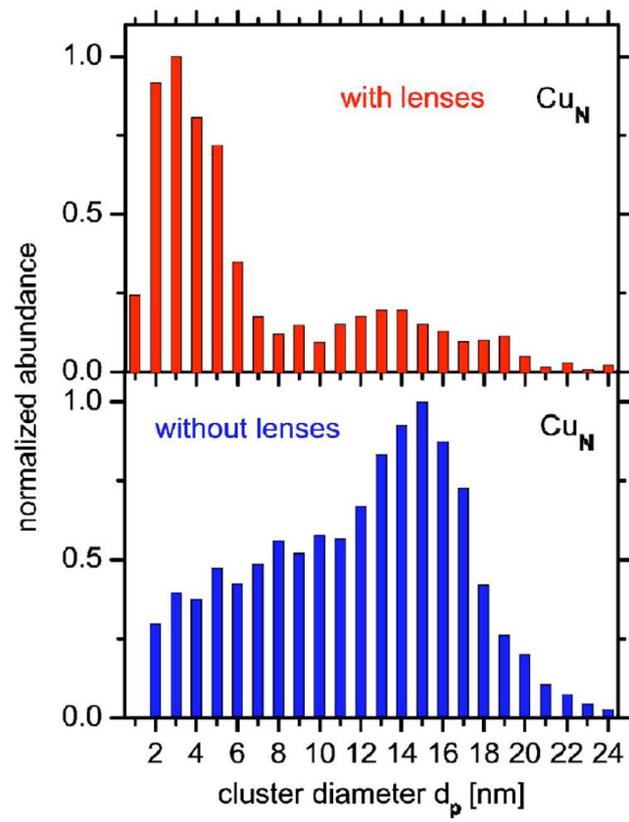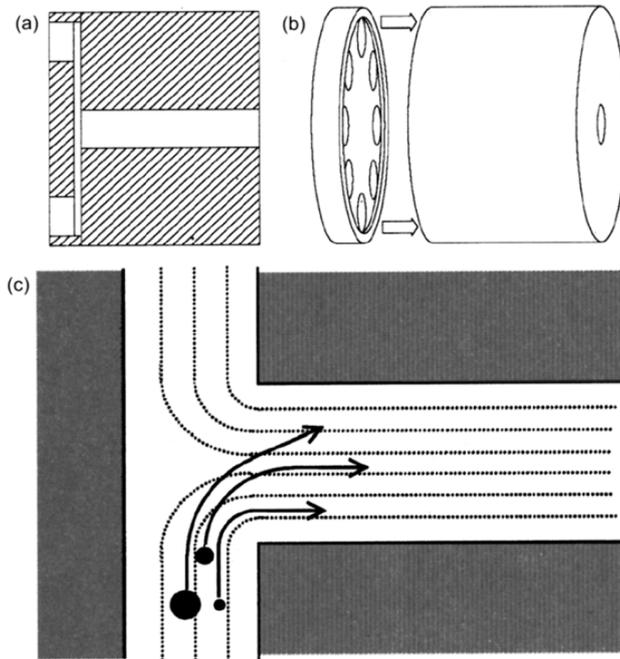
a)

Plasma torus

Magnetic field lines

S   N   S

Cathode

Magnetic field lines

Erosion trench   Electron trajectories

b)

Fig. 3

Fig. 4

Fig. 5

Fig. 6

Fig. 7

Fig. 8
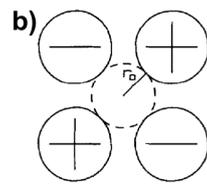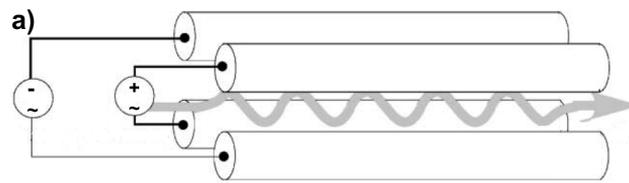
Fig. 9
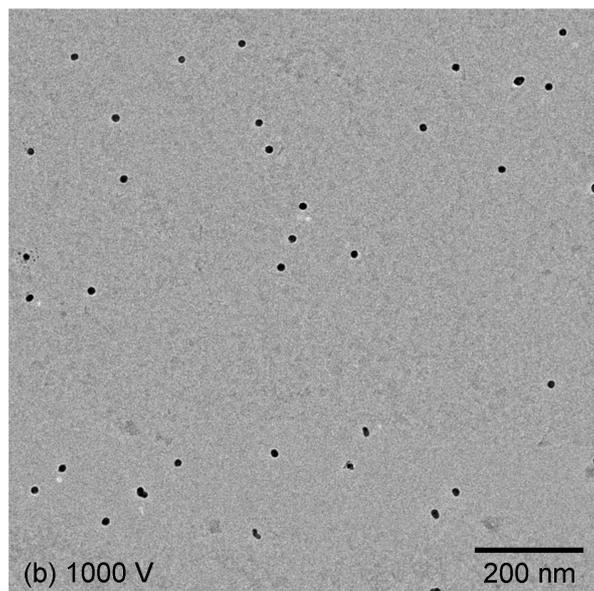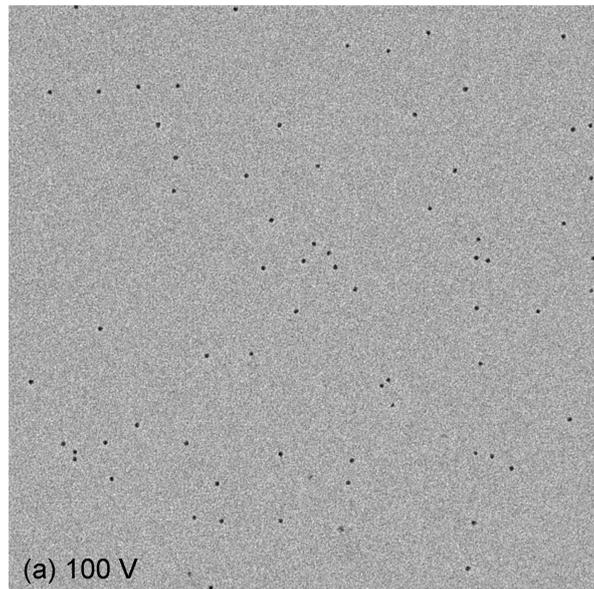
(a) 100 V

(b) 1000 V

200 nm

Fig. 10

Fig. 11

a) t = 0 ps

b) t = 4 ps

c) t = 16 ps

d) t = 100 ps

Fig. 12

Fig. 13

Fig. 14

Fig. 15

a

b

(I)   (II)

Fig. 16

Fig. 17

Fig. 18

(a)

cluster beam

mask   substrate

(b)

100 μm

Fig. 19

(a)   (b)

Fig. 20

Fig. 21

(a)

PMMA surface

50 nm

250 nm

(b)

PMMA surface

70 nm

250 nm

Fig. 22

Size-selected cluster

Reactive scattering

Non-dissociative scattering with vibrational excitation

Migration Deposition

Implantation
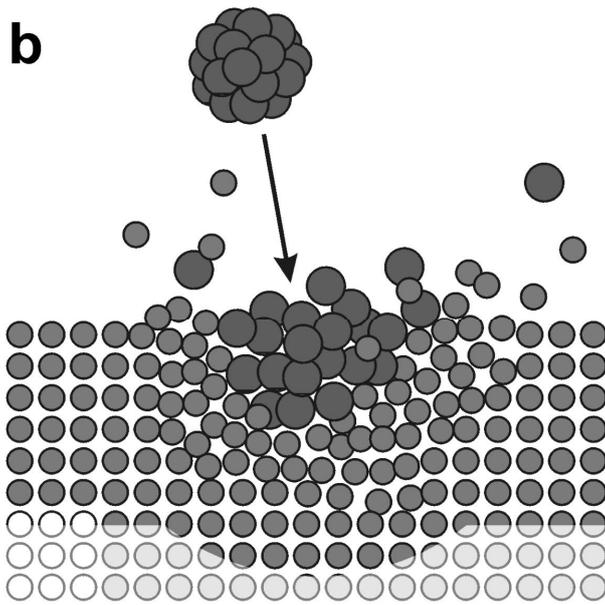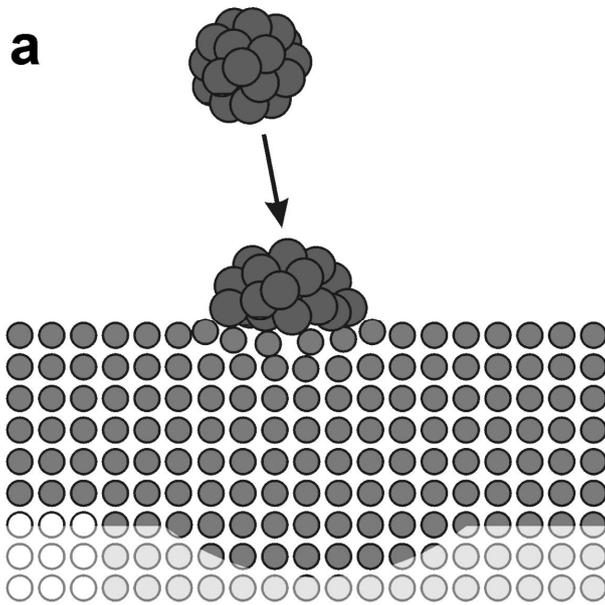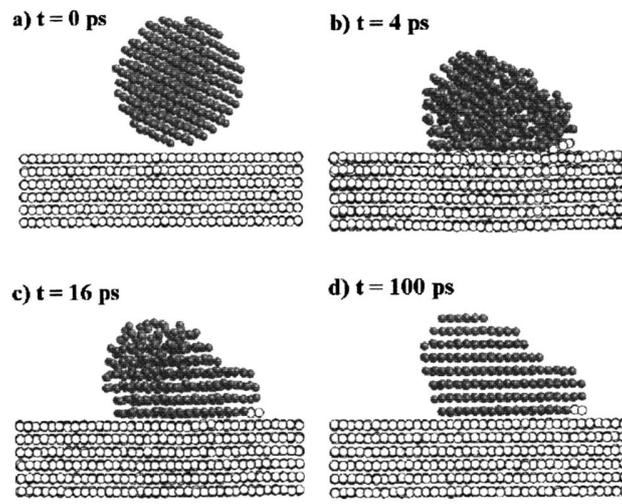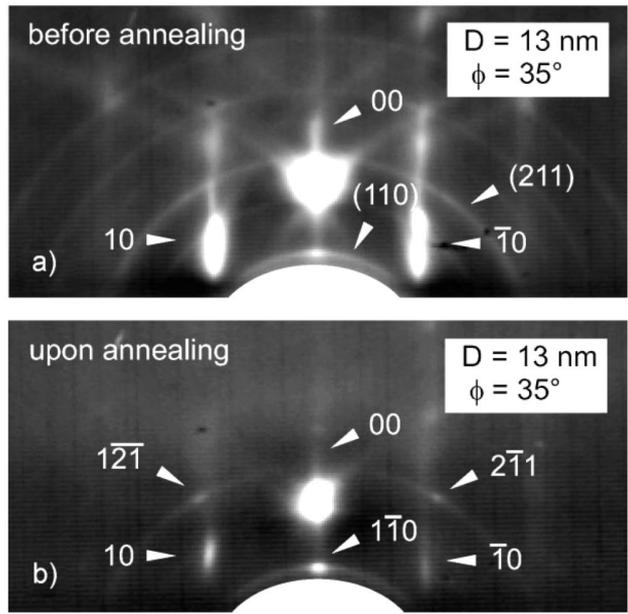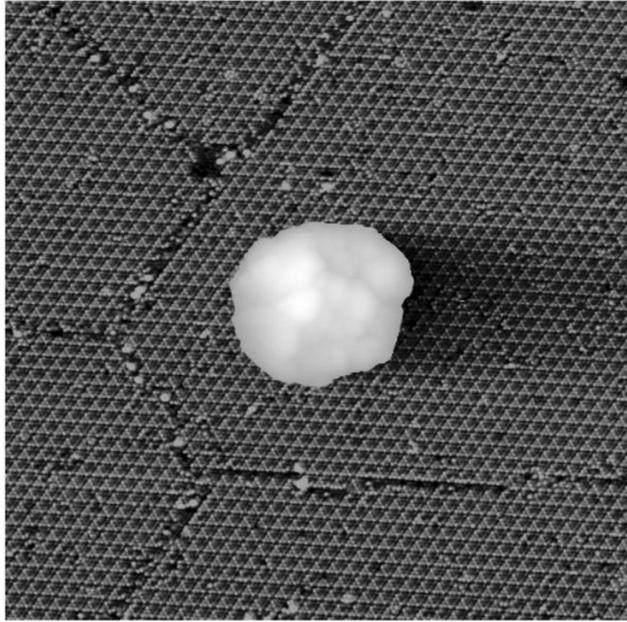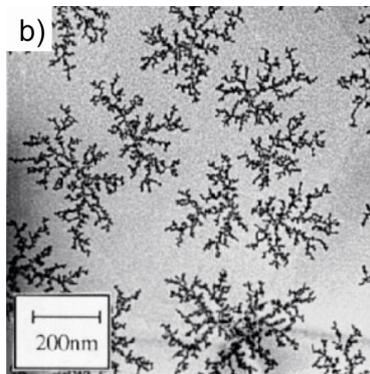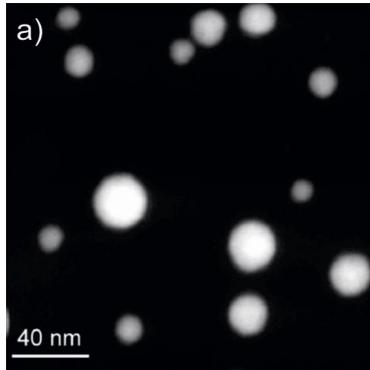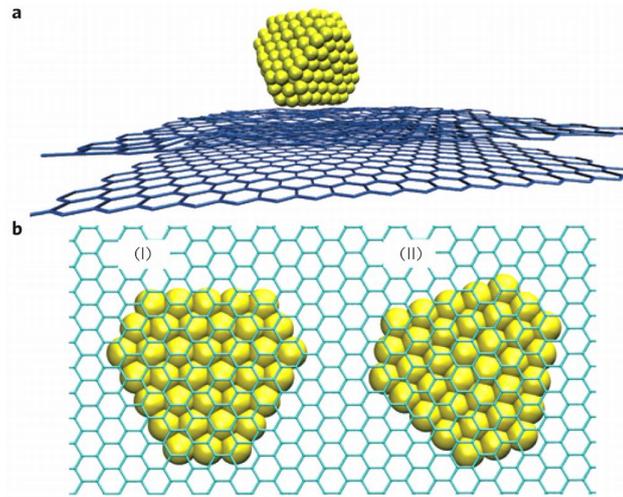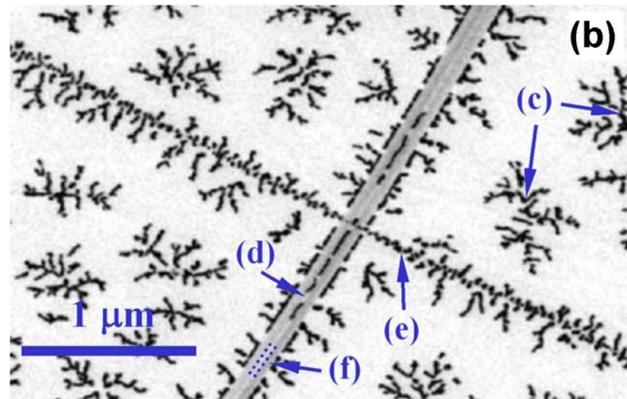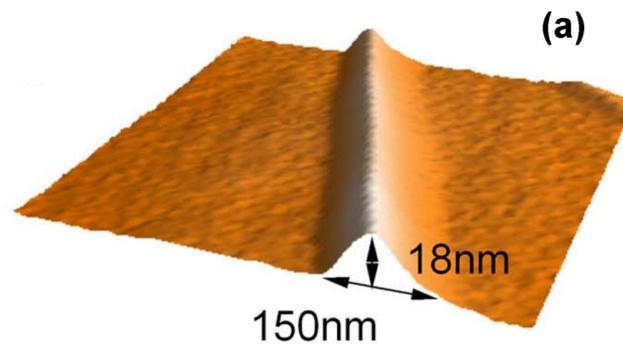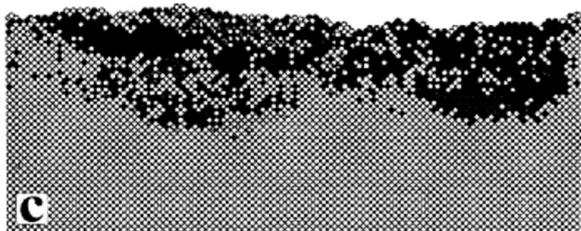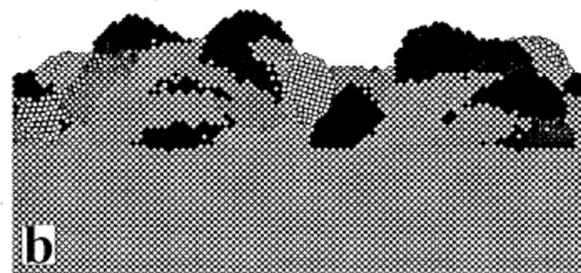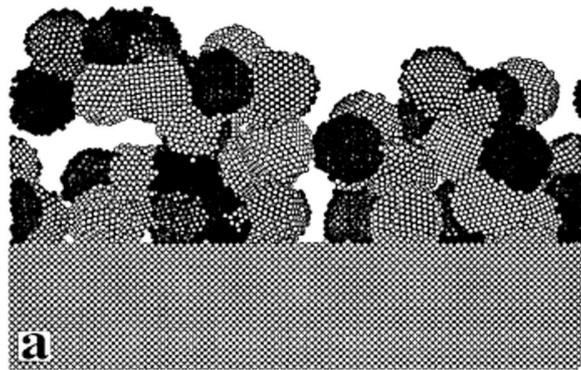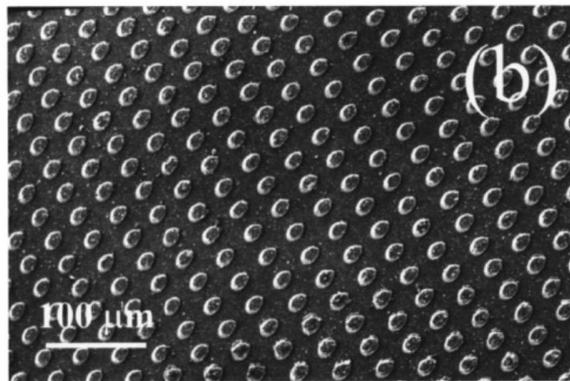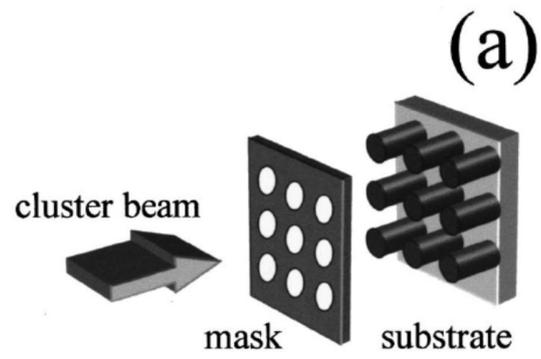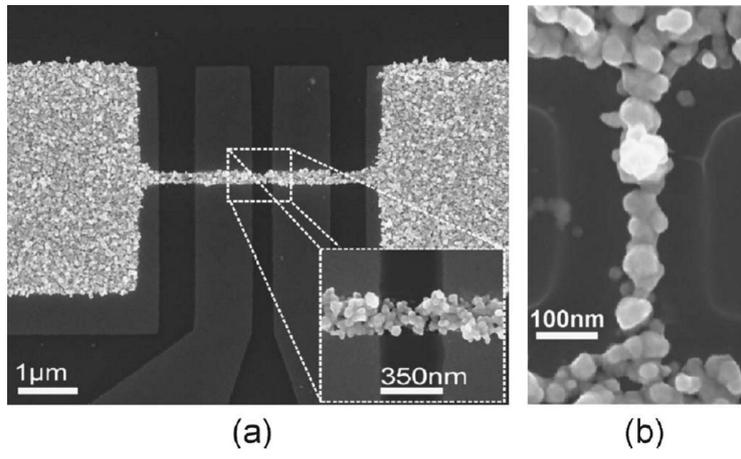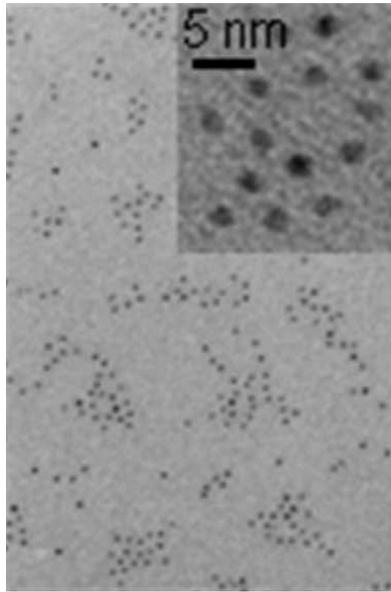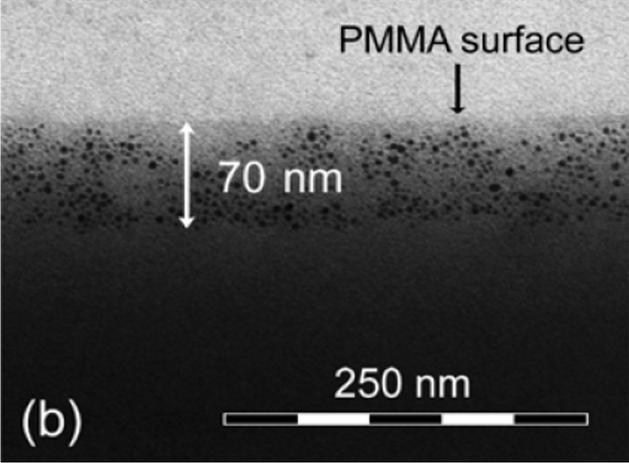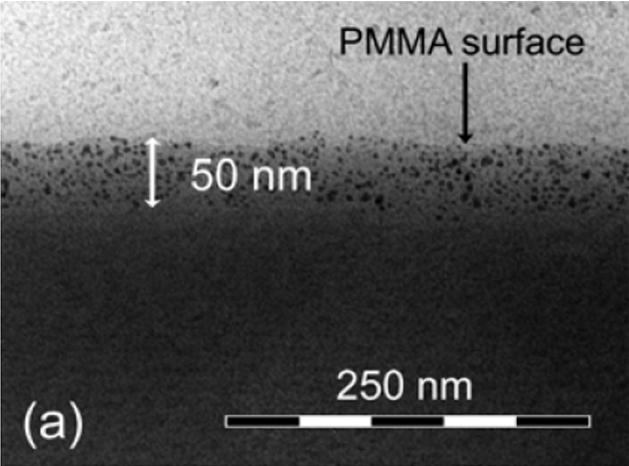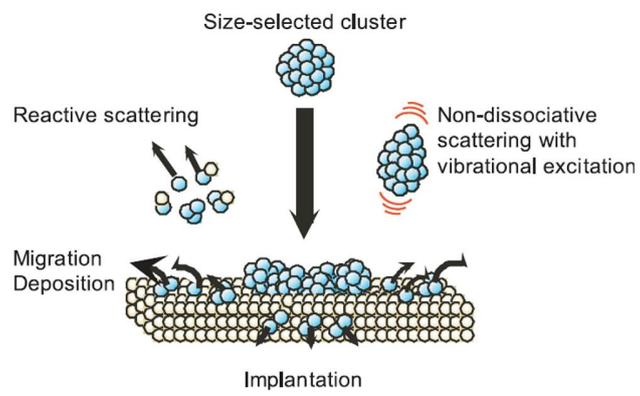
Fig. 23

Fig. 24

(a)

(b)

Fig. 25

(a)

(b)

(c)

(d)

Fig. 26

Fig. 27

Fig. 28

(a) 0.2ps   (b) 0.4ps   (c) 1.2ps

Fig. 29

Fig. 30

Fig. 31

Fig. 32

1 nm

nm
200

150

100

50

0

200

150

100

50

0

Fig. 33

Fig. 34

Fig. 35

Dislocated atoms
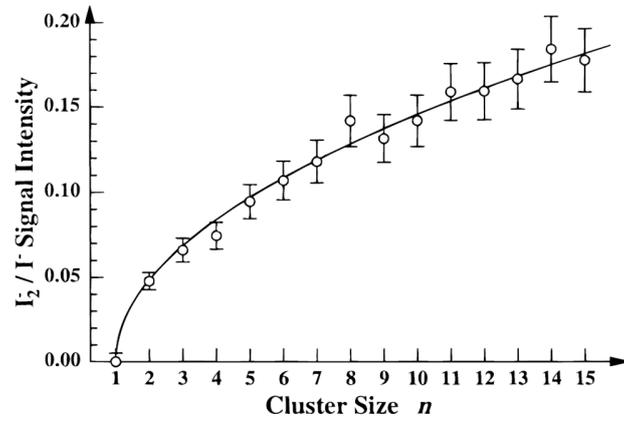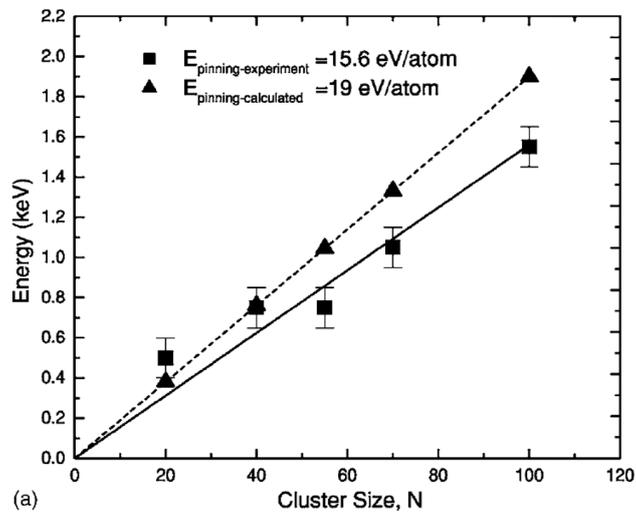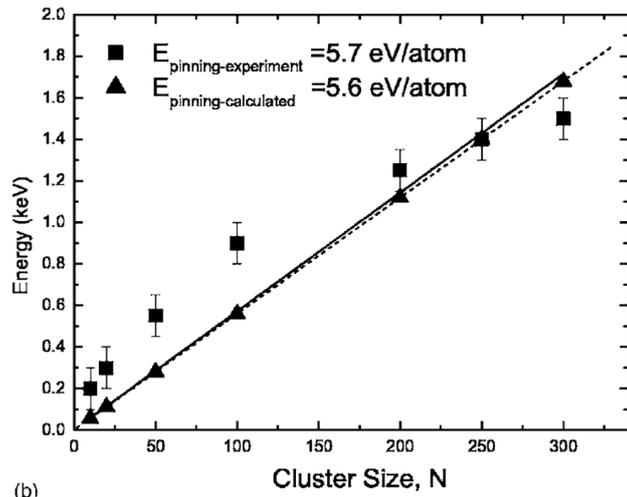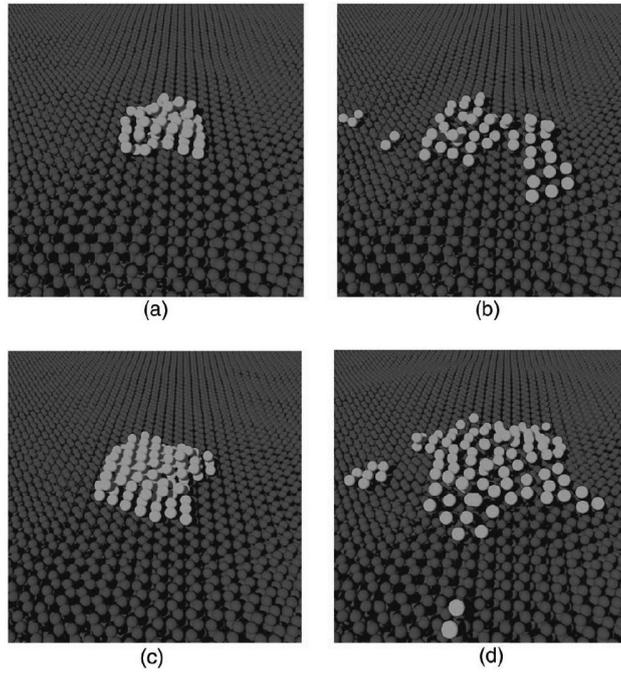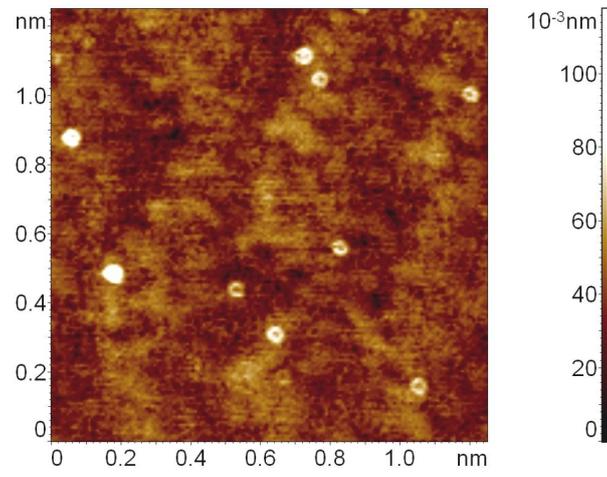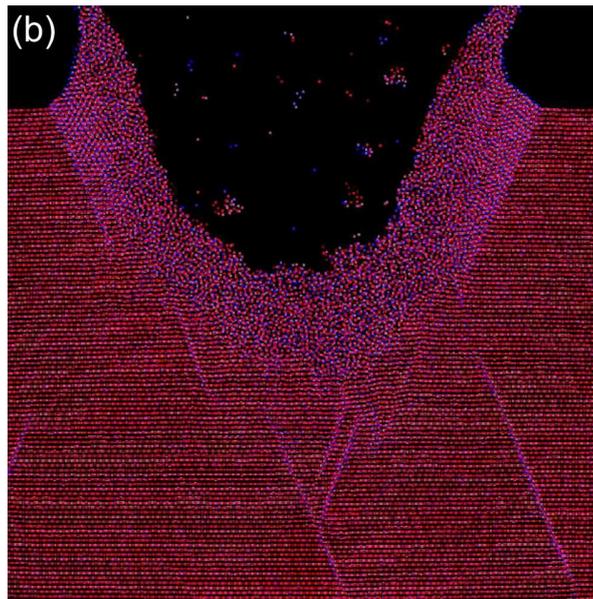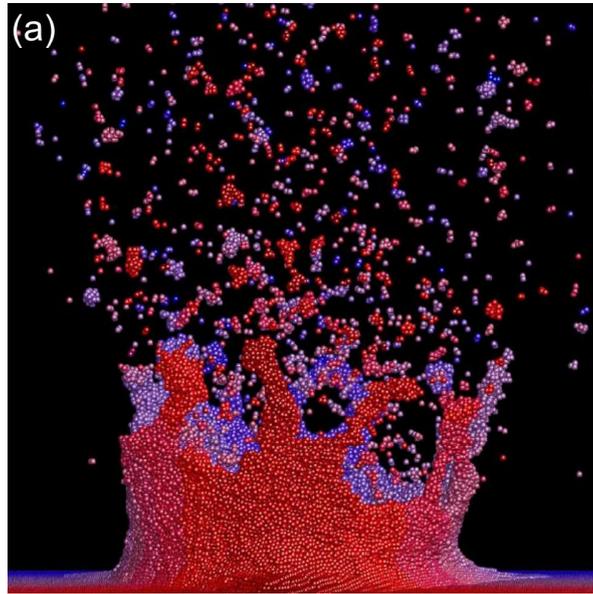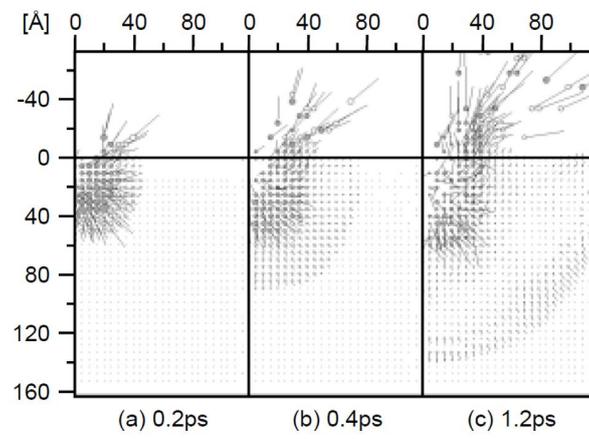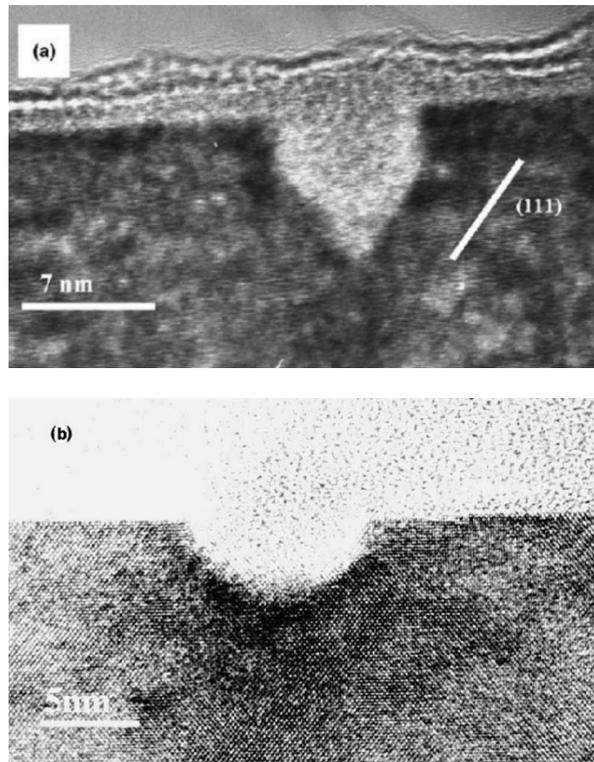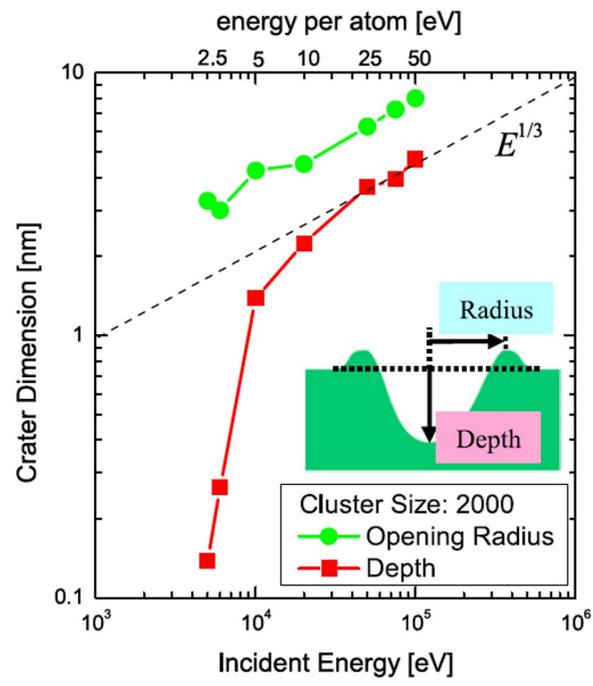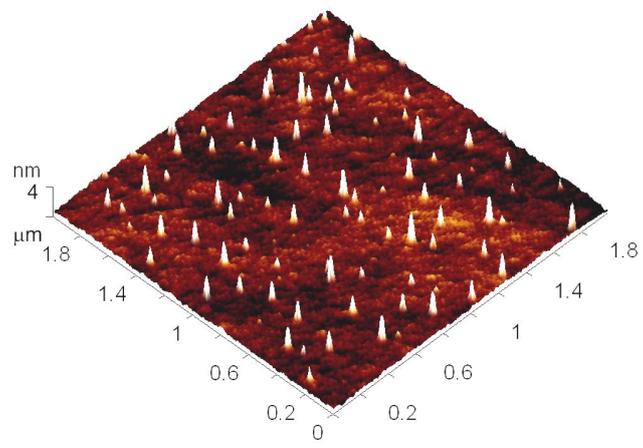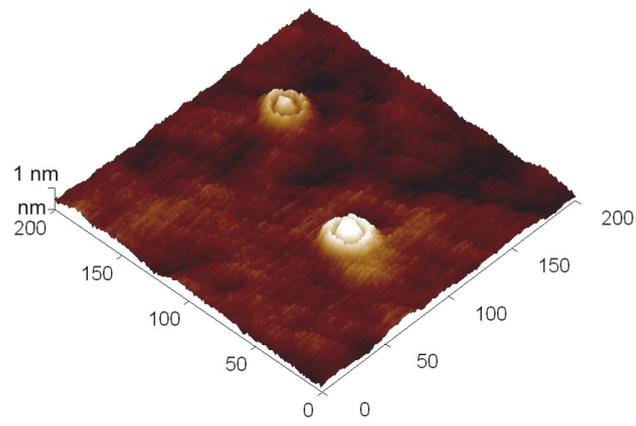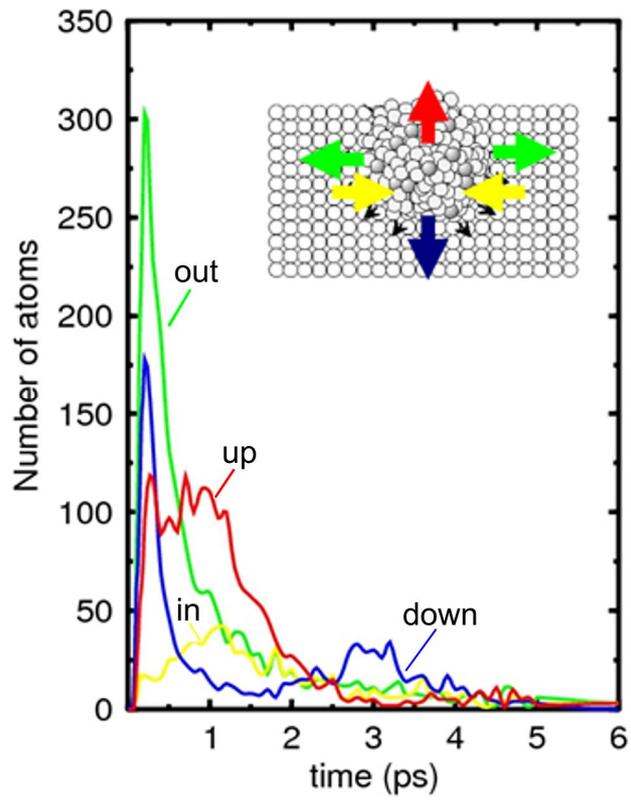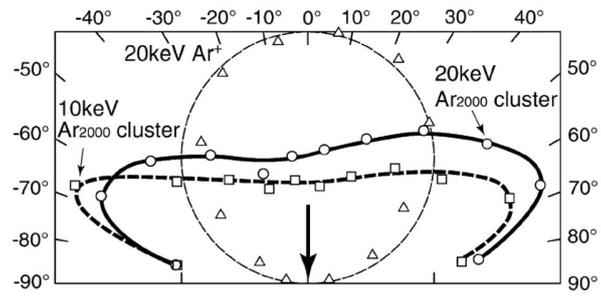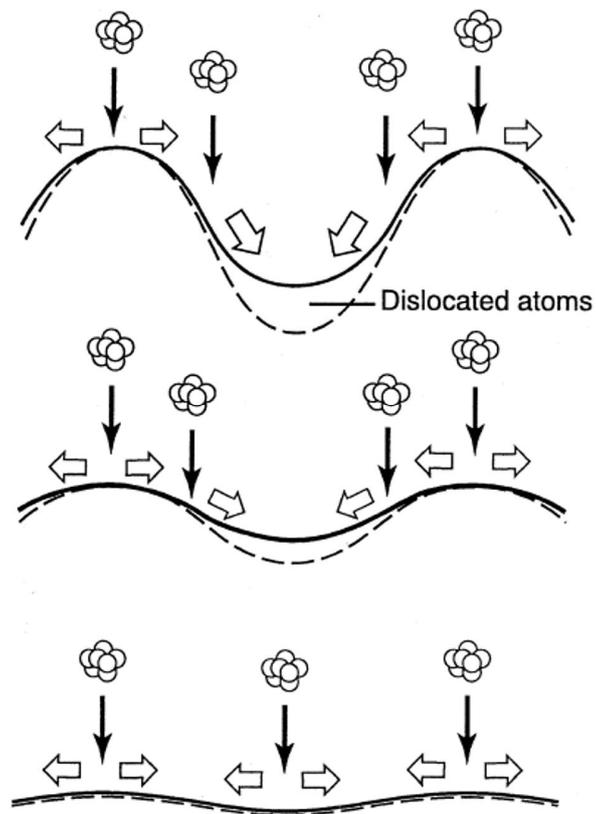
Fig. 36

Fig. 37

Fig. 38

Fig. 39

Fig. 40

Large Cluster　　　　Small Cluster

Substrate atoms
gain kinetic energy

Similar Damage
Formation Effect
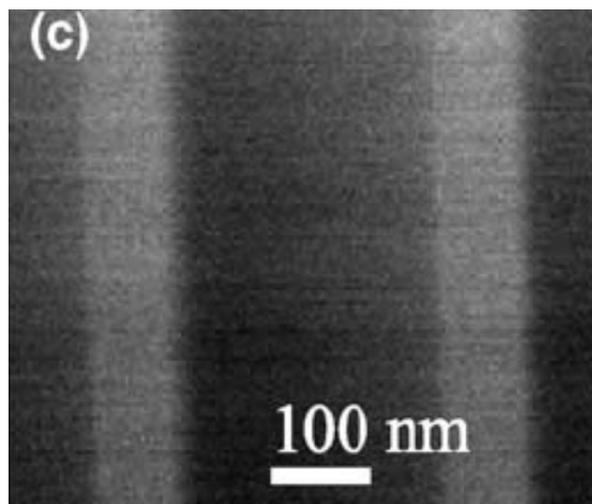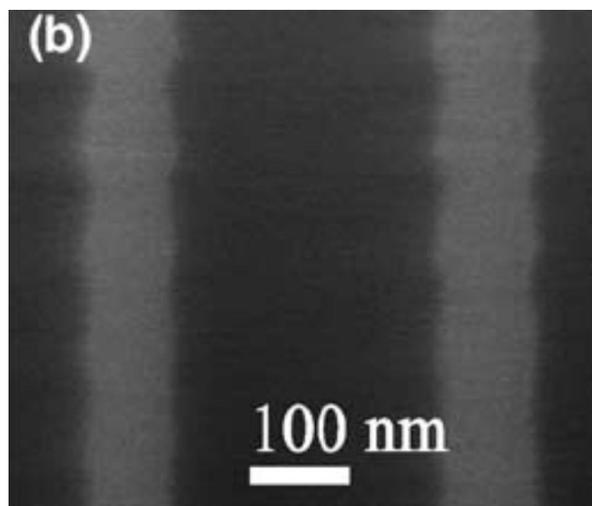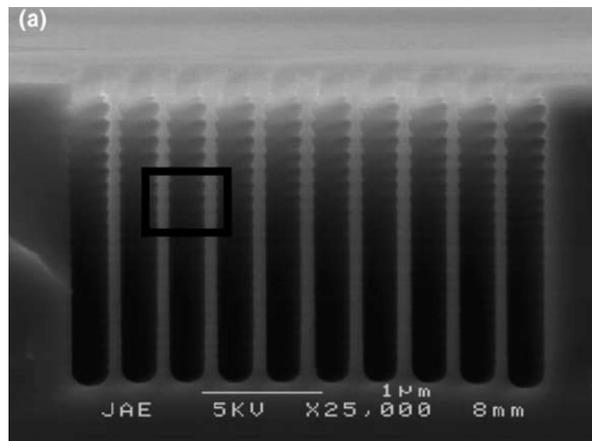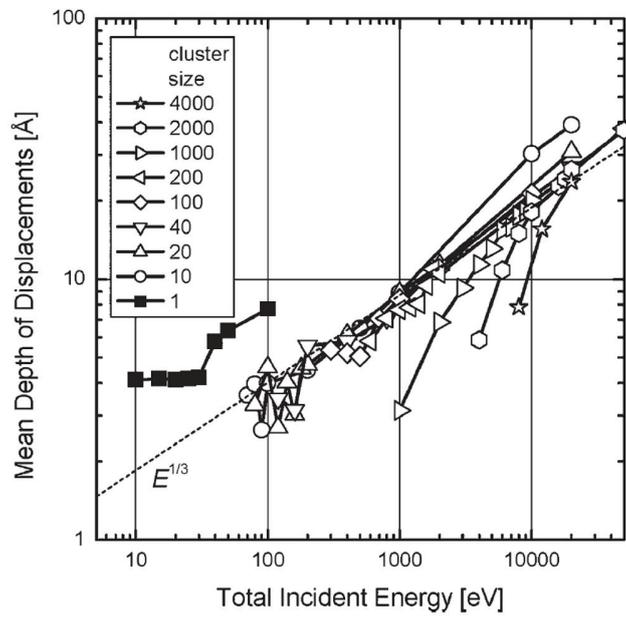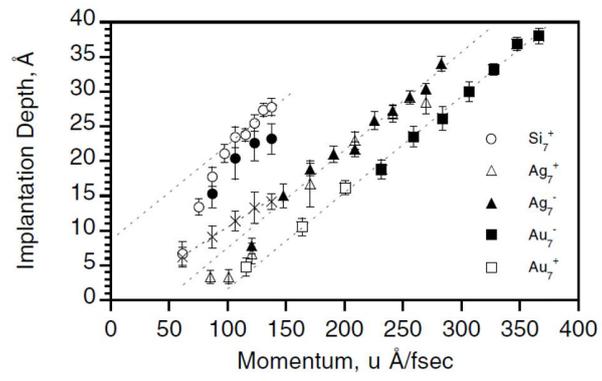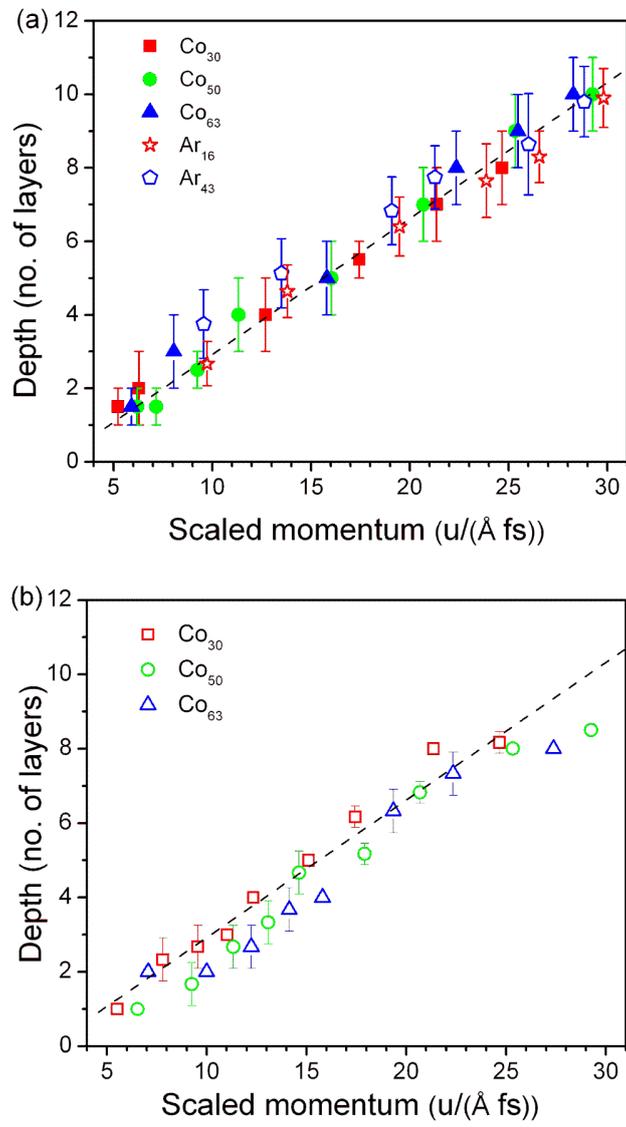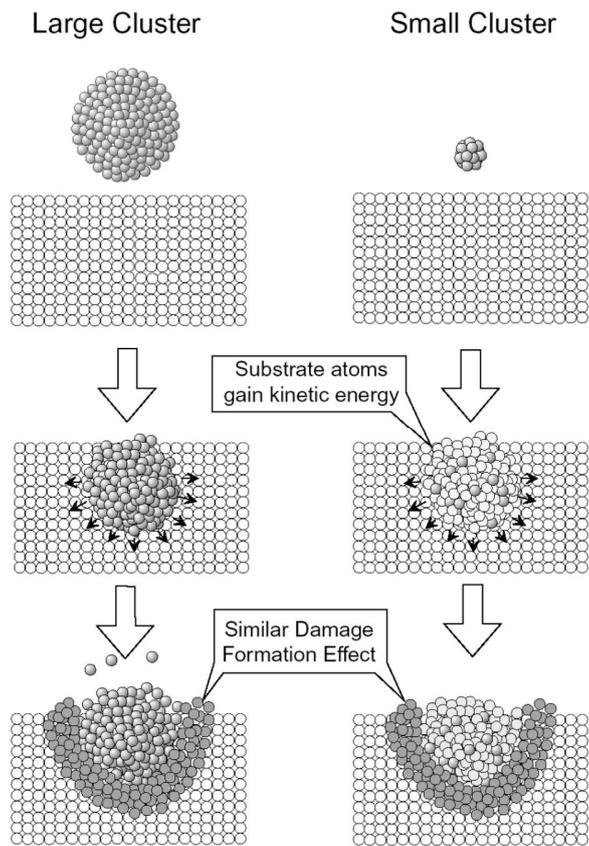
Fig. 41

Fig. 42

Fig. 43

Fig. 44

Fig. 45